Università degli Studi di Modena e Reggio Emilia

Dipartimento di Scienze Fisiche, Informatiche e Matematiche

Doctoral Course in Physics and Nanosciences

Coordinator: Prof. Marco Affronte

Scientific-Disciplinary Sector: PHYS-06/A

Cycle: XXXVII

Approaches to study how cells react to mechanical stimuli

Supervisor:

Prof. Andrea Alessandrini

Candidate:

Beatrice Bighi

Academic Year 2023/2024

Summary

Abstract (ita)

La meccanobiologia è una disciplina emergente che approfondisce le implicazioni che stimoli meccanici esercitano sulle cellule e le forze che le cellule applicano a loro volta sull'ambiente esterno. Queste non solo avvertono l'ambiente loro circostante, ma recepiscono le informazioni provenienti dall'esterno attraverso la meccanotrasduzione. In questi processi sono coinvolti alcuni attori principali quali il citoscheletro cellulare e complessi proteici ancorati alla membrana nucleare (complesso LINC) e alla membrana plasmatica (adesioni focali). In genere, la meccanobiologia studia il comportamento delle cellule in relazione a caratteristiche peculiari dell'ambiente o in risposta a specifiche perturbazioni (ad es. topologia del substrato, gradienti chimici, dimensione dei pori, strain stress, shear stress, ecc.). Questo lavoro di Tesi presenta un assortimento di cell stretchers sviluppati dal NanoBioLab per acquisire imaging time-lapse al microscopio ottico di cellule *in vitro* e approfondisce la risposta di diverse linee cellulari a stimoli meccanici specifici, in particolare:

(i) Fibroblasti cardiaci (HCF) coltivati su supporti elastomerici 2D sono stati sottoposti a stimoli di stretching periodico, diversi per forma d'onda, frequenza e direzionalità. Questi esperimenti sono stati svolti con lo scopo di gettare le basi per una maggiore comprensione degli effetti dello stretching sui fibroblasti cardiaci, dal momento che essi sono al centro di un lungo dibattito a proposito del loro ruolo nei processi di riparazione tissutale nel miocardio e di fibrosi.[1]

(ii) Cellule di glioblastoma multiforme (U87MG) coltivate su supporti μ-patternati sono state studiate per comprendere gli effetti della topologia del substrato sulla migrazione. Questo studio si collega all'interrogativo metodologico sulla trasferibilità dei risultati ottenuti da esperimenti 2D e 3D. Come approccio intermedio, supporti quasi-3D con micropillars sono stati usati per studiare la migrazione cellulare. Per validare il nostro approccio per confronto con esperimenti con cellule di glioma già pubblicati in letteratura abbiamo studiato l'effetto della blebbistatina (un inibitore dei motori di miosina) sulle cellule U87MG. Un obiettivo secondario di questa Tesi, parte di un più ampio progetto esistente, consiste nel valutare l'effetto di un potenziale nuovo farmaco per il trattamento del cancro, denominato 1*g*, nella migrazione singola e collettiva delle U87MG.[2]

(iii) Cellule di tumore del colon (HCT166) over-esprimenti le due isoforme della subunità A del fattore di trascrizione NF-Y sono state analizzate nella loro migrazione collettiva. Questo studio fa parte di un progetto più esteso indirizzato alla caratterizzazione dei diversi fenotipi

cellulari presenti nel tumore colon e nell'identificazione del loro ruolo nei processi di invasione e metastasi.[2]

[1] In collaborazione con l'Istituto INBB Biostructures and Biosystems National Institute di Bologna
[2] In collaborazione con il Dipartimento di Scienze della Vita dell'Università di Modena e Reggio Emilia

Abstract (eng)

Mechanobiology is emerging as a subject that provides useful insights into the implications of external mechanical stimuli on cells and, vice versa, of the forces applied by cells on their external environment. Cells, in fact, not only sense the external environment (mechanosensing), namely the extracellular matrix, but also translate information coming from the outside through mechanotransduction. The processes involve some major actors such as the cell cytoskeleton and protein complexes either anchored to the nuclear membrane (LINC complex) or to the plasma membrane (focal adhesion complexes). Generally, mechanobiology topics consider cell behavior in relation to peculiar characteristics of either the environment or to a specific perturbation (e.g. substrate topology, chemical gradients, pore size, strain stress, shear stress, etc.).

This Thesis both presents a collection of custom-made cell stretchers designed for time-lapse imaging by optical microscopy of *in vitro* cells and delves into the response of different cell lines to case specific, tailored mechanical cues, in particular:

(i) Human cardiac fibroblasts (HCF) cultured on 2D elastomeric substrates were subjected to different periodic stretching stimuli differing in waveform, frequency and in directionality. This line of inquiry aims at paving the way for a deeper understanding of the effects of mechanical stretch in cardiac fibroblasts as they are the center of a long-lasting biological question regarding their role in repair processes in the heart tissue and the onset of fibrosis.[1]

(ii) Glioblastoma cells (U87MG) cultured on 2D μ-patterned substrates were studied to shed light on the effects of substrate topology on cell migration and their mechanical aspects. This topic is related to a methodological question about whether 2D and 3D substrates might or might not yield the same results regarding cell behavior. As a middle ground, quasi-3D substrates with micropillars were used to investigate cell migration. To validate our model by comparison with experiments on glioma cells already present in literature, we studied the effect of blebbistatin (an inhibitor of myosin motors) on U87MG cells. A minor line of inquiry of this work, part of an already established project, was dedicated to assessing the effect of a potential novel drug for cancer treatment, 1*g*, in both single-cell and collective migration of U87MG cells.[2]

(iii) Human colon tumor cells (HCT166) overexpressing the different isoforms of the transcription factor subunit NF-YA were studied in their collective migration. This study was

carried out as part of a wider project that aimed at characterizing the different phenotypes and their role in the processes of invasion and metastasis.[2]

[1] In collaboration with the INBB Biostructures and Biosystems National Institute in Bologna
[2] In collaboration with the Department of Life Sciences of the University of Modena and Reggio Emilia

Thesis outline

The Thesis is outlined as follows:

In **Chapter 1** a general introduction to mechanobiology is presented, alongside the cytoskeleton, its main components and the elements of mechanosensing that enable mechanotransduction to send stimuli to the nucleus. In addition to that, a brief summary of the state of the art about cell stretcher devices is given and, finally, the experimental lines of inquiry studied in this Thesis are outlined.

Chapter 2 provides technical details about the adopted experimental setups, covering time-lapse imaging of in *in vitro* cell samples, the construction of cell cyclic stretchers, the fabrication of substrates for cell culturing in adhesion and information about cell lines used in this Thesis work. A brief explanation of the theory of calibration of the cell stretcher substrates is introduced, alongside its validation by Finite Element Measurement simulations. Moreover, an exhaustive explanation regarding how image analysis was performed and how the quantitative parameters adopted to study cell response were defined are given.

Chapter 3 offers a thorough characterization of the cell cyclic stretchers developed by the Nanobiolab group, including the results of their calibration and validation.

In **Chapter 4** the results of the first line of inquiry investigated in this Thesis, the application of stretching stimuli to Human Cardiac Fibroblasts, are reported. In the Chapter, results from both uniaxial and 90°-inversion (directional change of the uniaxial mechanical stimulus) experiments are presented.

Chapter 5 compiles the results of different migration studies performed with glioblastoma multiforme U87MG cells. The first Section of the Chapter examines the effects of treatment with a potential new drug for cancer treatment (defined as "1*g*"). The second Section investigates the migration of cells confined by μ-pillared substrates and explores, using blebbistatin treatment, whether these substrates could serve as an alternative to 3D substrates.

Chapter 6 gathers the results of collective migration experiments performed on Human Colon Tumor (HCT166) cells, investigating the molecular signatures of the NF-YA long and short isoforms on cell phenotype.

Chapter 7 draws the conclusions of this Thesis while in the **Appendix** the codes of a few ImageJ macros are transcribed.

Chapter 1 – Introduction

In **Section 1.1** of this Chapter, the concept of Mechanobiology is introduced to the reader, with a quick highlight of its implications in Life Sciences.

The following **Section 1.2** gathers a comprehensive overview of the cell cytoskeleton and its main components, focusing on those that are regarded as the most relevant one in mechanobiology. A series of proteins involved in cell movement, mechanosensing, mechanotransduction and in the physical connection to the nucleus is also presented.

In **Section 1.3** a quick introduction to cell stretching devices is given, together with a mention to current theories regarding cellular response to stretching stimuli.

In **Section 1.4** the biological mechanisms of cell migration are outlined, spanning through single-cell and collective migration as well as mesenchymal and amoeboid migration.

Finally, in **Section 1.5** the aims of this Thesis are presented.

1.1 Mechanobiology

In the last few decades, mechanobiology emerged as the *"missing link"* between cell biology, physics and medical engineering, accounting for all those physical aspects, factors and signals that, traditionally, were neglected in other disciplines [1]. The subject exploits multidisciplinary approaches in order to study how physical inputs are perceived and transduced by the cells, applying mathematical models [2], making use of mechanical devices (see **Section 1.3**) and different techniques.

Mechanical signals – and in general physical cues – keep raising the interest of a wide research community, so that the 2021 Nobel Prize for Physiology or Medicine has been awarded to Dr. David Julius and Dr. Arden Patapoutian, whose work focused on the mechanosensitive ion channels Piezo1 and Piezo2 [3] and on the heat-activated ion channel TRPV1 [4]. Mechanical forces – either internal or external – interplay with biochemical signaling exerting a regulatory effect in different biological activities such as morphogenesis, migration, differentiation, proliferation and polarization [5].

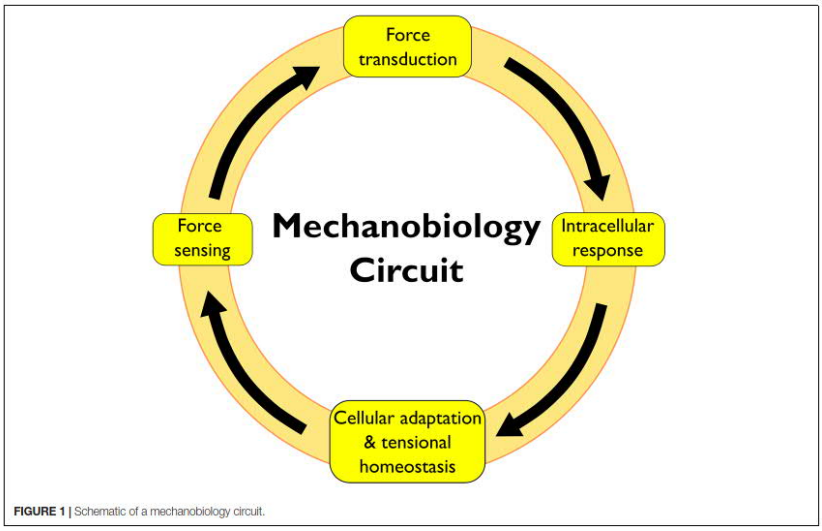

Fig. 1 The mechanobiology circuit in brief, from [5].

This interplay becomes evident especially in the physio-pathological context, where the alteration of mechanical properties of either single cells, aggregates of cells or even entire tissues can result in the onset of diseases and discomforts. Some relevant examples to this account are cardiac fibrosis, a stiffening of the heart muscle due to the dysregulation of the process of tissue repair by cardiac fibroblasts; and the process of metastasis in cancers, which relies on the ability of malignant cells to travel quickly from their primary site to other organs [6]. Another strong point validating the mission of mechanobiology is the need to study systems that are physiologically undergoing periodic mechanical stimulations, e.g. cells in the blood vessels subjected to blood flow/pressure pulsations, cells in the cardiac muscle experiencing the heartbeat, lung cells during breathing, cells of the gut during peristalsis, etc.

1.2 Cell cytoskeleton

The cytoskeleton is one of the most studied cell structures in mechanobiology since it plays a central role in determining the shape and the mechanical properties of the cells, it is involved cells movement, and it is regarded as the primary actor involved in the sensing and transduction of external physical stimuli. The cytoskeleton is an extensively organized and dynamic structure which can be described, from a biochemical point of view, as a tridimensional network of different proteins. It provides support for the cell body and organelles, directs the transport of substances, anchors cells to the substrate, etc. Some of these proteins are present as homo-

/hetero-polymers with *microtubules, actin fibers* and *intermediate filaments* being the most important ones.

1.2.1 Microtubules

Microtubules are polymers of the protein *tubulin*, a heterodimer composed by the globular proteins *α-tubulin* and *β-tubulin*, tightly non-covalently bound together. Both monomers exhibit a GTP-binding domain, with different accessibility to the solvent. Tubulin heterodimers associate head-to-tail in large linear structures called protofilaments whose endings are defined as the plus end (the β-tubulin ending extremity) and the minus end (exposing α-tubulin). The microtubule is a hollow cylindrical structure given by the lateral association of 13 parallel and slightly staggered protofilaments. The microtubule lattice preserves the polarity of its protofilaments with its plus end being more subjected to growth and shrinkage. These two processes cyclically alternate as a consequence of the periodical hydrolysis/phosphorylation of the exchangeable fraction of GTP-binding domains at the tip of the protofilaments. This phenomenon of growth and shrinkage is known as *dynamic instability* and relies on the rate of heterodimers addition, the rate of GTP hydrolysis and the concentration of free GTP-tubulin heterodimers in solution. The dynamics of microtubules assembly/disassembly is central in many processes, and it is usually the target of pharmacological treatments that aim at microtubules.

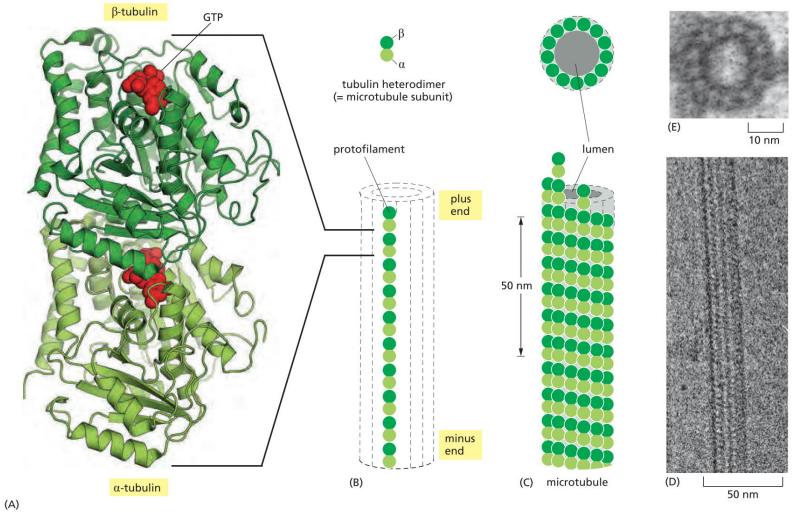

Fig. 2 Schematic representation of the αβ-tubulin heterodimer (a), protofilaments (b) and microtubules (c). Electron micrograph of a short section of a microtubule seen from the side (d) and from the cross section (e) (from [7]).

The microtubule cytoskeleton acts as a railway to transport cargo, in particular thanks to the action of two molecular motors families known as *kinesis* and *dyneins*.

Even though microtubules can nucleate in any part of the cell, many of them originate from the microtubule-organizing center (MTOC), a specific intracellular site rich with γ-tubulin ring complexes (γ-TuRC) that arrange γ-tubulins in a spiral template that eases the assembly of 13 protofilaments into a microtubule. In animal cells, the MTOC is represented by the *centrosome*, a spherical organelle close to the nucleus where the minus ends of microtubules are located while their plus ends grow outwards. This localization of the centrosome close to the nucleus is thought to establish an inner reference system for the cell, with microtubules "probing" the cell volume and organizing in space the various organelles. Its central location is also advantageous if we take into consideration the presence of *centrioles*, a set of two cylindrical and perpendicular modified microtubules, contained into the centrosome, whose activity is strongly related to cell mitosis. During mitosis centrosomes duplicate and migrate, with their couple of centrioles, to opposite sides of the nucleus, forming the *mitotic spindle*, a complex architecture that pilots the partitioning of the genetic material between daughter cells terminated by *cytokinesis*.

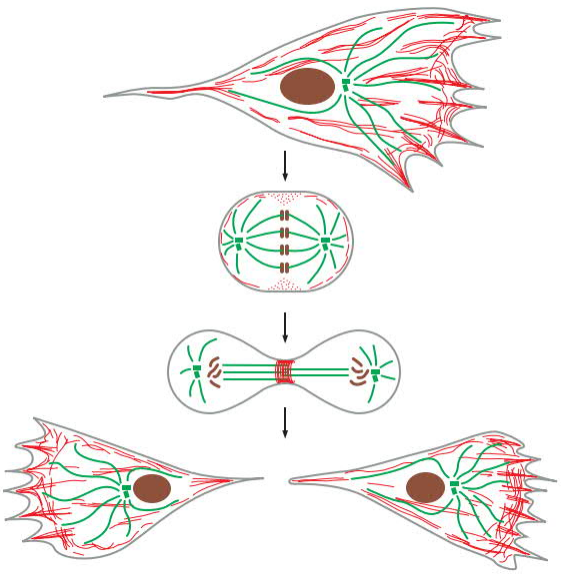

Fig. 3 Schematic representation of microtubules (in green) and actin filaments (in red) in a cell undergoing duplication (from [7]).

Many pharmacological treatments for cancer therapy aim at blocking cell duplication by directly interacting with microtubules. Among these, some drugs impair microtubule polymerization (such as *colchicine* and *nocodazole*) while others stabilize microtubules enhancing their formation (*Taxol*). In both cases, the interaction with the microtubules – either scarcely formed or stabilized to the extent that cell division is prevented – results in failure in cell duplication.

Specifically related to the work of this Thesis, recent studies have been scouting the effects of a novel 2,3-benzodiazepin-4-one derivative drug, defined as 1*g*, with particular focus to its potential applications in cancer treatment [8], [9], [10]. 1*g* was proven to be effective at blocking mitosis in different cell lines such as Jurkat cells [8], HeLa [9] and, recently, U87MG [10], [In preparation]. The compound acts primarily as a cytostatic agent that accumulates cells in the G_2/M and, at long exposure times, it also shows sign of cytotoxicity. The mechanism of action of 1*g* affects the dynamics of microtubules formation, decreasing the growth rate. It also affects centrosomes separation and loosens the organization of the mitotic spindle. Even though 1*g* does not stabilize microtubules, as Taxol does, 1*g*-treated cells do not bring mitosis to completion. Treated cells appear circular-shaped, with double the amount of DNA content, but unable to progress into cytokinesis. After some time, cytotoxic effects kick in and cause apoptosis to occur.

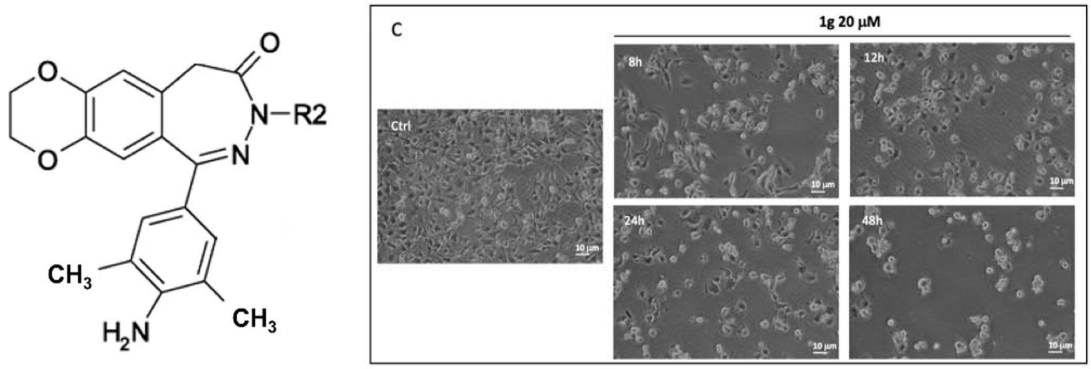

Fig. 4 On the left, molecular structure of 1*g* (adapted from [8]); on the right, U87MG morphology upon 20 µM 1*g* treatment (from [10]).

In this Thesis the effects of 1*g* on both single-cell and collective migration are presented in **Chapter 5**. These findings are but a small portion of a wider investigation directed to study of the effects of the drug on U87MG cells both in 2D and 3D experiments [In preparation].

1.2.2 Actin filaments

Actin filaments are rod-like homopolymers obtained by the coiling of two strands of filamentous actin (*F-actin*), which is the linear polymer resulting from the polymerization of the free actin monomer, *G-actin* (globular actin) (**Fig. 5a, b, c**). Since G-actin is a polar molecule, F-actin inherits such polarity that brings the distinction between the *pointed end* (the minus end) and the *barbed end* (the plus end) of the strands. The two sites are characterized by different reactivity: while at the barbed end polymerization occurs quickly, at the pointed end depolymerization is favored. This difference in polymerization/depolymerization rates results in the phenomenon of *treadmilling*, where the fiber is continuously being renewed by the simultaneous addition of monomers at one end and the loss of monomers at the other. Actin filaments are known to assemble in complex textures with different geometries (see **Fig. 5d**) responding to different biological tasks: contractile actin filaments known as *stress fibers* are spread in the bulk region of the cell body and are involved in cell locomotion; branched networks of actin filaments provide support in the cell cortex and in lamellipodia, while parallel bundles in filopodia help cells to explore the surroundings.

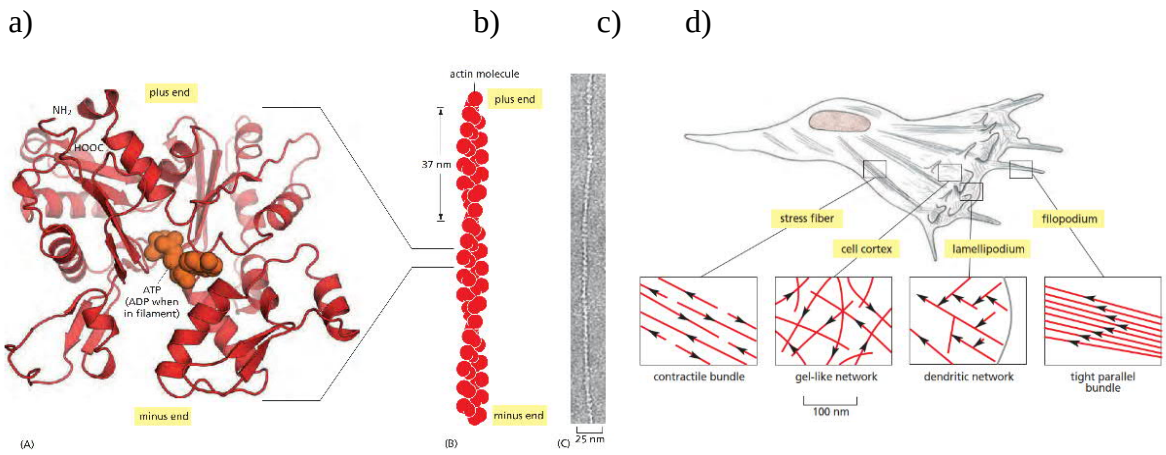

Fig. 5 Protein structure of G-actin (a), schematic representation of F-actin (b), SEM micrograph of an actin filament (c) and schematic representation of different F-actin assemblies (from [7]).

Stress fibers are regarded with deep interest in mechanobiology, as they are a physical link that mechanically connects the nuclear envelope to the external anchorage points, which are known as *focal adhesions* (see **Fig. 6** and **Section 1.2.4**) [11].

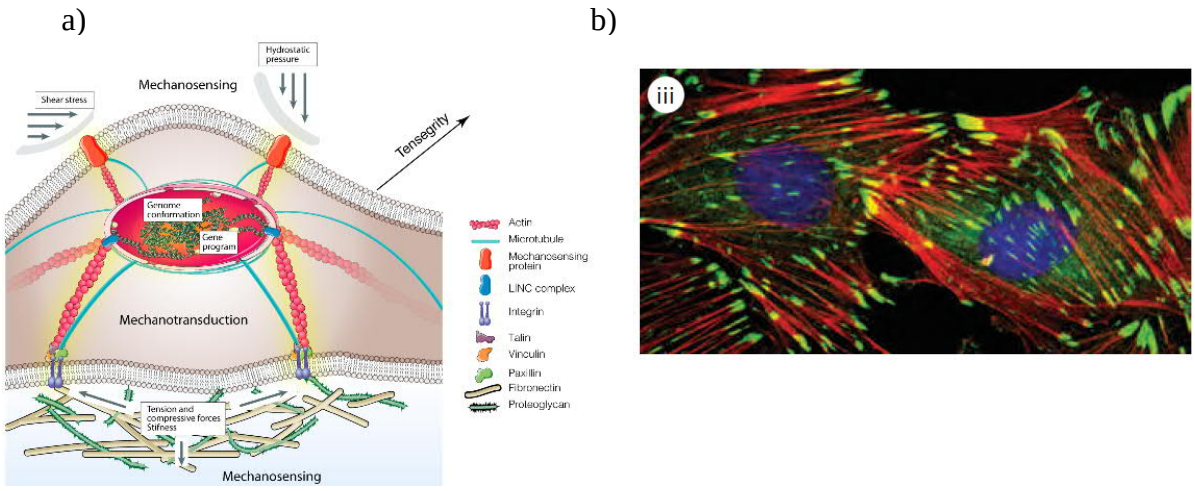

Fig. 6 Schematic representation of the connection stress fiber-focal adhesion-ECM (a), adapted from [11]. Micrograph of cells, with nuclei stained in blue, stress fibers in red and focal adhesions in green (b) (from [7]).

1.2.3 Intermediate Filaments

Intermediate filaments are large protein assemblies with a rod-like appearance and a 10-nm diameter. These supramolecular structures are the result of a complex association of different proteins, which share a large central α-helical domain that features about 40 heptad repeat motifs, enhancing the achievement of the structure of coiled-coils oligomers [7]. Coiled-coil dimers form tetramers by lateral interaction with other dimers, in a staggered configuration; tetramers then associate in groups of eight creating rope-like structures (**Fig. 7**). Intermediate filaments do not feature nucleotide-binding sites and are, generally, highly deformable polymers that can be stretched several times their initial length and bent to a great extent without rupturing.

The mechanism of assembly/disassembly of intermediate filaments is still unclear.

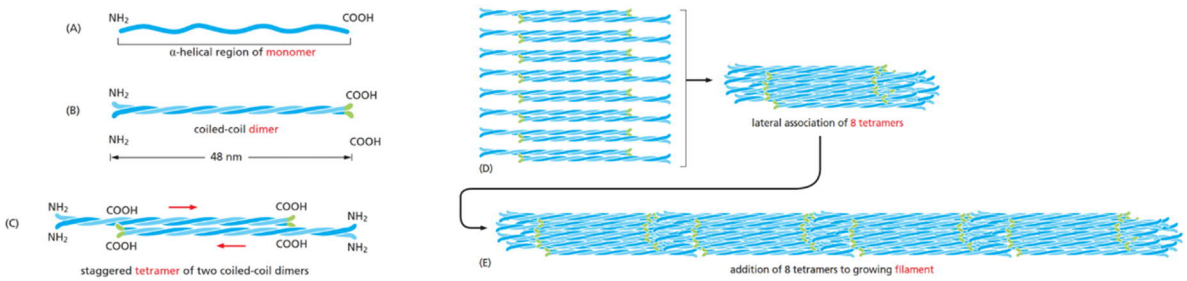

Fig. 7 Schematic representation of the structure of intermediate filaments (from [7]).

About 70 different genes in the human genome code for intermediate filament proteins; a classification based on similarities in protein structure and peptide sequence divides these proteins into types I and II (acidic and neutral/basic *keratins*), type III (includes *vimentin* and *desmin*), IV (includes *internexins*), V (nuclear *lamins*) and VI (includes *nestin*). T role of intermediate filaments is various and dependent on their type, generally, they confer mechanical stability to the cytoskeleton and the nucleus, and they are known to interact with *desmosomes* (cell-cell adhesion) and *hemidesmosomes* (cell-ECM adhesion) via adaptor proteins.

1.2.4 Focal adhesion complexes and other proteins involved in cell adhesion

Focal adhesions are macromolecular complexes resulting from the association of an ensemble of proteins that secure the extremity of a cytoskeletal stress fiber to the cell plasma membrane, eventually providing anchorage for the cell to the external environment (i.e. the Extra Cellular Matrix, ECM in short). The most important protein is integrin, a heterodimeric cell surface receptor that spans across the plasma membrane and acts as a mechanosensor. The extracellular domain of integrin binds with ECM proteins – e.g. fibronectin and collagen, through their Arg-Gly-Asp (RGD) peptide sequence – while its intracellular domain anchors to a multitude of other smaller proteins (adaptors) bound to the stress fibers of the cytoskeleton. Into the umbrella term focal adhesion other interesting proteins such as *talin*, *paxillin* and *focal adhesion kinases* (FAK) are included.

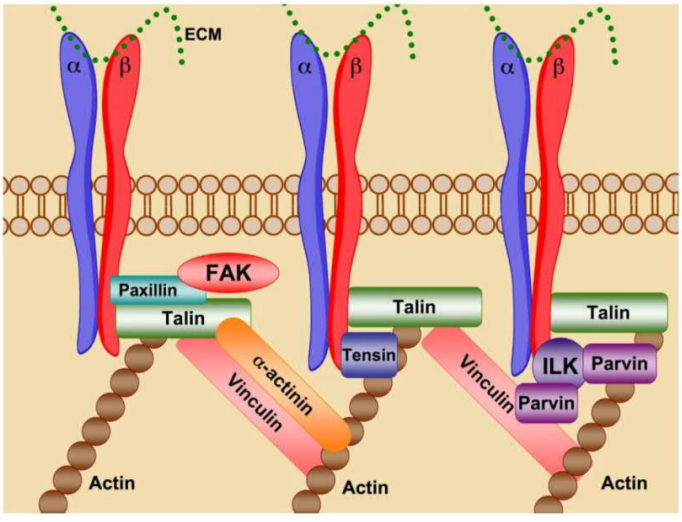

Fig. 8 Schematic representation of the main proteins in focal adhesions. The α and β subunits depict integrins (from [12]).

Different proteins are capable of binding to actin [7]: among these, non-muscle myosin II has a particular importance in mechanobiology since its interaction is at the basis of the exertion of contractile traction forces by cells. The role of myosin-II will be described in more detail in **Section 1.2.5**. In addition to myosin, also *α-actinin* and *vinculin* are worth mentioning, as they "sew" together parallel stress fibers into a more complex network.

1.2.5 Non-muscle myosin II and the swinging cross-bridge model

Myosin II molecules are known – together with actin – as the main contractile proteins in skeletal, smooth and cardiac muscles. An analogous counterpart with a similar function, defined as non-muscle myosin II (NMII), was found in all non-muscle eukaryotic cells [13]. NMII molecules appear as coiled-coil dimers with a rod-like domain and two actin-binding globular heads. Upon phosphorylation, the NMII align to actin filaments in the cytoskeleton so that the catalytic sites with ATPase activity, contained in the globular heads, can bind to actin [14].

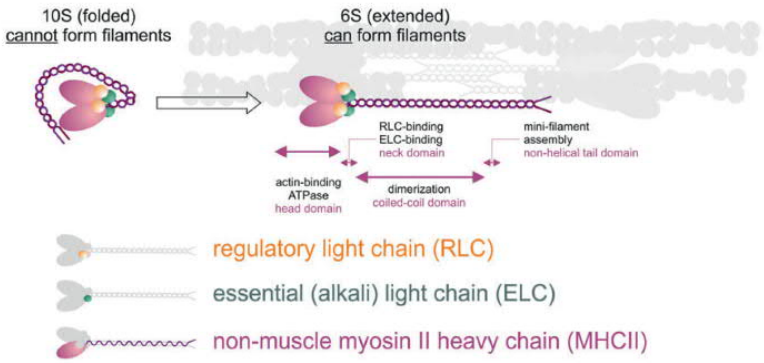

Fig. 9 NMII conformations: on the left, the folded assembly-incompetent dimer; on the right, the assembly-competent conformation involved in actin-binding activity (from [14]).

The mechanism of interaction between NMII and actin filaments is described by the swinging cross-bridge model [15] and depicted in **Fig. 10a**. It involves the Ca^{2+}/Mg^{2+}-actin-dependent ATPase catalytic site of NMII to hydrolyze an ATP molecule upon actin binding. Once the assembly – called *actomyosin* – releases the phosphate group, it undergoes a conformational change in the NMII structure that results in a "power stroke", a sliding of the filament of ~ 10 nm (**Fig. 10b**).

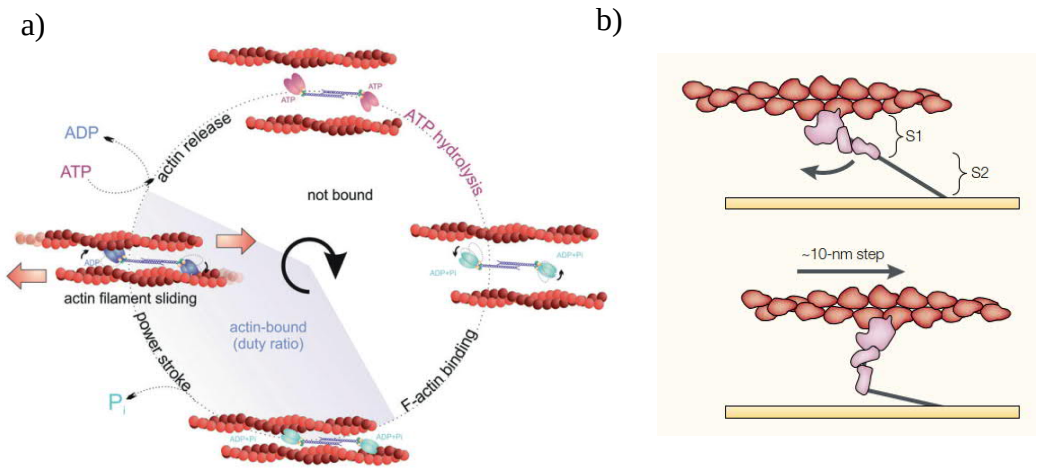

Fig. 10 (a) Diagram of the mechanism of formation of the actomyosin complex and its sliding movement (from [14]). (b) Schematic representation of the "power stroke" from [15].

Blebbistatin is an allosteric inhibitor of myosin II [16] that interferes with the release of the phosphate group after ATP hydrolysis, causing myosin heads to remain weakly bound or unattached to actin fibers, preventing the formation of the actomyosin complex [17]. This results in the impossibility for cells to exert contractile forces, an effect that has been widely exploited in mechanobiology experiments investigating the role of stress fibers in cell migration.

1.2.6 Transducing mechanical stimuli to the nucleus: the LINC complex and localization of the YAP protein

In the previous Sections we explored cell architecture with an outward point of view, focusing on the protein assemblies necessary for anchoring to the external environment. In this Section, the opposite end of the physical link, the "*Linker of Nucleoskeleton and Cytoskeleton*" (LINC) complex, is briefly described. The LINC complex includes two different protein aggregates containing the KASH and SUN domains, whose association spans through the perinuclear space between the Inner and Outer Nuclear Membranes (INM and ONM, as depicted in **Fig. 11a**). Common KASH-domain proteins are called *nesprins* and are able to bind to microtubules or to stress fibers. SUN nucleoplasmic domains are associated with the nuclear lamina (*lamin A/C*) and, eventually, to nuclear chromatin [18]. This last connection at the nuclear level enables the propagation of mechanical stimuli along the cytoskeleton and from the external environment to the nuclear environment [19], where gene regulation is possibly affected [20]. In a recent review by De Freitas et al. [21] a plethora of nuclear deformation-triggered effects is briefly

summarized, pointing out that different mechanosensitive pathways are present and can cause the onset of chromatin rearrangement (via the LINC complex) or inflammatory responses instigated by nuclear envelope (NE) rupture and consequent DNA damage (**Fig. 11b**).

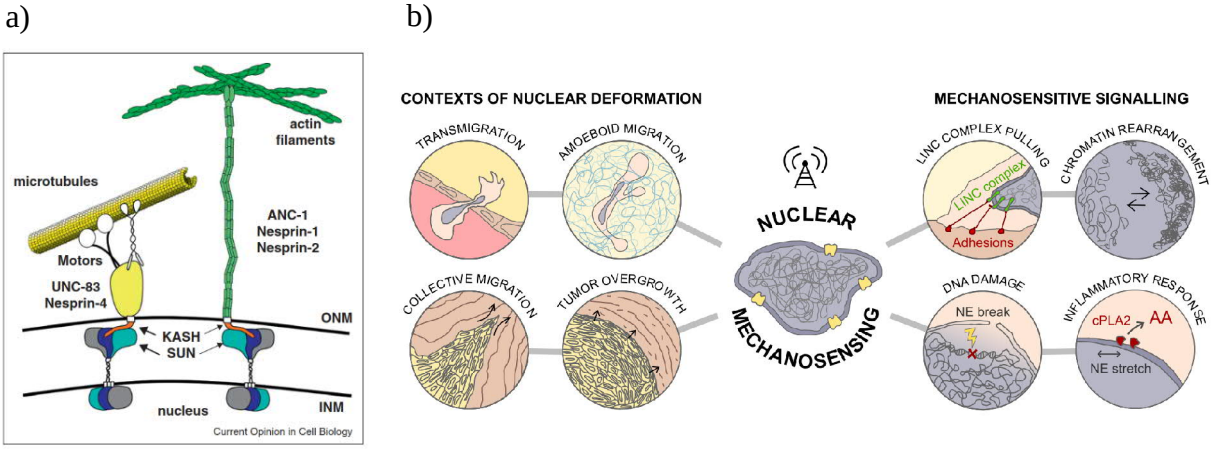

Fig. 11 (a) Scheme of the LINC complex (from [22]). (b) Schematic representation of different situations that can induce nuclear deformation and trigger mechanosensitive pathways (from [21]).

Another pathway for transducing mechanical cues to the nuclear content and affect gene expression is the translocation of transcription factors from the cytoplasm to the nucleus, such as the case of the Yes-associated protein (YAP), a transcriptional co-factor that participates in the Hippo signaling pathway.

Upon binding to transcription factors, YAP activates the transcription of target genes [23], involved with cell adhesion [24], cell proliferation [25], fibrosis [26] and the polymerization of actin [27]. The location of YAP in the cell body is often investigated: its translocation from the cytoplasmic to the nuclear compartment is, in fact, used as an index for YAP recruitment to the nucleus, a preamble to its role in gene expression. Mechanical cues such as cell density, substrate stiffness and stretching were recently identified as regulators of YAP translocation and as an evidence of the mechanotransduction event (**Fig. 12**) [28], [29], [30], [31].

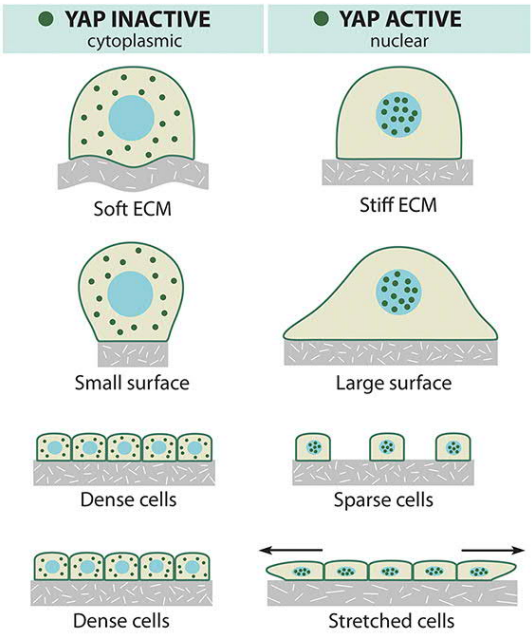

Fig. 12 Schematic representation of YAP localization upon different mechanical stimuli (www.mbi.nus.edu.sg).

1.3 Cell stretching devices and cell response to mechanical stimuli

In the past fifty years, cell stretchers probably became the most appreciated technological devices in mechanobiology, as they represent the simplest means to apply external mechanical stimuli to *in vitro* cells cultured on elastomeric substrates. From the ’70s [32], an assortment of different versions of cell stretchers spawned, either commercially available (Flexcell, Strexcell) or custom-made. The devices can differ for a multitude of case-specific features but, generally, they can be classified according to three features:

(i) the principle of actuation: most stretchers either are based on a pneumatic inflation/deflation of the culture chamber or on a stepper motor which applies a controlled deformation to the culture substrate (**Fig. 13**);

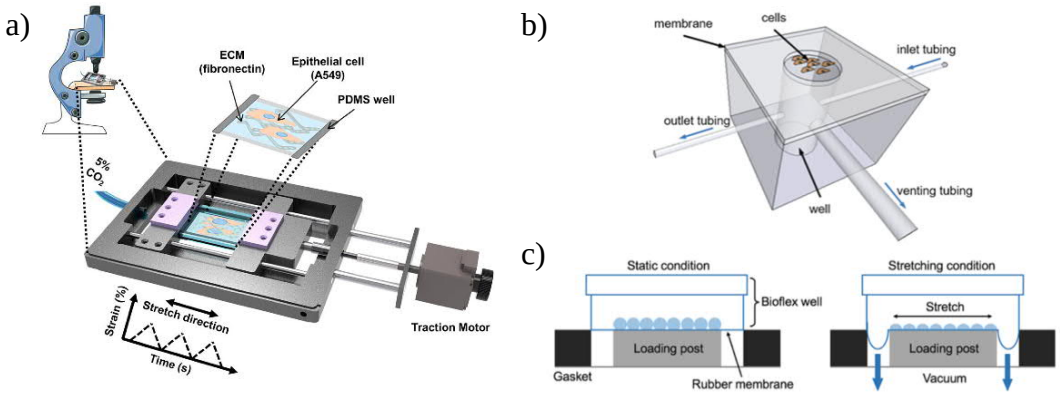

Fig. 13 (a) Examples of cell stretcher devices exploiting a motor actuation (from [33]) and (b, c) a pneumatic actuation (from [34], [35]).

(ii) the geometry of application of the stretching stimulus (uniaxial, biaxial, isotropic, etc.);

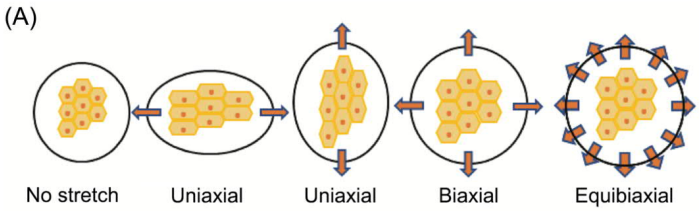

Fig. 14 Classification of the applied stretching stimulus (adapted from [36]).

(iii) type of applied stretching: *static* versus *cyclic*;

(iv) other features such as: compatibility with optical microscopy for time-lapse studies, user-friendly interfaces, customizable waveforms, accessibility to inject *in situ* drugs/reactants, application of microfluidics flows, etc.

1.3.1 Theories about cells orientation in response to stretching stimuli

One of the main effects of not-isotropic cell-cyclic stretching is cell reorientation. Currently, in mechanobiology many are striving to identify whether stretched cells choose to align according to specific directions which might be influenced by different factors such as the substrate geometry, the material elastic modulus and the features of the mechanical stimulus applied to the cells. One of the first theories regarding cell orientation was formulated by Terracio et al. [37], who observed cardiac cells orienting and elongating in a perpendicular direction with respect to the stretching direction. After that, Wang et al. [38] proposed a model which relates stress fibers orientation of endothelial cells mechanically perturbated by a cyclic stretching cue to the minimum strain direction. This interpretation has been reprised in following works, both when dealing with fibroblasts [39] and endothelial cells [40], [41], [42]. Further approaches were published by Livne et al. [43], who proposed a model where stress fibers orient along the direction of minimum energy, and by Pelling et al. [44], who reported that orientation may be guided by strain gradients. Nonetheless, in this Thesis, the zero-strain direction will be considered as the benchmark to assess cell alignment, since data were in good agreement with this theory.

1.4 Cell migration

1.4.1 Cell migration from a biological point of view

Migration, either of individual cells or cells in tissue monolayer, over a bidimensional surface is one of the most studied cellular activities to date, often with the aid of time-lapse optical microscopy. The former is usually studied in cell experiments where cells seeded at low density, hence not directly interacting, are observed during their movement, which is often described by different quantitative parameters such as cell mean speed, directionality, persistence, etc. The latter case, collective migration, is commonly studied in wound healing assays and usually they require cells to be at confluency, in monolayers in which a separation between cell fronts is created, either scratched with a pipette tip or with the aid of removable plastic strips. From a biological perspective, migration is the result of a series of biochemical events that involve

different proteins and may also include interaction with the ECM. Two distinct migration modes were characterized from a biological point of view: the *mesenchymal* mode and the *amoeboid* mode [45]. Mesenchymal migration involves distinct events in the cytoskeleton: the cell body becomes polarized, with a *leading edge* and a *trailing rear*, lamellipodia form at the front, supported by new focal adhesions and, at last, a contraction of the stress fibers drags the rear of the cell body towards the front (**Fig. 15**). Fibroblasts, endothelial cells, keratinocytes and some tumor cells are described to migrate in this mode [46]. The formation of FAs and actin polymerization are considered the speed-limiting factors that characterize the slow cell speed which is ~ 1 μm/min and local degradation of the ECM is another peculiar aspect [47].

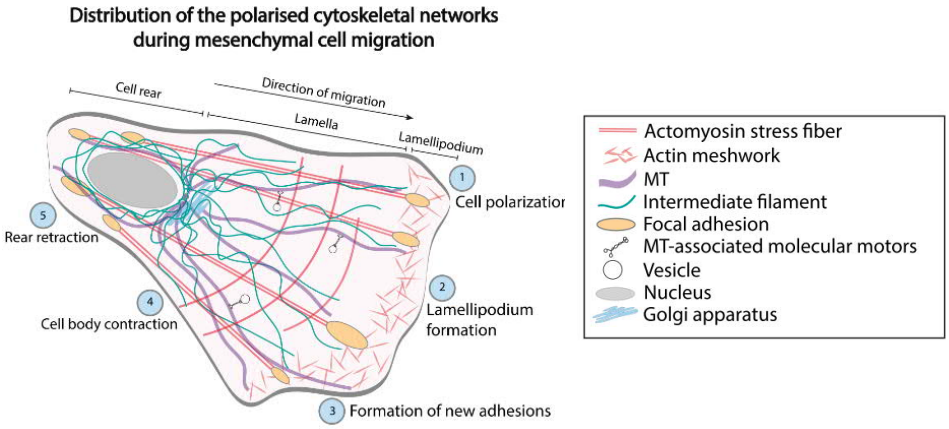

Fig. 15 Diagram of the steps of cytoskeletal rearrangement adopted during mesenchymal migration (adapted from [45]).

Amoeboid migration is somehow slightly more difficult to grasp: the motion looks “smoother” as if cells were sliding across the substrate surface, without anchoring to it. Focal adhesions are in fact not required during this migration mode, neither are stress fibers, and cell shape is rather globular (not polarized) with different types of protrusions quickly produced. A particular protrusion type is referred to as *blebs*, bulges that form in between the plasma membrane and the cortex, either because of membrane detachment or cortex rupture (**Fig. 16**), filled with cytosol liquid. Blebs form very rapidly and, after an expansion due to hydrostatic pressure in the cell body, contraction occurs in response to the polymerization and contraction of dendritic actomyosin complexes at the periphery of the plasma membrane [48].

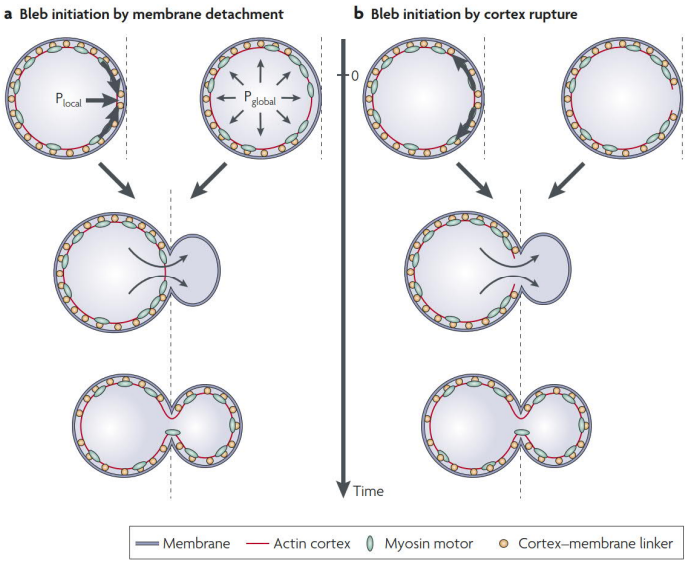

Fig. 16 Schematic representation of bleb formation (from [49]).

1.4.2 A mechanical analytical model for the traction forces at the cell-substrate interface: the molecular motor-clutch model

At the heart of the mechanosensing and mechanotransduction processes is the interaction between cells and the external substrate. In 2008 Chan and Odde, reprising a hypothesis stated by Mitchison and Kirschner in 1988 [50], proposed the motor-clutch model, with the purpose of describing the dynamics of traction forces exerted by cells as a function of the ECM stiffness [51].

In its first and simplest formulation, the one-dimensional motor-clutch model combines various components, such as myosin motor proteins, actin filaments, elastic substrates (with their elastic constant k_{sub}) and approximates the ECM-integrin-adaptor proteins-actin filament chain to a dynamic assembly, with its kinetics governed by k_{on} and k_{off} constants that describe the physical bonds of ECM, integrins and actin fibers (**Fig. 17**).

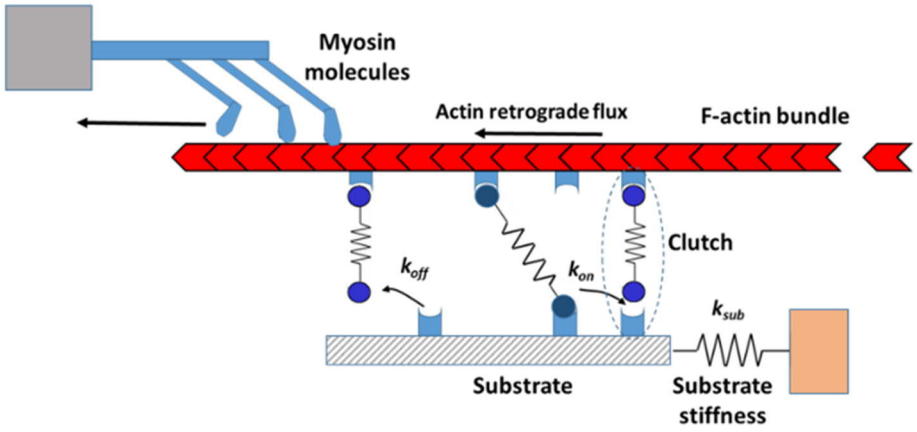

Fig. 17 Schematic representation of one-dimensional motor-clutch model (from Bighi et al., submitted).

Three mechanical equations describe the system as its main events occur:

(1) A linear force-velocity relation describes how the traction force due to the activity of myosin motors pulls back actin filaments, causing the *actin retrograde flow*. In the absence of external forces – i.e. when clutches are disengaged from the substrate – the retrograde flow moves at the speed υ_0. When clutches are engaged, the flow is linearly reduced to υ as follows:

$$v = v_0 \cdot \left(1 - \frac{F}{F_{stall}}\right)$$

where F_{stall} is the product of the maximum force generated by each single myosin motor (F_{max}) and the number of myosin motors considered (n_{motors}):

$$F_{stall} = n_{motors} \cdot F_{max}$$

(2) When clutches are engaged, the traction force that is transmitted along actin fibers, F, is distributed over the n_b (bound clutches) at work at the cell-substrate interface (Hooke's law):

$$F = \sum_{i=1}^{n_b} F_i$$

$$F_i = k_{clutch} \cdot (x_i - x_{sub,i})$$

Each single clutch behaves like a spring of elastic constant k_{clutch} being elongated from its initial relaxed position, where it was right above the contact point with the substrate $x_{sub,i}$, to its final position x_i. The substrate stores elastic energy as results of being pulled, this term that can be found retrieving x_{sub} from the following force-balance equation.

$$k_{sub} \cdot x_{sub} - k_{clutch} \cdot \sum_{i=1}^{n_b} (x_i - x_{sub,i}) = 0$$

(3) The single contribution that each engaged clutch provides to the overall traction force influences the dissociation of the clutch itself following the Bell model:

$$k_{off} = k^*_{off} \cdot e^{(F_i/F_b)}$$

where k_{off} is the effective rate of unbinding of the clutch, k^*_{off} is the value of the rate in the absence of applied forces and F_i and F_b are, respectively, the traction force transduced along the *i*-th clutch and the rupture force of the clutch bond. Alongside the dissociation of the clutches, some of them are undergoing association, relying on the content of integrins (density on cell membrane).

$$k_{on} = k^*_{on} \cdot C_{integrins}$$

Finally, simulations need to take into account the probability ($P_{b,i}$) that, at a given time, the *i*-th clutch is engaged:

$$\frac{dP_{b,i}}{dt} = (1 - P_{b,i}) \cdot k^*_{on} - P_{b,i} \cdot k^*_{off}$$

where $P_{b,i}$ is given by the fraction of bound clutches over their total number $n_b / n_{clutches}$.

As force *F* keeps on building, at a certain point, more and more clutches start to disengage, finally rebooting the system to the completely disengaged state; this behavior is known as “load and fail” and brings the system back to its initial state. This situation occurs when cells are on a soft substrate.

The effective force that, globally, clutches exert (*F*) depends on the substrate rigidity and features an optimum value of k_{sub} that maximizes its value. The force loading rate (meaning the time derivative of *F*) is found to be the central physical quantity that affects mechanosensitivity and depends on the threshold rigidity value. In stiffer substrates ($k_{sub} > k_{optimal}$) forces build up too quickly and clutches are almost instantly disengaged (“frictional slippage” regime), in softer substrates ($k_{sub} < k_{optimal}$) the force loading rate grows so slow that eventually, the lifetime of clutch engagement is surpassed, and clutches unbind. The relation between transmitted force and substrate stiffness hence could be described as a biphasic behavior, which is experimentally dependent also on the cell line (**Fig. 18a**). Parallel to this, also actin retrograde flow (υ) has a biphasic behavior character, reflecting the “damping” effect of the ($1 – F/F_b$) term (**Fig. 18b**).

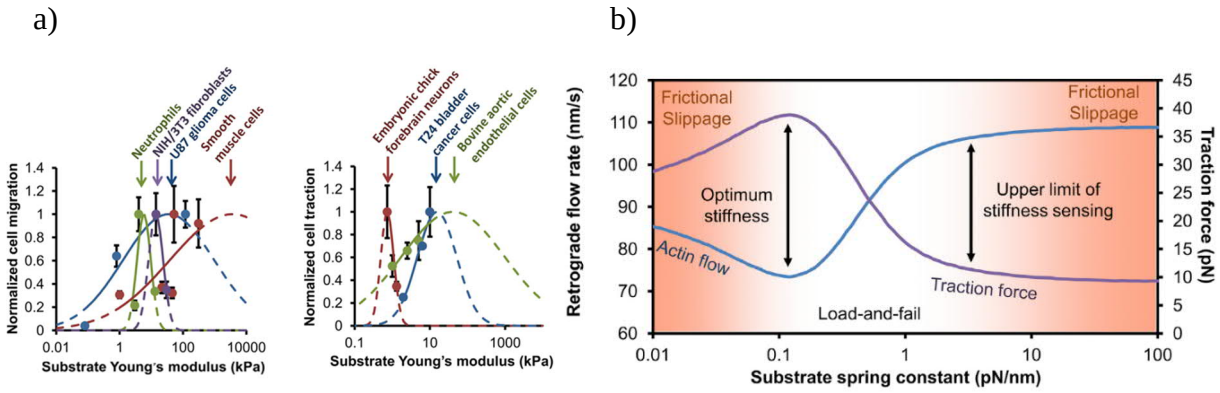

Fig. 18 Cell migration and traction forces Actin retrograde flow and traction force behavior *versus* substrate stiffness (from [52]).

In some systems though, rather than a biphasic behavior, force-substrate stiffness graphs feature a monotonic behavior (**Fig. 19a**) [53]. This behavior has been explained with the partial unfolding of adaptor proteins, *talin* in particular, due to applied mechanical force along the clutch assembly [54] (**Fig. 19b**). After this event, other adaptors proteins establish a connection with actin, reinforcing the bond between internal and external elements of the cell. In these systems, the response of engaged clutches to increasing force loading rates follows the definition of *slip bond* until a certain threshold value: once this threshold is surpassed, it follows the behavior of a *catch bond*. Slip and catch bonds are terms introduced to describe the different response that non-covalently bound molecules oppose to dissociation when a tensile force is applied to the bond. Molecules bound with slip bonds, when pulled apart, are more prone to dissociation since their bound lifetime decreases in response to the mechanical perturbation. Conversely, tensile forces initially strengthen catch bonds increasing their lifetime as a consequence of a new non-covalent allosteric configuration of the molecules, reached after the physical deformation of its pristine state. In this new configuration, the ligand molecule undergoes a conformational change that exposes more binding sites for non-covalent interaction (**Fig. 19c**). This strengthening effect is known as *strain reinforcement*.

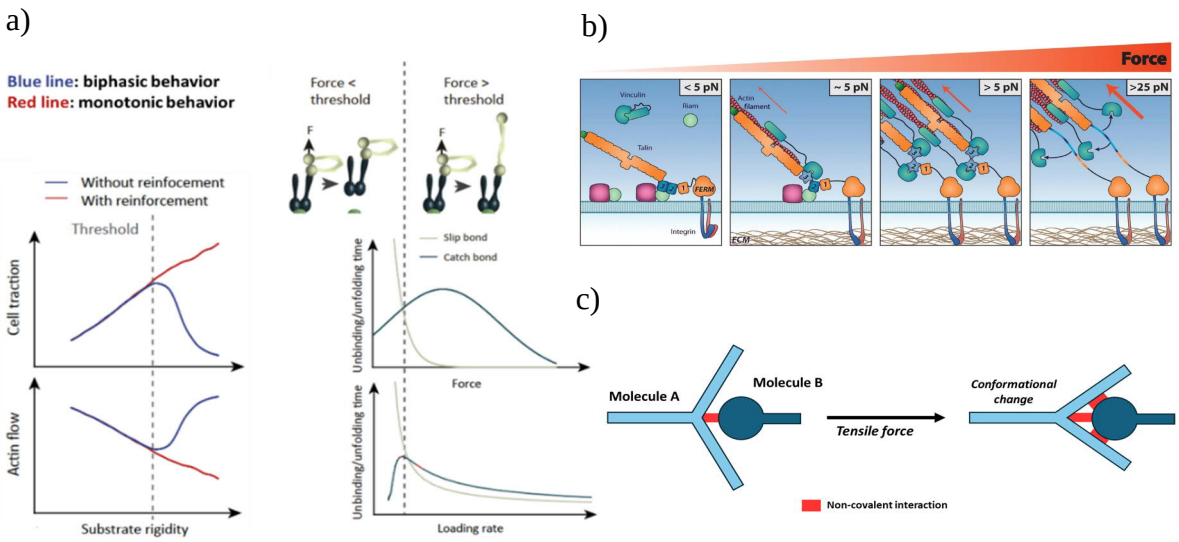

Fig. 19 (a) Force/actin flow behavior *versus* substrate rigidity and catch/slip bond response to force/loading rate (adapted from [53]). (b) Talin unfolding due to applied forces (from [54]) and (c) schematic representation of catch binding allosteric configurations.

Over the past 20 years, the molecular motor-clutch model has become a cornerstone for more complex simulations, and it has been improved to extend its application field, including cell migration and cell spreading studies, in addition to considering various mechanical environments (viscoelastic substrates, stretched substrates, durotaxis, substrates with gradients of stiffness, etc.) and also including contributions from microtubules [55].

1.5 Aims of the Thesis

Below are listed the main lines of inquiry pursued in this Thesis.

1.5.1 Mechanical stimulation of cardiac fibroblasts

Cardiac fibroblasts are approximately up to the 10-25 % [56] of the total number of cells in the heart muscle, second to the most abundant cell type, cardiomyocytes, which are responsible for muscle contraction. Fibroblasts produce matrix components such as collagen type I and III, participating in the regulation of the ECM homeostasis. In physiological conditions these cells retain a quiescent state that, upon injury, is dismissed as a phenotype conversion into *myofibroblasts* is triggered. Inflammatory processes following injury activate a fibroblasts-mediated repair mechanism through an inflammatory, proliferative and maturation phase [57]. In particular, during the proliferative phase activated fibroblasts start secreting collagen which, in the maturation phase, settles into a dense network. Alongside collagen, α-SMA (*smooth muscle actin*) is temporarily expressed in activated fibroblasts; its expression stops after 7-10 days from the injury as cell mature into *matrifibrocytes*, a new fibroblast state suitable for a maturing scar tissue [57]. Allegedly, if dysregulated, this repair mechanism can paradoxically cause the onset of cardiac fibrosis [58], [59], [60] leading to myofibroblasts ultimately being regarded as an ambivalent cell type. To this account, a deep understanding of what makes a mechanical stimulus harmless rather than deleterious, and its consequences on gene expression, is critical.

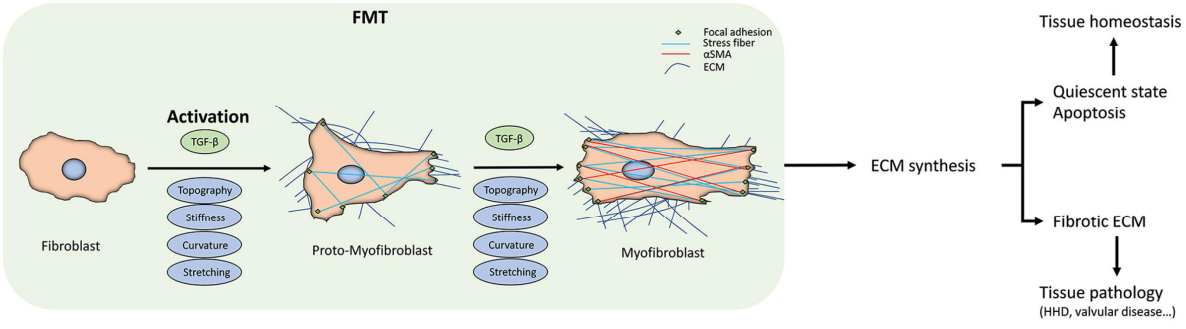

Fig. 20. Schematic representation of the fibroblast-to-myofibroblast transition (from [60]).

The effect of *in vitro* mechanical stimulation in (myo)fibroblasts in both physiological and pathological contexts has been a topic of interest in the mechanobiology field for the last twenty

years. A recent review by Bracco Gartner et al. [61] attempts at summarizing the findings about stretched fibroblasts and mechanically induced cardiac fibrosis pointing out that, to date, results are contradictory. The authors also underline that the wide variability of experimental conditions makes it difficult to reach a well-established consensus and to compare results and considerations.

In this Thesis, we evaluate the effect of cyclic stretching on human cardiac fibroblasts (HCF) cultured on PDMS substrates. Firstly, to throw the basis to interpret and understand how cells respond to a single stimulus, uniaxial cues were applied. Secondly, in order to mimic the occurrence of an injury on pre-aligned fibroblasts, experiments with a change of stretching direction were performed to follow cell reorientation.

1.5.2 Confined migration of glioblastoma cells in quasi-3D environments

When assessing cell movement, 2D *versus* 3D experimental setups are frequently counterposed. Traditionally, bidimensional experiments were the first to be designed to observe cell behavior and, to date, are still largely appreciated as they offer easy access by optical and fluorescent imaging. Despite this, they might oversimplify the complexity of the physiological environment. Depending on the target of the investigation, 2D experiments are divided into single-cell migration assays and collective migration assays (i.e. wound healings): in both cases cells are seeded on flat surfaces, eventually coated with ECM proteins (fibronectin, collagen, genipin, laminin, etc.) to favor cell adhesion.

Even though 3D experiments are closer to the real picture, they are undoubtedly more difficult to manage, both in terms of culturing and substrate preparation but also imaging-wise. 3D assays can be performed using Transwells (commercially available substrates with two compartments divided by a porous membrane which allows cell crossing) or exploiting tridimensional hydrogels/matrices. These setups usually require cells to be permanently marked with fluorescent markers and their imaging becomes quite difficult, so that they usually require confocal microscopy. Another viable option are cell spheroids, cellular aggregates of a spherical shape that are placed on 2D surfaces or inside 3D matrices and whose expansion is observed in time.

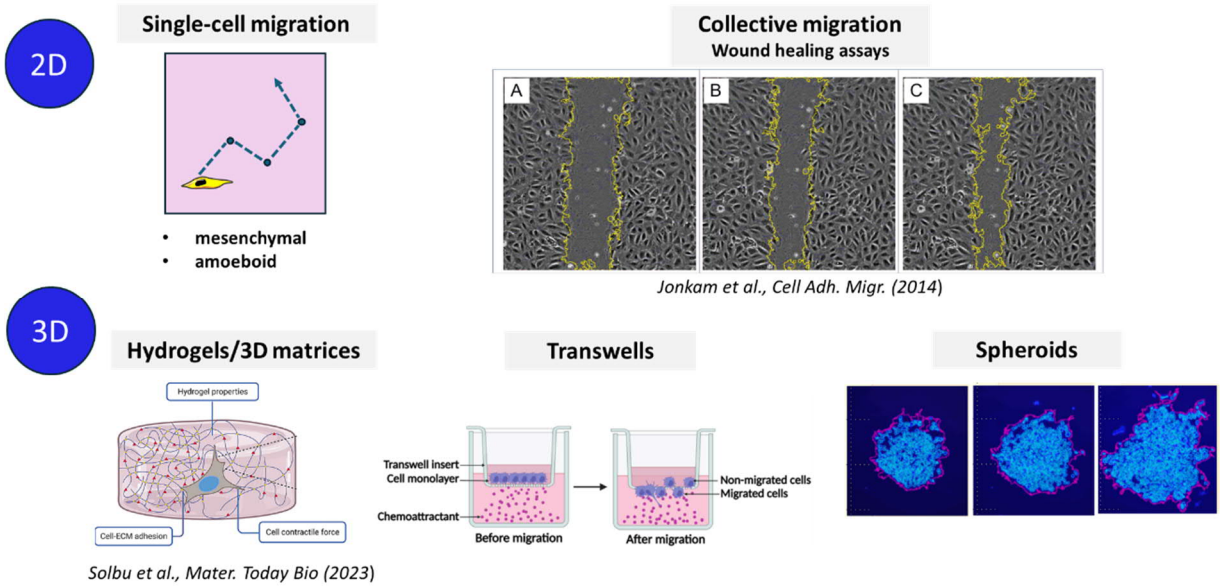

Fig. 21 Schematic representation of the most common migration assays.

The gap between data obtained from 2D and 3D assays is not automatically closed: some articles are in fact pointing out that some cell lines react to specific drugs differently whether in 2D or 3D assays. This is the case of U87MG cells, a model cell line used to study glioblastoma multiforme (GBM), a brain tumor that is renowned for being one of the most aggressive cancers known to date. Despite being rare, with an incidence of less than 10 per 100˙000 people, GBM has a poor prognosis with a survival rate of 14-15 months after the diagnosis. GBM is characterized by high vascularization and invasion capacity within the brain tissues and is known to be quite unresponsive towards pharmacological treatments.

Different studies [62], [63] with U87MG cells find that cells cultured in 2D and 3D respond to blebbistatin in a different manner. Beadle et al. [62] find that blebbistatin does not affect cells cultured on fibronectin-coated glass coverslips, while it slows down cell invasion through pores 3 μm in diameter. Yet, Inukai et al. [63] find blebbistatin to favor invasion through 8-μm pores.

In this work, we propose a quasi-3D environment consisting of a μ-patterned PDMS substrate as a potential alternative to traditional 2D setups and troublesome 3D substrates. This support is then used to culture U87MG cells and test their response to increasing blebbistatin concentrations, as a term of comparison with data published in literature. The μ-patterned substrate is intended to keep an easy access to imaging by the microscope while exposing cells to tridimensional obstacles (micropillars) distancing enough to compress cells as if they were squeezing through a pore.

1.5.3 Characterization of colon cancer invasiveness and metastatic potential related to overexpression of NF-YA isoforms

Tumor progression is ratified by invasive growth and manifestation of metastasis. Invasive growth (invasion) is reported to occur in two fundamentally diverse modalities, classified as collective migration and single-cell migration. In collective migration multicellular groups interconnected by cadherins and gap junctions move altogether, forming cell clusters that feature a leading edge and a trailing edge. Cells at the leading edge resemble mesenchymal cells, producing pseudopodia and interacting with the ECM causing its degradation, “digging” a scaffold for the rest of the cluster to crawl into. In single-cell migration cells move independently as individuals, either adopting the mesenchymal or the amoeboid types of movement.

Mesenchymal migration is characteristic of fibroblasts, so that it is often referred to as “fibroblast-like” migration. It involves the polarization of the cell into an elongated shape, with a leading edge that anchors to the substrate through integrins and focal adhesions and pulls, with the aid of actin stress fibers contraction, the body of cell forward. Epithelial cancer cells that detach from the tumor and start migrating with the mesenchymal mode have undergone the epithelial-to-mesenchymal phenotype transition (EMT). Other peculiarities of this migrating mode are the degradation and remodeling of the ECM, the non-alteration of the shape of the nucleus and the slow rate of migration [64].

Amoeboid migration is reported as the most effective and fast mode of migration for single cells, as it requires no adhesion (hence no ECM degradation) and no continuous cytoskeletal re-organization. Cells assume a round shape and acquire a high deformability, which enables squeezing through small pores by cyclic expansions and contractions of the cell body and the appearance of blebs exploiting hydrostatic pressure. Even nuclei undergo deformation and, in addition to this, together with other organelles, lose their inner position in the cell body [64]. It is worth mentioning that cells can evolve from collective to individual migration and reversibly transition between mesenchymal and amoeboid, as simplified in **Fig. 22**.

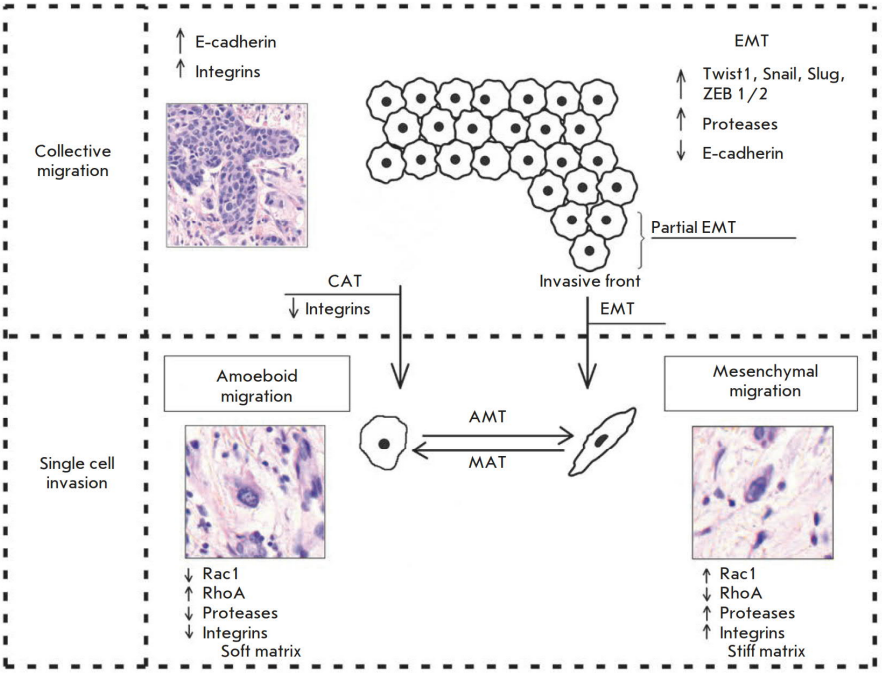

Fig. 22 Schematic representation of the collective and single-cell migration modes of cancer cells (from [64]).

Understanding how tumors progress into further stages by invasion and metastasis is fundamental. This is especially true for cancers such as the colorectal one (CRC), which has been reported by the World Health Organization as one of the most recurring cancers, accounting for a third of the worldwide diagnoses. CRC progression in patients is predicted by the Tumor, Nodes, Metastases (TNM) staging model, where the tumor mass grows in its primary site and, eventually, reaches the lymphatic nodes and blood vessels, ultimately accessing different areas of the body where it can spread as a metastasis. To this account, understanding the molecular and genetic signatures that would allow to anticipate the growth and the onset of metastasis is a central topic in cancer research.

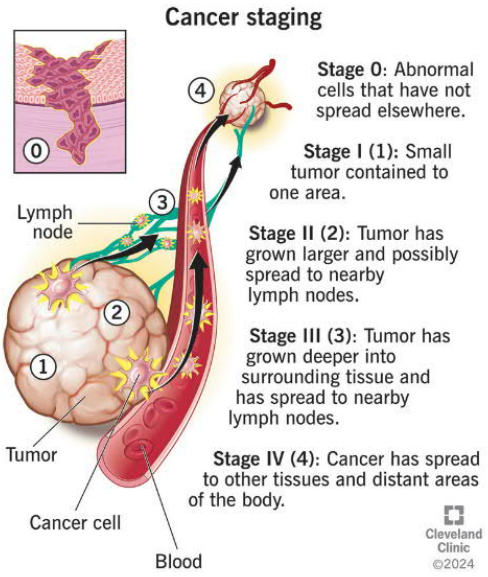

Fig. 23 Schematic representation of the cancer staging system into the tumor, nodes and metastases phases (TNM) (from https://my.clevelandclinic.org/).

To this account, a renowned molecular species whose activity has been studied is the nuclear transcription factor NF-Y, a heterotrimeric protein known to participate in the progression of epithelial cells from benign to malignant. It activates genes belonging to altered genetic pathways that are present in cancer cells [65]. The DNA-binding site of the transcription factor is embedded in the NF-YA subunit, which is available in two alternative splicing: the NF-YA long (NF-YAl) and the NF-YA short (NF-YAs) isoforms, differing for 28/29 aminoacids at the N-terminus [66]. NF-YA is upregulated in a multitude of tumors, such as lung, ovarian, osteosarcomas, breast, gastric and prostate cancers [65] and the NF-YAs/NF-YAl ratio is used as a marker for pro-migration propensity and for aggressive metastaticity, following the epithelial-to-mesenchymal transition (EMT) [67]. Furthermore, the two isoforms were linked with phenotype differences in prostate cancer cells (PC3) [68].

In this Thesis, the collective migration of HCT166 (Human Colon Tumor) cells – adopted as a model for CRC – overexpressing the long and short isoforms of NF-YA was studied in wound healing and spheroids assays. This study aims at understanding the roles of NF-YAs and NF-YAl cells in the invasion and metastasis processes of the colon tumor and, if possible, to establish the molecular signature these proteins confer to the phenotype.

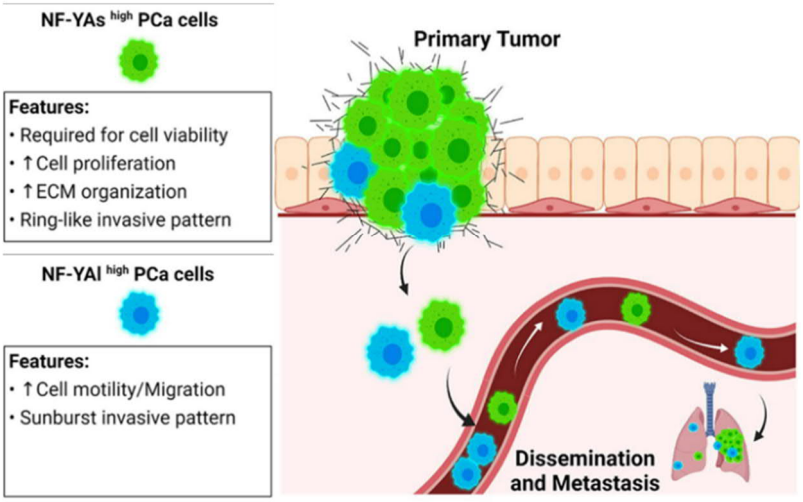

Fig. 24 Schematic representation of the phenotype characteristics of NF-YAs and NF-FYAl expressing prostate cancer cells (adapted from [68]).

Chapter 2 – Methods and Techniques

In **Section 2.1** a general introduction to time-lapse imaging performed with a custom-made stage and with an autofocus algorithm is provided. In **Section 2.2** an extensive description of the components of the cell stretchers-incubators devices is then given, together with the available customizable stretching protocols. **Section 2.3** provides an explanation of the fabrication of PDMS substrates intended for both stretching and confined migration experiments. The calibration and validation of the stretcher devices is thoroughly presented in **Section 2.4**. Following that, **Section 2.5** contains details about cell culturing and the experimental designs carried out for each cell line. Finally, in **Section 2.6** the various parameters accounted as physical observables to characterize the behavior of cells are defined.

2.1 Time-lapse *in vitro* experiments

Time-lapse experiments of *in vitro* cultured cells have been performed exploiting an inverted optical microscope equipped with fluorescence microscopy. The microscope, an Olympus IX70, is equipped with an ORCA-flash 4.0LT camera, a custom-developed motorized stage (**Fig. 25**) and a motorized focus. The microscope can be used with different contrast techniques, such as phase contrast (PC), differential interference contrast (DIC) and bright field (BF).

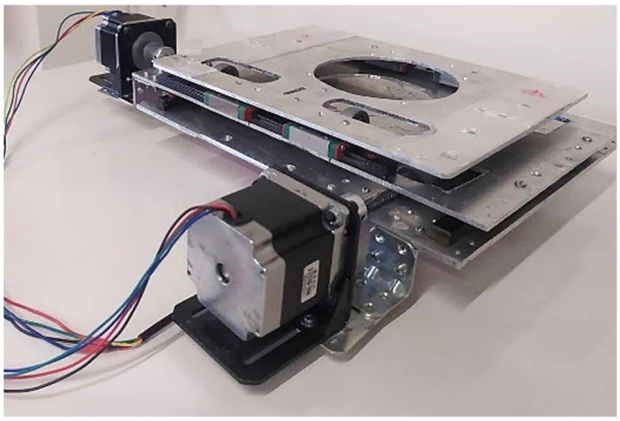

Fig. 25 Picture of the custom-made stage for the inverted optical microscope.

The motorized stage and image acquisition are controlled by an Arduino Mega microprocessor and a custom-made Python code that both move the stage through the different chosen positions and rotate the focus knob in order to acquire *z*-stack images. The stage movement and the focus

knob rotation are enabled by two different NEMA23 stepper motors (*x*, *y*) and a NEMA17 stepper motor (*z*). The acquired *z*-stack is analyzed to find the best focused slice by a custom-made algorithm, included in the Python code, which identifies the slice with the maximum contrast [69]. The same Arduino Mega microprocessor can provide, if required, the stretching stimulus through an additional set of stepper motors, belonging to the cell stretcher devices, and eventually pause it to allow image acquisition (**Fig. 26**).

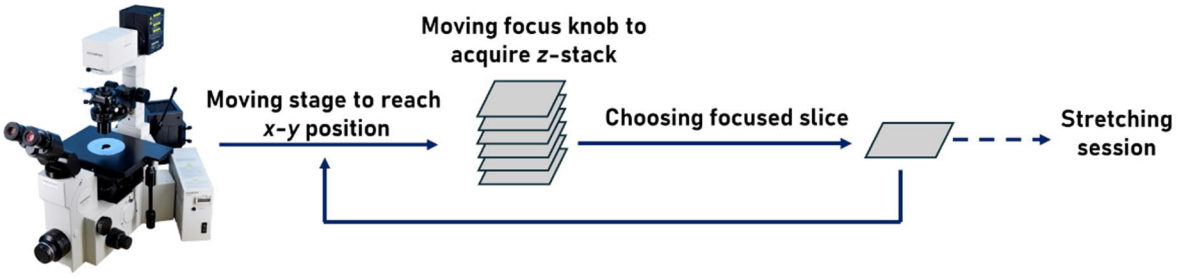

Fig. 26 Schematic representation of the cycle of image acquisition/stretching session (if present). Every step is handled by the Arduino Mega microprocessor and the dedicated Python script.

2.2 Description of the stretcher devices and user-customizable protocols

The stretcher devices were built in the NanoBioLab with a *do-it-yourself* approach, following the same setup previously adopted and published in [39]. The devices were designed to be compatible with time-lapse acquisition at the optical microscope, so that they could be placed on the motorized stage while allowing cells incubation. The devices are in fact able to keep cells at 37 °C, 95-100% RH and in a 5% CO_2 atmosphere, maintaining the correct parameters through a feedback system controlled by an Arduino Uno microprocessor that regulates temperature and gas supply over time (see **Fig. 27**).

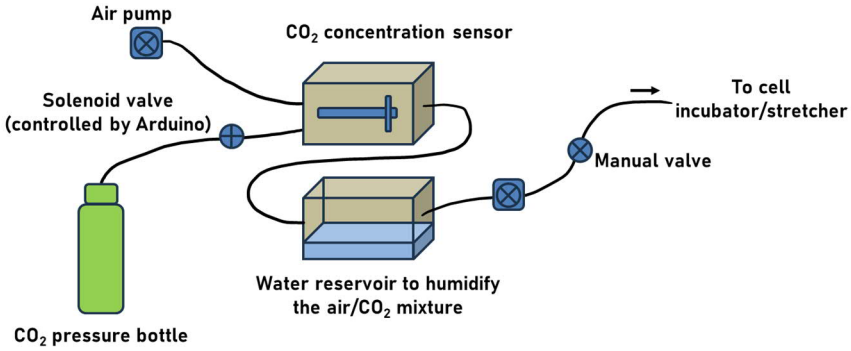

Fig. 27 Schematic representation of the feed-back system that regulates T, RH and CO_2 supply.

All devices are equipped with:

- an aluminum external chassis;
- a transparent lid with a central ITO glass window whose switching on/off is regulated by the Arduino board to prevent water condensation on the lid;
- a T and RH internal sensor (DTH 22);
- different water reservoirs heated by thick film resistors (TFR 28 Ω) alimented by an external power supply (12 V max), that provide heating and humidity in the chamber;
- a gas inlet that introduces the CO_2-enriched air mixture into the chamber (CO_2 Adafruit sensor);
- a transparent central lodge which is placed right above the objective of the inverted microscope that hosts the PDMS substrate (see **Fig. 28**);
- a series of clamping sites and movable barriers that allows the transmission of the mechanical signal from the stepper motors (which are external to the chassis) to the PDMS substrate;
- a set of NEMA23 stepper motors coupled with DM542 drivers (in configuration OFF-ON-ON-ON which provides 1 step = 0.02 mm of lateral displacement);
- electrical connections to the Arduino Mega microprocessor that pilots the movement of the motorized stage to perform the autofocus algorithm by a Python interface.

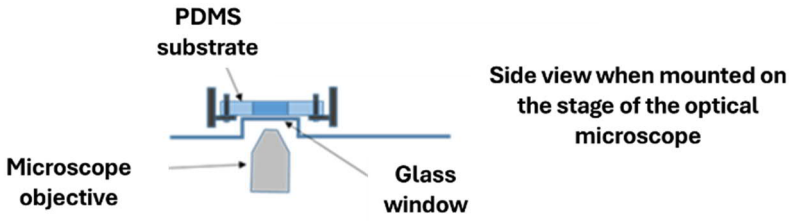

Fig. 28 Schematic representation of the central lodge for the PDMS substrate and the relative position to the microscope objective.

These features, and the case-specific geometry adopted for each different stretcher are exemplified in **Fig 29**.

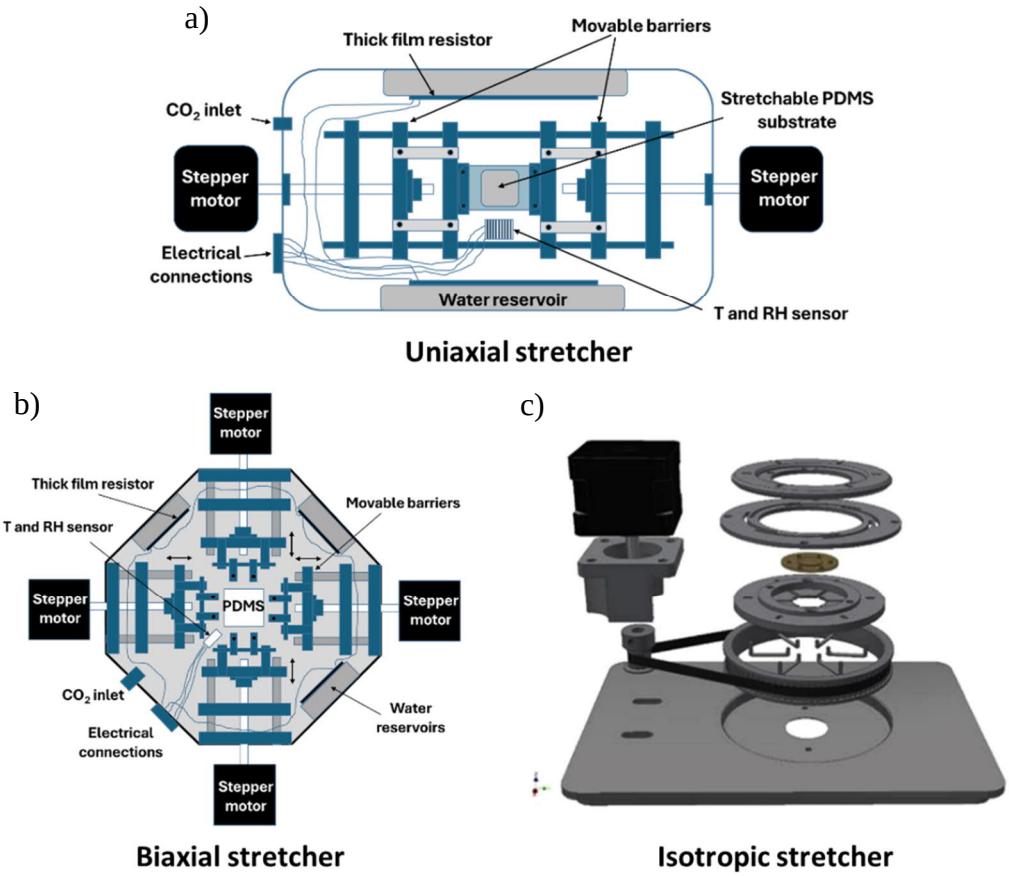

Fig. 29 Schematic representation of the main components of the different stretchers: (a) uniaxial (from [39]), (b) biaxial and (c) isotropic (from [70]).

Stretching protocols

A dedicated LabVIEW panel allows the user to choose the parameters to feed to the stepper motors of the stretcher devices, customizing the signal waveform and setting its amplitude and frequency. **Fig. 30** shows an example of the triangular, square and sinusoidal signals at 100-steps amplitude and 1 Hz frequency.

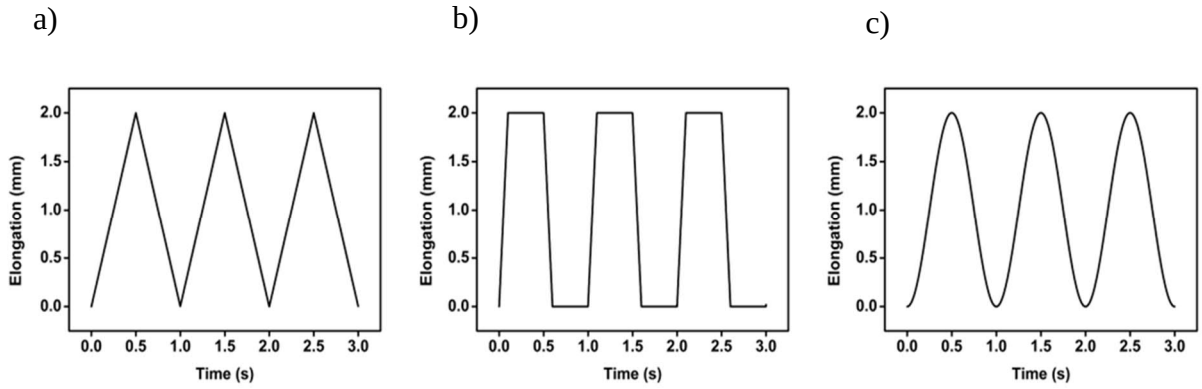

Fig. 30 Example of the triangular (a), square (b) and sinusoidal (c) signals. The *y* axis represents the elongation provided per side to the PDMS substrate.

2.3 Fabrication of PDMS substrates

Polydimethylsiloxane – PDMS – is an elastomeric polymer featuring different properties that make it the most suitable material for stretching experiments coupled with time-lapse imaging by optical microscopy. Over the last decades, PDMS has been widely used in biophysics and in the bioengineering field. The polymer is, in fact, optically transparent, permeable to gases, biocompatible and appropriate for cell seeding, its elastic modulus can be fine-tuned by selecting the relative amounts of pre-polymer and crosslinker components and it is resistant to oxidation, to temperature variations and aging and also electrically insulating.

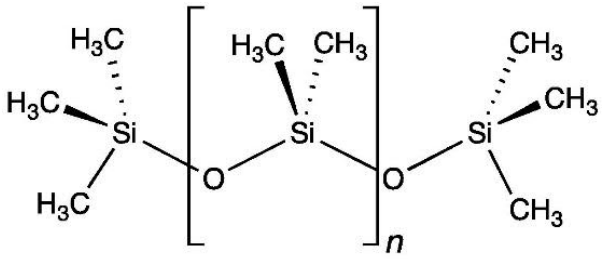

Fig. 31 Structure of the PDMS polymer.

The material can be easily synthesized from commercially available two-component kits, the base monomer and the crosslinker, which upon mixing polymerize even at room temperature. The mixing ratio of the two components determines the elastic modulus *E* of the polymerized material and different protocols – also mixing pre-polymers from different kits, being the Sylgard 184 and Sylgard 527 (Dow Corning) the best known – are available in literature to obtain the desired *E* value [71].

In this work, the Sylgard 184 kit was used following two different recipes: in the case of PDMS substrates for stretching experiments the 20:1 ratio was chosen (*E* = 1.56 MPa [72]), while to realize μ-pillared substrates the typical 10:1 ratio (*E* = 2.1 MPa [73]) was preferred. The liquid mixture obtained by mixing the two components needs to be degassed in a vacuum chamber for about 20-40 min; it is poured then into a PVC mold (**Fig. 32a**) and degassed again for another 20-40 min to remove air bubbles. Afterwards, the mold is placed in a stove at 70-80 °C for 2 h, fastening the polymerization process. The cured PDMS substrate – in **Fig. 32b** the substrates for the different stretchers – is then demolded and cleaned with ethanol and a nitrogen flux. This technique is known as *replica molding* and allows to create as many substrates as wanted from the same master mold.

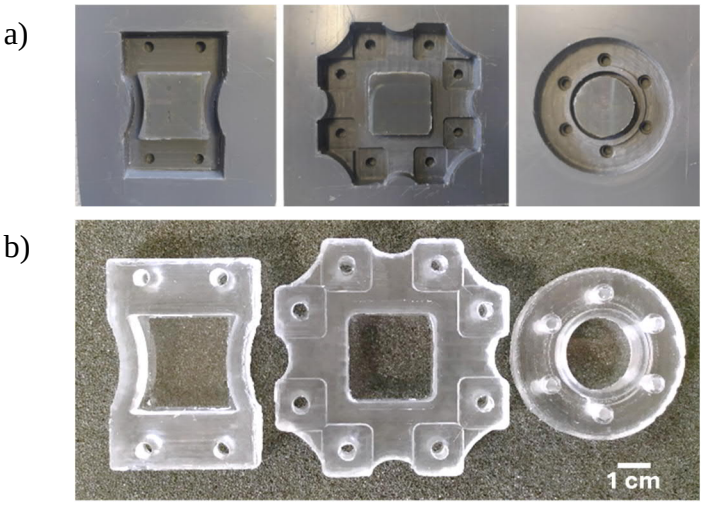

Fig. 32 (a) Pictures of the different CNC-milled PVC molds to cast PDMS. (b) Picture of PDMS substrates for the different stretcher devices.

2.3.1 PDMS substrates with µ-patterns

A line of inquiry investigated in this work includes cells migration on a micropatterned PDMS substrate. The PVC mold used to shape the liquid PDMS included – in the center of the well that hosts cells – a silica wafer with µ-holes.

The silica wafer was prepared by Reactive Ion Etching, a technique that allows to engrave holes in a thin layer of photoresist pre-polymer covering a silica wafer. The chip is superimposed by the desired pattern and exposed to the UV light so that only some regions of the pre-polymer crosslink and harden. The non-exposed pre-polymer remains liquid and is then removed by a proper developer solvent which unveils the underlying pattern.

The portions of wafer that are not covered by the polymerized resist are susceptible to engraving by the plasma: small depths will be dug in these sites, producing µ-holes (**Fig. 33** and **Fig. 34**). Subsequently, a superficial treatment with siliconizing agents – such as APTES – functionalizes the wafer so that it becomes inert and hydrophobic, suitable for PDMS pouring and demolding.

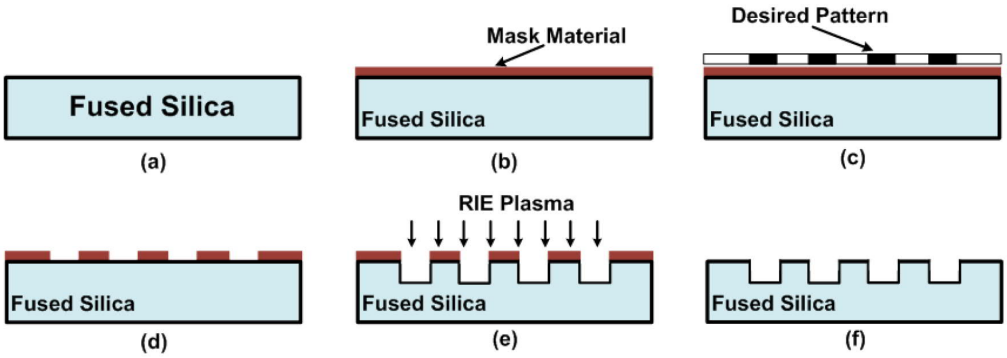

Fig. 33 Schematic representation of the different steps of RIE lithography (from [74]).

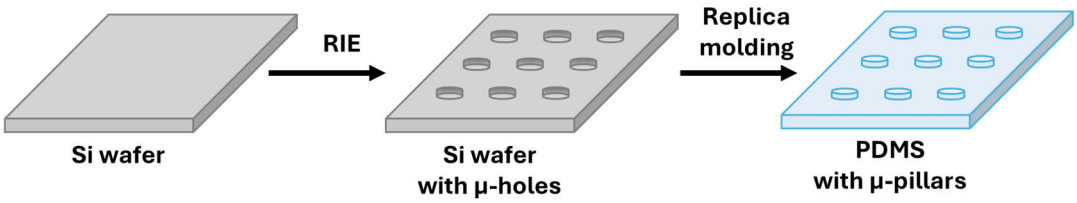

Fig. 34 Schematic representation of the µ-holed silicon master and the replica molding process.

A PVC mold embedded with the μ-holed pattern is then used as master mold to produce PDMS substrates by replica molding as previously described. In **Fig. 35** we can see images of the PDMS μ-pillars ($h = \phi$ = 8 μm, center-to-center distance = 15 μm) acquired by Scanning Electron Microscopy (SEM) and optical microscopy.

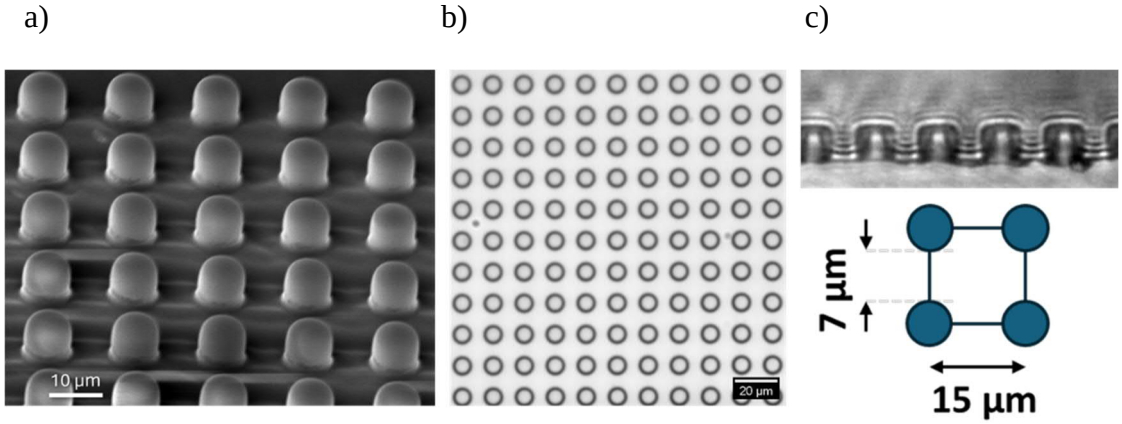

Fig. 35 Images of the PDMS μ-pillars after fabrication acquired at the SEM (a) and at the optical microscope, top view (b) and side view (c).

2.4 Calibration and validation of the stretcher devices

Prior to application, the stretcher devices need calibration, in order to check for the effective strain produced by the stepper motors as well as to choose the proper experimental conditions. Calibration of the devices was carried out experimentally and data was analyzed with a custom-made Python script and then validated by Finite Element Method simulations.

2.4.1 Experimental calibration and theoretical approaches to calculate ε

The devices were experimentally calibrated directly on the microscope stage: a 20:1 PDMS substrate was mounted and clamped in the central lodge of the stretchers and deformed by applying gradually incremented steps to the stepper motors. On the surface of the PDMS, a layer of nanobeads (0.2-0.5 μm in diameter) was added to act as fiducial spatial markers to be observed by the microscope. The images in **Fig. 36** depict how beads appear during the process (for a better visualization, triads of points are highlighted as green triangles).

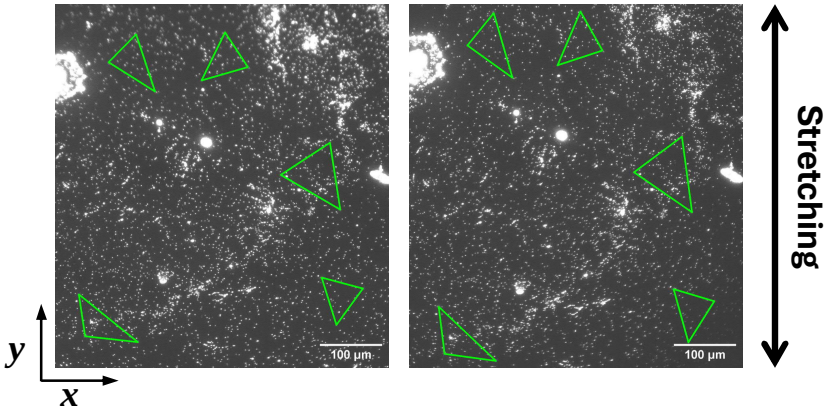

Fig. 36 Example of triads of points considered for the experimental calibration of the uniaxial stretcher. The panel on the left portrays the initial unstretched condition; on the right, the stretched condition (at 140 steps, along the *y* axis).

The theory of calibration hereby presented recalls what proposed by Ragazzini et al. [39]. In particular, the main property observed to calibrate the devices is strain, as it is largely addressed as one of the main mechanical properties that cells respond to in cyclic stretching experiments [75].

Strain is commonly defined in the engineering field as:

$$\varepsilon = \frac{\Delta L}{L_0}$$

where ΔL represents the elongation of an object and L_0 its initial length.

In a slightly more complex scenario, where a two-dimensional object is infinitesimally stretched, one can define strain along the *x* and *y* axes as:

$$\varepsilon_{xx} = \frac{\partial \boldsymbol{u}_x}{\partial \boldsymbol{X}} \quad ; \quad \varepsilon_{yy} = \frac{\partial \boldsymbol{u}_y}{\partial \boldsymbol{Y}}$$

where $\boldsymbol{u}$ is the displacement vector that connects the point $P(x, y) \equiv P(\boldsymbol{X})$ to its new position $P'(x', y') \equiv P(\boldsymbol{x})$, being $\boldsymbol{X}$ and $\boldsymbol{x}$ the vectors of initial and final coordinates respectively (**Fig. 37**).

The displacement vector $\boldsymbol{u}$ is hence defined as $\boldsymbol{u} = \boldsymbol{x} - \boldsymbol{X}$.

The strain ε can be described as a tensor, where ε_{xy} and ε_{yx} are terms related to *shear* (γ) and, in the case of pure strain, are null.

$$\boldsymbol{\varepsilon} = \begin{pmatrix} \varepsilon_{xx} & \varepsilon_{xy} \\ \varepsilon_{yx} & \varepsilon_{yy} \end{pmatrix} = \begin{pmatrix} \dfrac{\partial \boldsymbol{u_x}}{\partial \boldsymbol{X}} & 0 \\ 0 & \dfrac{\partial \boldsymbol{u_y}}{\partial \boldsymbol{Y}} \end{pmatrix}$$

The strain matrix, expressed as the Green-Cauchy tensor, is associated to the gradient deformation matrix $\boldsymbol{F}$ as follows:

$$\boldsymbol{\varepsilon} = \frac{1}{2}(\boldsymbol{F} + \boldsymbol{F}^T) - \boldsymbol{I}$$

being $\boldsymbol{F}$ defined as:

$$\boldsymbol{F} = \frac{\partial \boldsymbol{x}}{\partial \boldsymbol{X}} = \frac{\partial(\boldsymbol{X} + \boldsymbol{u})}{\partial \boldsymbol{X}} = \boldsymbol{I} + \frac{\partial \boldsymbol{u}}{\partial \boldsymbol{X}} = \boldsymbol{I} + \boldsymbol{\varepsilon}$$

it contains terms due to strain, shear and rotation which need to be distinguished. To do so, $\boldsymbol{F}$ can be written as the product of $\boldsymbol{R}$, matrix of rotation, and $\boldsymbol{U}$, matrix of stretching. In this way, the product $\boldsymbol{F^T} \cdot \boldsymbol{F}$ becomes independent of the rotation transformation, as shown below:

$$\boldsymbol{F^T} \cdot \boldsymbol{F} = (\boldsymbol{R} \cdot \boldsymbol{U})^{\boldsymbol{T}} \cdot (\boldsymbol{R} \cdot \boldsymbol{U}) = \boldsymbol{U^T} \cdot \boldsymbol{R^T} \cdot \boldsymbol{R} \cdot \boldsymbol{U} = \boldsymbol{U^T} \cdot \boldsymbol{U}$$

The calibration process implemented by a custom-developed Python code previously published by our group [39] exploits these relationships to evaluate $\boldsymbol{F}$, $\boldsymbol{F^T}$, $\boldsymbol{R}$ and $\boldsymbol{U}$ in order to retrieve the Green-Cauchy strain matrix $\boldsymbol{\varepsilon}$ and diagonalize it to obtain $\varepsilon_{x'x'}$ and $\varepsilon_{y'y'}$. The $\varepsilon_{x'x'}$ and $\varepsilon_{y'y'}$ components obtained after diagonalization are along two perpendicular directions *x'* and *y'*, which are the main and secondary strain directions. The angle of rotation between the reference system (*x*-*y*) and the new reference system (*x'*-*y'*) is then used to evaluate the zero-strain direction (see **Section 2.4.2**).

The input data introduced in the Python script are the position coordinates of a set of nanobeads which were tracked during the experimental calibration.

2.4.2 Zero-strain direction

In addition to the evaluation of the strain value ε, the direction at which the strain results null, defined as $\theta_{zero\text{-}strain}$, was calculated by the same Python script.

First of all, the *x'*-*y'* reference system based on the main and secondary directions of strain is adopted, as a rotation of angle θ of the laboratory reference system *x*-*y* (**Fig. 37**).

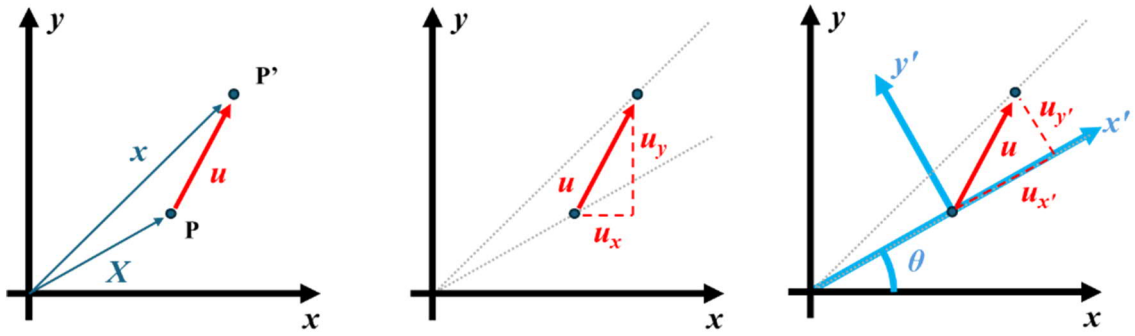

Fig. 37 Schematic representation of the change of reference system from the laboratory frame (*x*-*y*) to the strain-defined one (*x'*-*y'*).

The displacement vector ***u***, previously introduced, can be re-written as:

$$u_x = u_{x'} \cdot cos\theta - u_{y'} \cdot sin\theta$$

$$u_y = u_{x'} \cdot sin\theta + u_{y'} \cdot cos\theta$$

Hence leading to a more compact expression:

$$\begin{pmatrix} u_x \\ u_y \end{pmatrix} = \begin{pmatrix} cos\theta & -sin\theta \\ sin\theta & cos\theta \end{pmatrix} \cdot \begin{pmatrix} u_{x'} \\ u_{y'} \end{pmatrix}$$

$$\begin{pmatrix} u_{x'} \\ u_{y'} \end{pmatrix} = \begin{pmatrix} cos\theta & sin\theta \\ -sin\theta & cos\theta \end{pmatrix} \cdot \begin{pmatrix} u_x \\ u_y \end{pmatrix}$$

We define the rotation matrix ***R*** as:

$$\boldsymbol{R} = \begin{pmatrix} cos\theta & sin\theta \\ -sin\theta & cos\theta \end{pmatrix}$$

so that the strain matrix ***ε***, defined in the new reference system becomes ***ε'***:

$$\boldsymbol{\varepsilon'} = \boldsymbol{R}\,\boldsymbol{\varepsilon}\,\boldsymbol{R}^{\boldsymbol{T}}$$

$$\begin{pmatrix} \varepsilon_{x'x'} & \varepsilon_{x'y'} \\ \varepsilon_{y'x'} & \varepsilon_{y'y'} \end{pmatrix} = \begin{pmatrix} cos\theta & sin\theta \\ -sin\theta & cos\theta \end{pmatrix} \begin{pmatrix} \varepsilon_{xx} & \varepsilon_{xy} \\ \varepsilon_{yx} & \varepsilon_{yy} \end{pmatrix} \begin{pmatrix} cos\theta & -sin\theta \\ sin\theta & cos\theta \end{pmatrix}$$

$$\varepsilon_{x'x'} = \varepsilon_{xx} \cdot cos^2\theta + \varepsilon_{yy} \cdot sin^2\theta + 2\varepsilon_{xy} \cdot sin\theta\, cos\theta$$

$$\varepsilon_{y'y'} = \varepsilon_{xx} \cdot sin^2\theta + \varepsilon_{yy} \cdot cos^2\theta - 2\varepsilon_{xy} \cdot sin\theta\, cos\theta$$

In absence of shear deformation, the term ε_{xy} is equal to 0, so that $\varepsilon_{x'x'}$ becomes:

$$\varepsilon_{x'x'} = \varepsilon_{xx} \cdot cos^2\theta + \varepsilon_{yy} \cdot sin^2\theta$$

The Python script carefully evaluates the ε_{xy} and ε_{yx} terms during the calibration procedure, ensuring they are significantly close to zero.

Trying to express $\varepsilon_{x'x'}$ as a single function of $sin\theta$ one obtains:

$$\varepsilon_{x'x'} = \varepsilon_{xx} + (\varepsilon_{yy} - \varepsilon_{xx}) \cdot sin^2\theta$$

$$\varepsilon_{x'x'} = \varepsilon_{xx} \cdot \left[1 - \left(1 - \frac{\varepsilon_{yy}}{\varepsilon_{xx}}\right) \cdot sin^2\theta\right]$$

To nullify the term $\varepsilon_{x'x'}$ the parenthesis that multiplies ε_{xx} needs to be null, which occurs for a specific value of $\theta = \theta_{zero\text{-}strain}$:

$$\left[1 - \left(1 - \frac{\varepsilon_{yy}}{\varepsilon_{xx}}\right) \cdot sin^2\theta\right] = 0$$

$$sin^2\theta = \frac{1}{1 - \frac{\varepsilon_{yy}}{\varepsilon_{xx}}}$$

$$\theta_{zero-strain} = arcsin\sqrt{\frac{1}{1 - \frac{\varepsilon_{yy}}{\varepsilon_{xx}}}} = arctg\sqrt{-\frac{\varepsilon_{xx}}{\varepsilon_{yy}}}$$

2.4.3 Validation by FEM simulations

Finite Element Method simulations were adopted as a validation test in order to check the goodness of the experimental calibration. The different geometries of the PDMS substrates were designed with FreeCad and were virtually deformed exploiting the *3D Simulations/Thermal and Mechanics* module of the CST Studio software. The designs were simulated applying the following parameters of density, Young modulus and Poisson ratio (ρ = 1090 kg/m^3, E = 1.56 MPa, ν = 0.499) in order to reproduce a material corresponding to PDMS 20:1; a total of 50 tetrahedral meshes was chosen.

The strain components extracted from the simulations were then compared to the experimental ones.

2.5 Cell culturing and experimental outlines

In this Section the specific culturing conditions adopted for each cell line and their relative experiments are detailed.

2.5.1 Human Cardiac Fibroblasts (HCF)

Human Cardiac Fibroblasts (Innoprot P10453-IM) were cultured using the specific FM-2 medium (CliniSciences) with addition of 1% Fibroblast Growth Supplement-2 (FGS-2, Cat #2382), 1% penicillin/streptomycin and 5% of fetal bovine serum (FBS), designed for optimal growth. When cultured on plates and flasks, the surface of the substrates was coated with poly-L-lysine 10 mg/mL (CliniSciences).

For stretching experiments, cells were seeded on PDMS substrates, but prior to seeding the surface of the polymer was functionalized in order to enhance its hydrophilicity. This was achieved with a mild plasma treatment (Diener Fempto, 40W), where a mixture of high energy ions and molecules (plasma) obtained from a N_2/air mixture impacts the surface of PDMS for 2 min, cleaning it while forming superficial silanol (Si-OH) groups. After that, the PDMS was sterilized by 2 h of UV exposure and then incubated with 0.01 mg/mL sterile fibronectin (Sigma-Aldrich) at 37 °C for 1 h. The fibronectin solution was then removed and an aliquot of 2 mL of cell suspension with an approximate density of $10^{\cdot}000$ cells/cm^2 was placed in the PDMS well and incubated for at least 24 h to allow cells to adhere.

Outline of the stretching experiments with HCF

In this work, stretching experiments performed with HCF cells were designed with a constant maximum amplitude of 100 steps (hence a 2 mm elongation per side) and a frequency of either 1 or 0.3 Hz. This stretching protocol was adopted for both the uniaxial and the biaxial stretcher.

In particular, in uniaxial experiments, a single stretching session with the duration of 3 h was imposed to cells. The effect of different waveforms was scouted imposing triangular, square and sinusoidal signals with f = 1 Hz. In order to understand the effect of a different frequency, a low-frequency triangular signal, with f = 0.3 Hz, was tested.

For biaxial experiments, two stretching sessions were performed to investigate the effect of a sudden change in the direction of stimulation. Firstly, cells were stretched along the *x*-motor

axis for 3 h, secondly, a change in the stretching direction was applied to deform cells along the *y*-motor axis. We defined this experimental setup as “90°-inversion experiments”. These experiments were carried out applying the triangular signal at 100-steps amplitude and with 1 and 0.3 Hz frequencies; both maximum amplitude and frequency were kept constant for the whole duration of the experiment, before and after the “inversion time”. The second stretching session could either last 30 min or 1 h, to analyze aspects of the re-orientation kinetics; after such time cells were fixed with PFA 4% in PBS and stained for immunofluorescence.

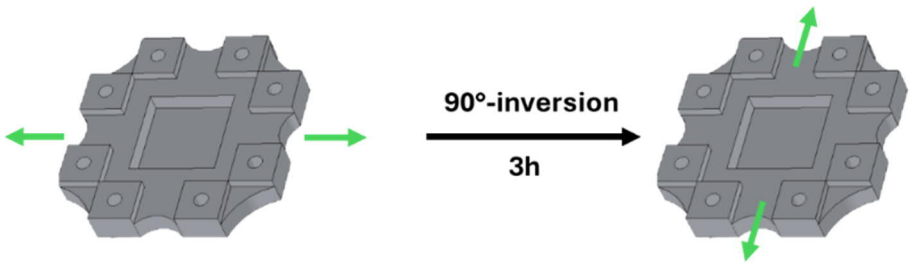

Fig. 38 90°-inversion experiments performed with the biaxial stretcher.

Images were acquired every 4 min during the experiments, achieving a total of 45 frames in experiments with the uniaxial cell stretcher and 45 + 15 frames (respectively before and after changing the stretching axis) in experiments with the biaxial cell stretcher to be processed for the analysis.

A synthetic overview of the experiments carried out with the uniaxial and biaxial stretcher devices is given in **Table 1** and **Table 2**.

Table 1 Summary of the experiments with HCF cells performed with the uniaxial stretcher.

Waveform	Amplitude	*f*	Duration
T	100 steps	1 Hz	3 h
Q	100 steps	1 Hz	3 h
S	100 steps	1 Hz	3 h
T	100 steps	0.3 Hz	3 h

Table 2 Summary of the experiments with HCF cells performed with the biaxial stretcher.

Waveform	Amplitude	*f*	Duration (1st session)	Duration (2nd session)
T	100 steps	1 Hz	3 h	1 h
T	100 steps	1 Hz	3 h	30 min
T	100 steps	0.3 Hz	3 h	1 h
T	100 steps	0.3 Hz	3 h	30 min

2.5.2 Glioblastoma Multiforme (U87MG)

Glioblastoma Multiforme U87MG cells (ATCC) were cultured in DMEM medium (Euroclone) with 1% penicillin/streptomycin (Euroclone), 1% L-glutamine, 1% non-essential aminoacids and 1% sodium piruvate (Euroclone). When cultured on the PDMS, the same treatment adopted in the previous Section was carried out to enhance surface hydrophilicity and cell adhesion. The PDMS was exposed to UV light for 2 h and incubated with sterile fibronectin 0.01 mg/mL (Sigma-Aldrich) at 37 °C for 1 h. Once the fibronectin solution was removed a 2-mL aliquot of cell suspension with a density of 20˙000 cells/mL was deposited into the PDMS well and allowed to adhere for 48 h prior to the time-lapse imaging.

Outlines for migration experiments with U87MG

In this Thesis, U87MG cells were treated with 1*g* and blebbistatin in order to perform different migration experiments. Below are the specific conditions adopted.

(i) *Cell migration in presence of 1g*

Experiments relative to the single-cell migration in presence of the 1*g* drug (synthetized and purified by Prof. Roberta Ettari, University of Messina, Italy) [8], [9], [10] were carried out in non-treated 6-well plates, in the absence of fluorescence staining. Cells were seeded at 15˙000 cells/mL density and let adhere for 24 h.

To evaluate collective migration wound healing assays were performed culturing cells at 80-90% confluency in 6-well plates. Prior to imaging, a gap in the cell monolayer was scratched using a p200 tip.

Right before image acquisition, the cell medium was replaced by an aliquot of medium containing different volumes of a 100 mM solution of the drug 1*g* in DMSO. For single-cell

migration, the tested 1*g* concentration in solution are 1 and 2 μM; instead, for wound healings a 20 μM concentration was used.

Imaging was carried under the optical microscope (10x/20x, Phase Contrast) in a custom-made cell incubator designed to host well plates while allowing live imaging. The incubator was developed by the NanoBioLab [69] and is equipped with the same features as listed in **Section 2.2**, stepper motors aside. Images were acquired every 6 minutes. For single-cell migration experiments, imaging lasted 6 hours, resulting in a total of 60 frames, while for wound healing experiments, imaging continued for up to 24 hours, yielding a total of 240 frames for analysis.

(ii) *Confined migration experiments with blebbistatin*

For experiments carried out with μ-patterned PDMS substrates, nuclear staining was required: before starting imaging under the microscope, the cell medium was thus changed with a medium aliquot (2 mL) containing 1-2 μL of 1 mg/mL Hoechst 33342 solution in PBS (Thermo Fisher). The marker was allowed to complete nuclei staining for at least 15-20 min in the dark before starting image acquisition. After this time, the medium was again changed with a blebbistatin-containing medium aliquot (Sigma Aldrich); the tested concentrations are 5, 10, 15 and 20 μM.

Imaging was carried out under the optical microscope (20x, Phase Contrast) with, inserted, the fluorescent DAPI cube. Image acquisition occurred every 6 min and was performed for 6 h, collecting 60 frames for the analysis.

2.5.3 Human Colon Tumor (HCT116)

HCT166 cells (ATCC #CCL-247) overexpressing NF-YAl and NF-YAs were transfected [76] and selected as described in [65]. For wound healing assays cells were seeded into Ibidi culture-inserts (#80209 Ibidi GmbH) and cultured up to confluence. Prior to imaging at the optical microscope the insert was removed and a gentle wash with PBS 1x was performed, then complete IMDM medium was replenished [65].

3D multicellular tumor spheroids (MTSs) of HCT166 overexpressing cells were prepared by plating 5˙000 cells into 96-well ultra-low attachment (ULA) plates with round bottom (#7007 and #4515, Corning, USA) in 150 μL of ice-cold complete medium with 1 mg/mL Matrigel matrix (#354248, Corning, USA). After centrifuging for 10 min at 1000g and 4 °C,

MTSs were incubated for 7 days, during which 50 µL of fresh complete medium were added every 3 days. MTSs were gently collected using a cut p200/p1000 pipette tip to help preserving their morphology and were washed with 1X PBS. Spheroids were deposited with a 50 µL drop in 96-well plates coated with collagen matrix. The collagen matrix was prepared mixing 3 mg/mL rat tail collagen I (#7341085, Corning, USA) with NaOH, $NaHCO_3$ and IMDM medium, in ice-cold conditions at pH = 7 – 8. 100 µL of the matrix were dispensed in the well plates and let polymerize at 37 °C for 30 min, prior to transferring the spheroids [65].

In both cases, imaging was performed using the 10x objective, with images acquired every 8 minutes. Wound healing experiments lasted approximately 30 h, collecting around 200 frames, while spheroids were observed for 48 h, resulting in a total of 360 frames. Wound healing was monitored using phase contrast, while spheroids were observed in bright field modality.

2.6 Experimental parameters for the characterization of cell behavior

2.6.1 Single-cell migration

In this work, the analysis of the migration of cells without fluorescent markers was performed using the ImageJ *Manual Tracking* plugin (https://imagej.net/ij/plugins/track/track.html), whereas for marked cells the *TrackMate* plugin (https://imagej.net/plugins/trackmate/) was used in combination with a slightly modified version of the Google Colab notebook *CellTracksColab – TrackMate* (https://cellmig.org/software/, [77]). In **Fig. 39** an example of output of the Manual Tracking is proposed, while in **Fig. 40** a TrackMate tracking output is reported.

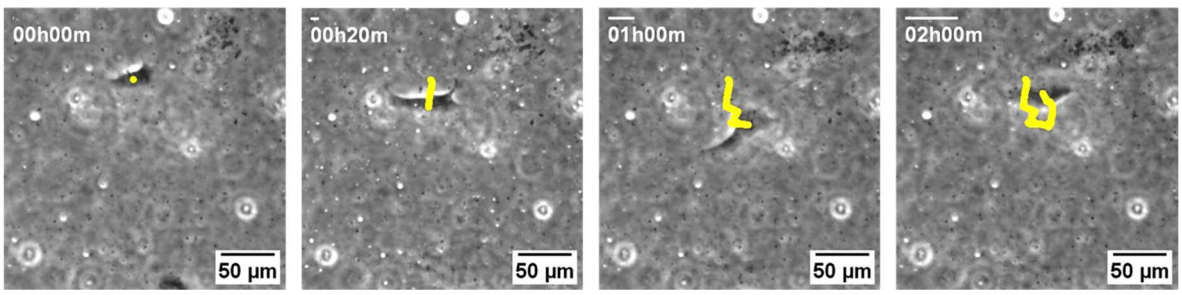

Fig. 39 Image sequence showing the trajectory of a HCF cell migrating.

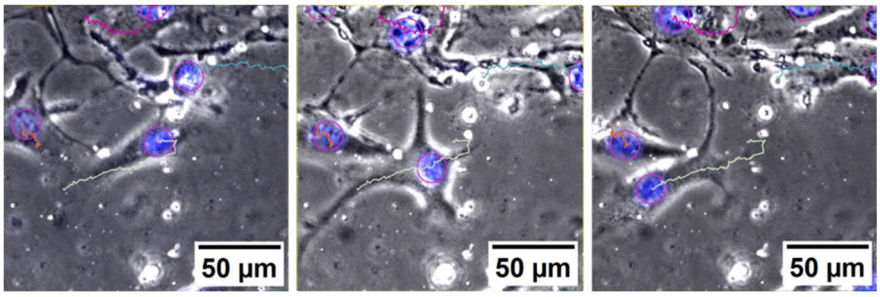

Fig. 40 Image sequence showing the output of the TrackMate plugin, performed on U87MG cells migrating (Hoechst staining of the nucleus).

From the tracking, either manual or automatized, the *x*-*y* coordinates and time-points of every trajectory were recorded (**Fig. 41**). In order to acquire data from a significant number of cells, images of adjacent areas of the PDMS substrates were acquired and then fused together with a custom-modified version of ImageJ's *Grid Stitching* plugin (https://imagej.net/plugins/grid-collection-stitching, see **Appendix**). The obtained stacks of tiles were then aligned with the plugin *Template Matching* (https://sites.google.com/site/qingzongtseng/template-matching-ij-plugin, see **Appendix**) and the tracking was then performed.

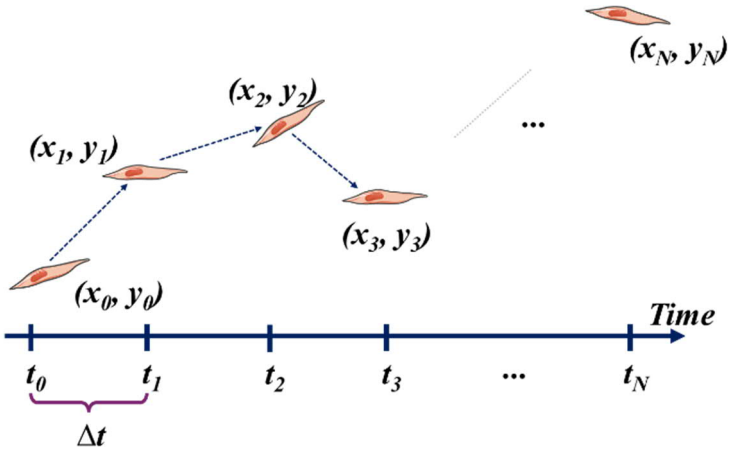

Fig. 41 Schematic representation of the rough data of a cell movement being tracked.

Cell migration is a rather complex process to characterize, hence a multitude of complementary parameters are hereby proposed, matching the same tendency currently followed in literature. Wind-rose plots are commonly used to show the unprocessed cell tracks, origin normalized. Another parameter, one of the most known and used, is the mean square displacement (MSD), as it can be interpreted as the area explored by cells over time. The MSD is defined as follows [78]:

$$MSD_{cell}(t = n\Delta t) = \sum_{i=0}^{N-n-1} \frac{(x_{i+n} - x_i)^2 + (y_{i+n} - y_i)^2}{N - n}$$

with *N* being the number of frames, *t* the time variable, *Δt* the time step between subsequent frames in the time-lapse sequence, and $n = t/\Delta t$ a parameter defined as "lag".

After determining each cell's MSD, a mediated value over the whole cell sample is calculated:

$$MSD_{all\ cells}(t = n\,\Delta t) = \sum_{j=1}^{N_{cells}} \frac{MSD_{cell,j}(t)}{N_{cells}}$$

In order to preserve data consistency only non-dividing cells that were migrating for at least 70% of the entire stack were considered.

From the tracks other parameters can be extracted, such as the traveled distance, the net displacement, the speed and the migration direction.

The mediated value of the MSD was then fitted with the Persistent Random Walk model (PRW) [79], [80]:

$$MSD_{PRW}(t) = 2S^2P[t - P(1 - e^{-t/P})]$$

From the *S* and *P* parameters found by the fitting, representing the speed and persistent time of the cell sample, the diffusion coefficient *D* is calculated as:

$$D = \frac{S^2 \cdot P}{2}$$

Such definition of the *D* coefficient simplifies the equation of the MSD_{PRW} to the version stated below:

$$MSD_{PRW}(t) = 4D[t - P(1 - e^{-t/P})]$$

To characterize the overall direction of migration, the final angle of migration, θ_{final}, was evaluated (**Fig. 42**). In particular, the absolute value of the sine of θ_{final} is compared to the mean value of the sine of a random distribution of angles, which results equal to $2/\pi$ and to other relevant directions depending on the type of experiment.

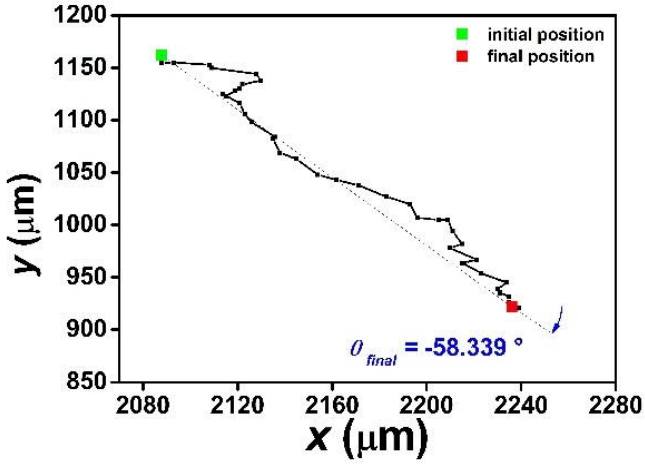

Fig. 42 Schematic representation of the tracking of a cell and its θ_{final} angle.

2.6.2 Evaluation of collective migration (Wound healing assays)

The time-lapse sequences of collective migration were analyzed with ImageJ: images were aligned with *Template Matching* and the border of the cell sheets were automatically detected by applying the *Variance Filter* (radius = 20), binarizing and launching *Analyze Particles*. From the detected ROIs the *x*-*y* coordinates of the borders as well as the area occupied by the cells were extracted and analyzed with a custom-made Python script.

In order to quantitatively characterize collective migration, the same parameters adopted in [65] were taken into consideration; below a brief description of each of them.

The area of the wound is obtained by subtracting the area occupied by the cells from the dimension of the entire image and it is expressed as the following percentage:

$$Wound\ area\ \%\ (t)\ =\ \frac{Area_{\ wound,t}}{Area_{\ wound,t=0}} \cdot 100$$

Initially, wound area at t = 0 is equal to 100% and, in time, it slowly narrows down as the gap is being gradually closed.

Wound repair is calculated as the recovered area at t = 24 h and it is given by the following equation:

$$\%\ of\ wound\ repair\ =\ 100 - Wound\ area\ \%\ (t\ =\ 24h)$$

From the *x*-*y* coordinates of the cell fronts, the advancement of the cell fronts is expressed as the Mean Front Displacement over time:

$$Mean\ Front\ Displacement\ (t) = \frac{\sum distance\ from\ initial\ border\ (t)}{N_{border\ points}} =$$

$$= \sum_{i=1}^{N_{border\ points}} \frac{\sqrt{(x(t,i) - x(t_0,i))^2 + (y(t,i) - y(t_0,i))^2}}{N_{border\ points}}$$

where $x(t, i)$, $y(t,i)$, $x(t_0, i)$ and $y(t_0,i)$ are the coordinates of the cell front at times t and t_0 respectively (**Fig. 43a**).

In addition to the previous parameter, from the *x*-*y* coordinates the front length *L* was calculated in order to express the complexity index given by the ratio *L/D* with *D* being the dimension of the image (**Fig. 43b**).

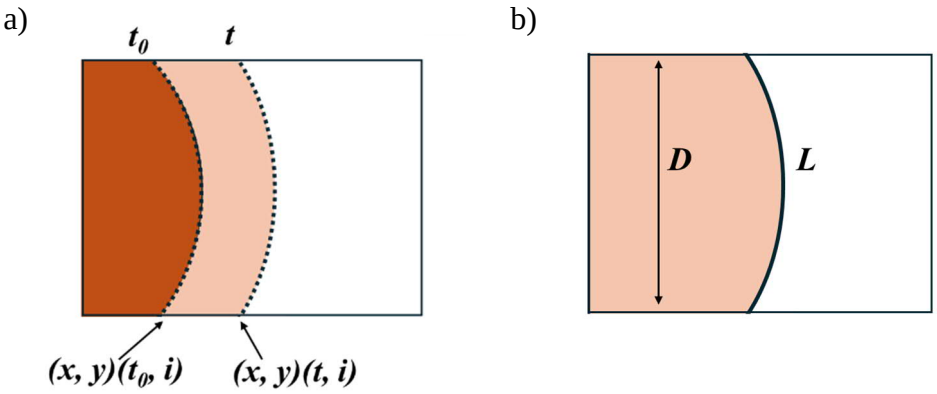

Fig. 43 (a) Schematic representation of the *x* and *y* coordinates from the cell front at different *t* values. (b) Schematic representation of the *L/D* ratio.

Finally, from the comparison of the images at $t = 0$ and $t = 24$ h the front speed and the angle of migration were extracted, and their frequency distribution was obtained.

2.6.3 Evaluation of cell orientation

Cell orientation data were extracted by contouring a large sample of cells at the end of each experiment using the *Freehand Selection Tool* in ImageJ and approximating each cell to an ellipsis. From this process, information about the *a* and *b* semi-axes of the ellipses was retrieved, as well as the major axis direction (**Fig. 44**).

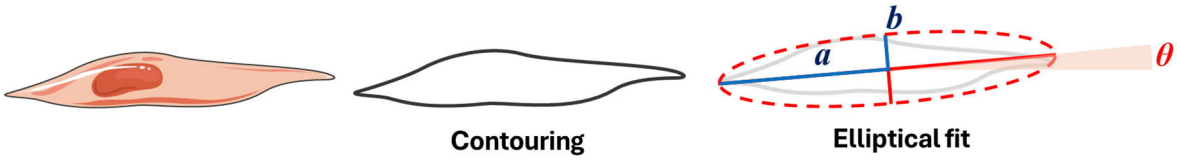

Fig. 44 Schematic representation of cell contouring and elliptical fitting.

Cell shape is described by the aspect ratio *b/a* parameter which assumes values close to 1 in the case of circularly shaped cells whereas it is < 1 for elliptical cells: the smaller the ratio the more elongated the ellipsis.

In addition to the aspect ratio, the orientation direction of the whole sample was expressed as the order parameter *S*, traditionally found in the field of liquid crystals and defined as such (for 3D systems):

$$S = \langle \frac{3\,cos^2(\Delta\theta) - 1}{2} \rangle$$

with $\Delta\theta = \bar{\theta} - \theta$.

In the case of 2D systems, *S* can be rewritten as:

$$S = \langle 2\,cos^2(\Delta\theta) - 1 \rangle$$

S can vary between −1 and +1 and can describe different symmetrical distributions:

- $S = 0$ represents a random distribution around the $\bar{\theta}$ direction
- $S = +1$ depicts perfectly ordered systems, either with parallel or anti-parallel orientation
- $S = -1$ describes a distribution orthogonally oriented against the $\bar{\theta}$ direction.

2.6.4 Semi-quantitative analysis of immunofluorescence signals

As markers for the focal adhesion complexes either Focal Adhesion Kinases (FAKs) or paxillin were stained, with their specific anti-FAK and anti-paxillin antibodies. To characterize stress fibers shape F-actin was stained with phalloidin and nuclei by DAPI.

To better characterize the effect of stretching upon stress fibers orientation and focal adhesions, a semi-quantitative analysis of the immunofluorescence signal was carried out as follows.

The red channel signal (F-actin) was processed on ImageJ by subtracting the background, then, cell bodies were contoured with the *Freehand Selection Tool* and saved as regions of interest (ROIs). For each ROI the fluorescence signal was processed through the *Fast Fourier Transform* (FFT) available in ImageJ which, very briefly, decomposes an image into the sum of the sine and cosine waves with different amplitudes and phases necessary to reconstruct the input image. The output of the FFT process on ImageJ is an image in the spatial frequency domain, which can uncover the contribution of periodic features and their orientation present in the starting image. In our case, aligned stress fibers generate, in the spatial frequency domain, bright streaks which are perpendicular to the fibers' orientation. An example of FFT processing of an image is given in **Fig. 45**.

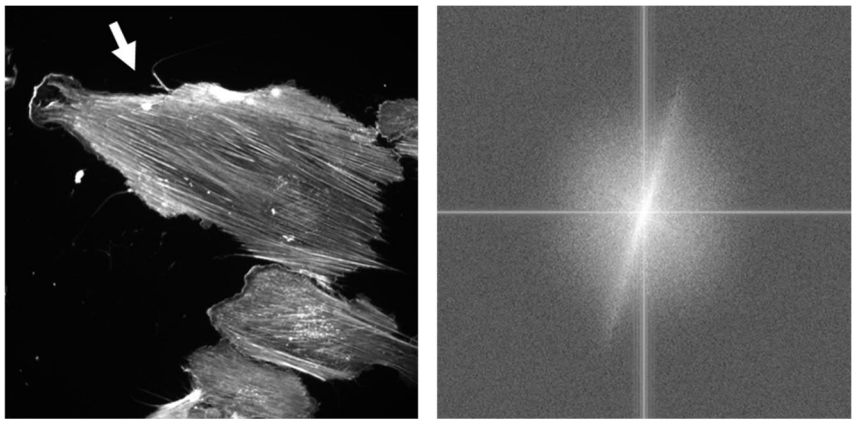

Fig. 45 Example of FFT process. On the left, the image of a cell with F-actin stained; on the right, the output of the FFT performed on the cell pointed by the white arrow.

This process allows to retrieve the direction of a sample of stress fibers and compare it to the orientation direction of the cell body (found by the procedure described in **Section 2.6.3** in **Chapter 2**) and to the direction of the cell nucleus (extrapolated by the binarization and the elliptical fit of the DAPI signal). The absolute value of the sine of these angular parameters was then compared for the different experimental conditions.

In addition to this analysis, the distribution of focal adhesions/paxillin within the cell body was also evaluated. The green channel signal (FAK, pPAX) was processed by ImageJ by subtracting the background, cell bodies ROIs from the previous analysis were retrieved and nuclei ROIs were detected by binarization of the DAPI signal. The mean gray value of the ROIs containing only the cell cytoplasm and only the (peri)nuclear area (**Fig. 46**) was calculated and then expressed as (peri)nuclear-to-cytoplasmic (N/C) ratio [81], defined as:

$$N/C = \frac{Mean\ gray\ value\ (Nuclear\ ROI)}{Mean\ gray\ value\ (Cytoplasmic\ ROI)}$$

Fig. 46 Schematic representation of cytoplasmic (on the left) and nuclear (on the right) ROIs.

2.6.5 Quantification of gene expression levels in HCF cell (qRT-PCR)

To assess how gene expression is influenced by the stretching protocols, qRT-PCR measurements were carried out after large samples of cultured and stretched cells were collected, with the aid of a larger version of the uniaxial stretcher (**Fig. 47**) that enables to simultaneously stimulate up to four PDMS substrates. These measurements were performed at the INBB – Biostructures and Biosystems National Institute in Bologna.

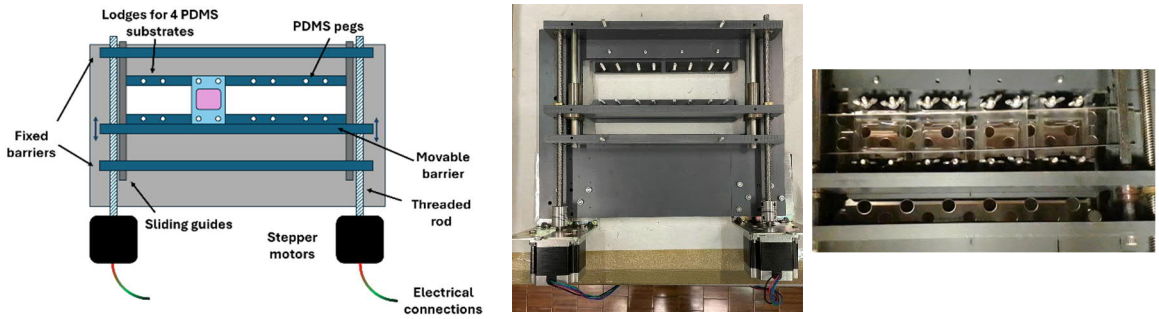

Fig. 47 Schematic representation and pictures of the multi-substrate uniaxial stretcher.

The culture medium was discarded, and cells were washed with PBS 1x, and the mRNA contained in the cells was extracted using the Aurum™ Total RNA Mini Kit (BioRad #7326820). The concentration of the obtained RNA solution was evaluated by spectrophotometry, using the NanoDrop One photometer (Thermo Fisher). After that, 400 ng of RNA were used to obtain, by reverse transcription, the corresponding complementary DNA (cDNA), using the iScript Advanced cDNA Synthesis Kit for RT-qPCR (Bio Rad), applying a two-step cycle in a thermocycler (step 1: 20 min at 46 °C, step 2: 1 min at 95 °C). The obtained cDNA solution was then diluted to 5 ng/µL and used to perform qRT-PCR.

The amplification and quantification of the cDNA was carried out in a thermocycler (CFX Connect – BioRad) adding to 1 µL of cDNA solution 10 µL of the iTaq Universal SYBR Green Supermix 2X (BioRad), 1 µL of a 5 µM mix of Forward and Reverse gene-specific primers (BioRad) and 8 µL of nuclease-free water. The obtained 20 µL of solution were then subjected to amplification and quantification as follows:

- 1 cycle at 95 °C for 30 seconds
- 40 cycles consisting in two steps:
    - 5 seconds at 95 °C (denaturation)
    - 30 seconds at 60 °C (annealing and extension)
- 1 final cycle with a thermal ramp from 65 °C to 95 °C (DNA melting)

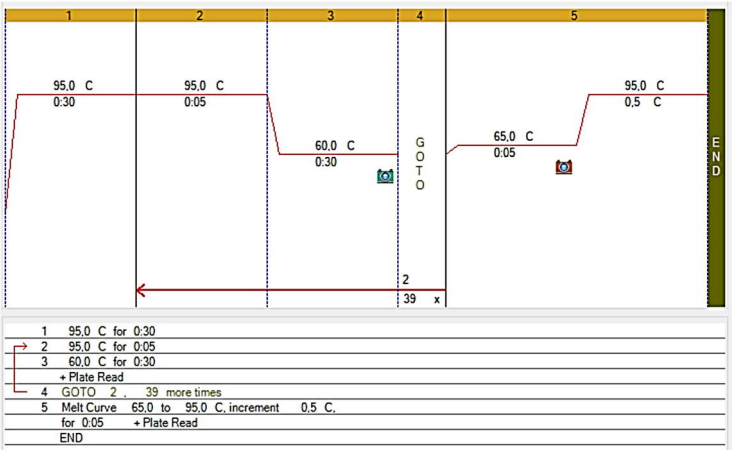

Fig. 48 Thermal profile of the thermocycler.

To study the manifold effects that stretching could provide to the cells, a large number of genes were chosen, some of them related to the production of collagen and fibronectin (COL1A1, COL1A2, COL3A1, FN1, BMP1), others involved – either directly or indirectly – with the degradation of the ECM (MMP2, TNC, TIMP1, TIMP2, SPARC) and others involved in mechanotransduction (KCNK1 (alias TWIK1), KCNK2 (alias TREK1)), TRPV4 and TMEM63A). As reference housekeeping genes, GAPDH, PGK1 and YWHAZ were chosen using the Prime PCR Pathway Plate Reference Gene 96well (BioRad).

The Livak method was applied to calculate the $\Delta\Delta Ct$ value of each gene of interest. Briefly, the ΔCt of a specific target gene is given by its Ct value (cycle threshold, meaning the cycle number in which the fluorescence signal of the target gene is significantly detectable)

minus the *Ct* value of a reference gene. The *ΔCt* value for a gene is both evaluated in the sample of interest and in a control sample, as follows:

$$\Delta Ct_{\,sample} = Ct_{\,(target\ gene,\ in\ sample)} - Ct_{\,(refence\ gene,\ in\ sample)}$$

$$\Delta Ct_{\,control} = Ct_{\,(target\ gene,\ in\ control)} - Ct_{\,(refence\ gene,\ in\ control)}$$

$$\Delta\Delta Ct = \Delta Ct_{\,sample} - \Delta Ct_{\,control}$$

In order to compute the fold change, or Relative Normalized Expression, the $2^{-\Delta\Delta Ct}$ value is then calculated.

2.6.6 Statistical evaluation of the data

The data presented in this work are expressed as mean value ± standard deviation, if not otherwise expressed. To assess statistical difference, the unpaired t-test was performed comparing two sets of data (typically the control sample *versus* the treated/stretched sample). Values of *p* below 0.05 were considered statistically significant.

Chapter 3 – Results of calibration of the stretcher devices

In this Chapter the results of the experimental calibration and validation by FEM simulation are presented for the uniaxial, biaxial and isotropic stretchers respectively in **Sections 3.1**, **3.2** and **3.3**.

3.1 Uniaxial stretcher

The calibration of uniaxial stretcher device here presented is intended to complete what formerly published by Ragazzini et al. [39], enriching the adopted procedure and the results previously achieved with validation by FEM simulations.

Fig. 49 is an example of displacement maps which portray how the PDMS is being deformed by the uniaxial stretcher. These maps were obtained from a slightly modified version of the Particle Image Velocimetry plugin for ImageJ (https://sites.google.com/site/qingzongtseng/piv) (see the entry *"Multi-slice PIV plugin"* attached to the **Appendix** of this thesis).

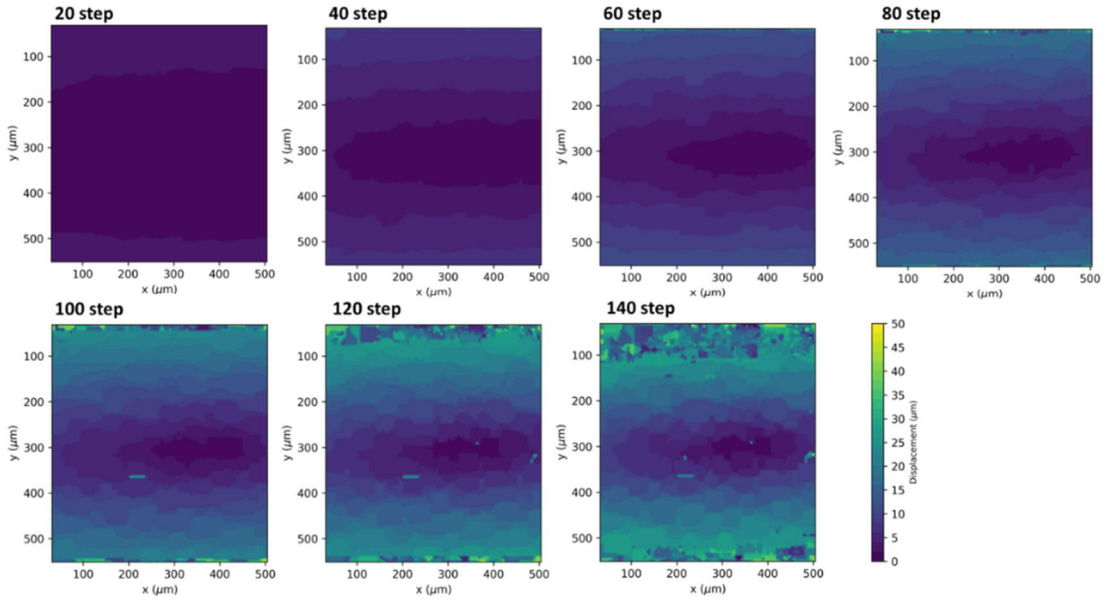

Fig. 49 Displacement maps obtained from the PIV analysis performed comparing images at increasing steps *versus* the initial one.

The ε_{xx} and ε_{yy} components of the strain and its final value ε are displayed in **Fig. 50**. The *x* and *y* components increase in magnitude as the steps applied by the stepper motors are increased: in particular, the *y* component has a positive sign in accordance with an elongation of the PDMS substrate along the *y* axis, while the *x* component has a negative sign, in agreement with a compression of the substrate. The final ε value obtained by the sum of the ε_{xx} and ε_{yy} components results in a linear dependence to the applied steps, with an experimentally relevant value of strain obtained at 100 steps, $\varepsilon = (8.6 \pm 0.8)$ %.

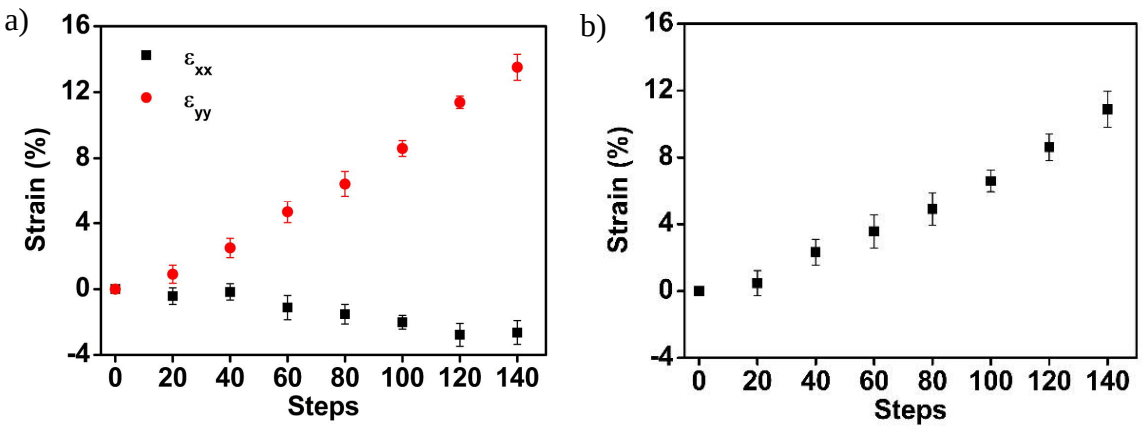

Fig. 50 ε_{xx} and ε_{yy} (a) and ε value (b) at progressively increased steps during the uniaxial stretcher calibration.

The two mirroring zero strain directions, θ_1 and θ_2 (**Fig. 51**) show little dependence on the applied steps. At higher steps of deformation, θ_1 and θ_2 reach constant values which are reported to be $\theta_1 = (25 \pm 2)$ ° and $\theta_2 = (155 \pm 1)$ °.

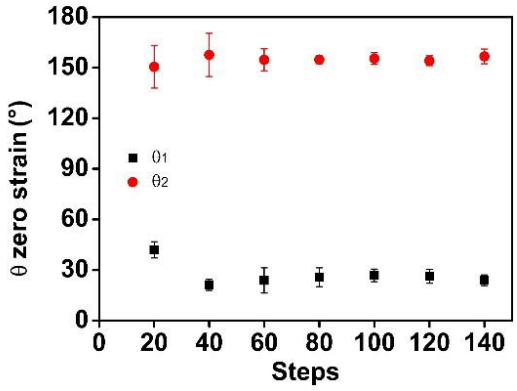

Fig. 51 Progression of the two mirroring directions of zero strain during the uniaxial stretcher calibration.

The FEM simulations were performed applying a 2.0 mm deformation along the longitudinal axis (which will from now on be referred to as the *y* axis, to be uniform with the notation adopted for the previous paragraph) at the top and bottom sides of the substrate portrayed in **Fig. 52**. The applied deformation of 2.0 mm per side was chosen to be consistent with the effective deformation obtained at 100 steps by the stepper motors (0.02 mm/step · 100 steps).

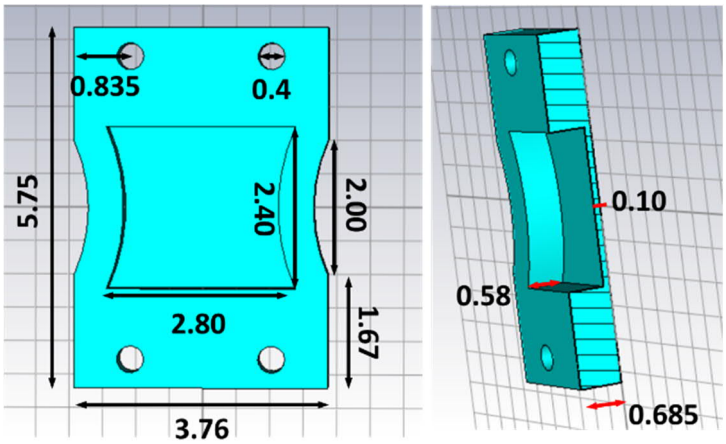

Fig. 52. FreeCad design of the PDMS substrate for the uniaxial stretcher, measurements are given in centimeters.

The output of the simulation reported in **Fig. 53** shows the distribution of ε_{xx}, ε_{yy}, ε and the zero- strain direction (one of the two mirroring angles). The values of ε and $\theta_{zero\text{-}strain}$ reach a constant value in the center of the substrate: this aspect underlines the fact that the substrate geometry, slightly curved at the sides, provides a uniform distribution of the mechanical properties in the center, which is the area usually observed during stretching experiments.

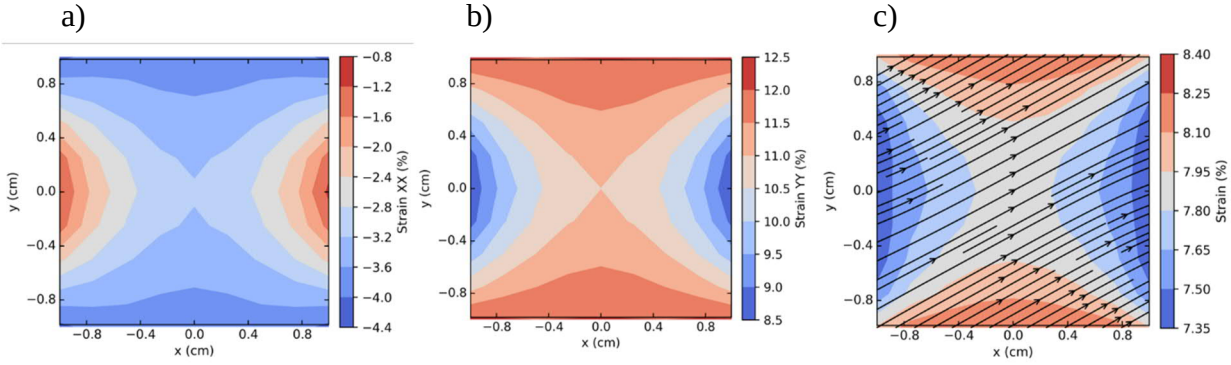

Fig. 53 Distribution of the values of ε_{xx} (a), ε_{yy} (b) and ε overlaid with the zero-strain direction (c), depicted by the black arrows.

From the FEM simulations the mean values of ε and θ in the center of the well, in a (0.1 x 0.1) cm^2 area comparable to the experimentally observed one are, respectively, (7.84 ± 0.02) % and (28.20 ± 0.02) °. Both values are in good agreement with the experimental ones.

3.2 Biaxial stretcher

The calibration of the biaxial stretcher device followed two different operational modes: in the first case, either the *x* or the *y* motor axis was individually stretched; in the second case they both were used simultaneously. This choice was made for two reasons: first, to check that the two axes of the stepper motors were, *de facto*, equally effective at stretching and, second, that stretching with both axes could provide an equibiaxial deformation. For the sake of brevity, from now on, we will refer to the first operating mode as *single-axis* mode and to the second as *two-axes* mode.

Fig. 54 compares the ε_{xx} and ε_{yy} components and the ε values obtained during the single-axis calibration of the *x* and *y* axes, in panels (a) and (b) respectively. Comparing the calibration of the *x* axis *versus* the *y* axis we can notice a strong resemblance between the data, proving that the two axes are interchangeable and can provide strain to the PDMS substrate to the same extent. At 100 steps, both axes provide in fact strain values of ε = (10 ± 1) %. The same behavior due to elongation and compression occurring to the PDMS substrate observed for the uniaxial stretcher is once again observed, as expected. Even the mirroring directions of zero strain are very similar, as written in **Table 3**; moreover, the values of ε and θ are in close accordance with those obtained for the uniaxial stretcher, proving that the biaxial stretcher can work, when used in single-axis mode, as a uniaxial device.

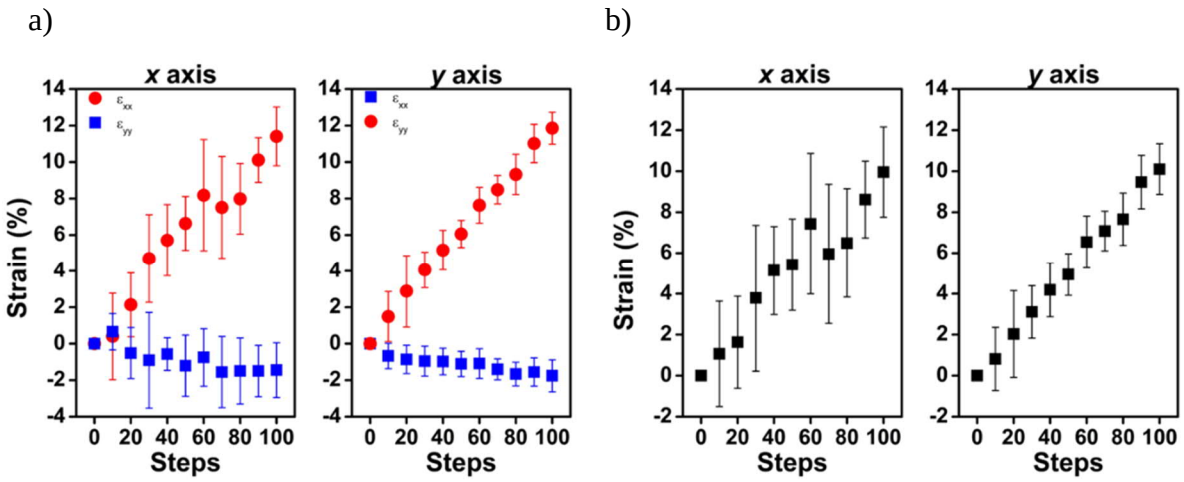

Fig. 54 Values of ε_{xx} and ε_{yy} (a) and ε (b) in the single-axis mode calibration of the *x* and *y* axes of the biaxial stretcher.

Table 3 Mirroring angles of zero strain in the single-axis calibration mode of the biaxial stretcher.

Single-axis calibration	θ_1 (°) [*]	θ_2 (°) [*]
x axis	17 ± 11	158 ± 10
y axis	19 ± 6	158 ± 4

[*] values are referred with respect to the direction of compression.

The results obtained by the two-axes calibration, performed by feeding the same number of steps to both axes of the stretcher device, are expressed as radial strain ε and reported in **Fig. 56**. The radial strain was calculated as $\varepsilon = (L - L_0) \cdot 100 / L_0$, with L being the distance of a bead from the center of the image (a fixed point) at different steps and L_0 its initial distance, as exemplified in **Fig. 55b**.

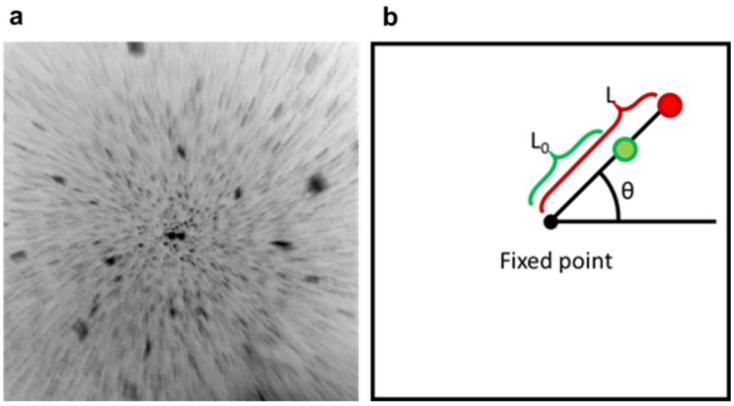

Fig. 55 *z*-projection of the beads being displaced during the two-axes calibration procedure (a) and schematic representation of the choice of L and L_0 (b).

The results in **Fig. 56a** show a homogeneous distribution of the radial strain ε, independently from the angle at which the beads were chosen with respect to the fixed central point. This evidence proves that the x and y axes of the biaxial stretcher can provide an isotropic dilation of the PDMS substrate in all directions. The different values were mediated and are displayed in **Fig. 56b**, where a linear increment with respect to the steps of the stepper motors is noticeable. In particular, at 100 steps the value of radial strain is ε = (8.9 ± 0.9) % while no value of zero-strain direction is hereby provided, since ε is actually non null and almost constant in every direction.

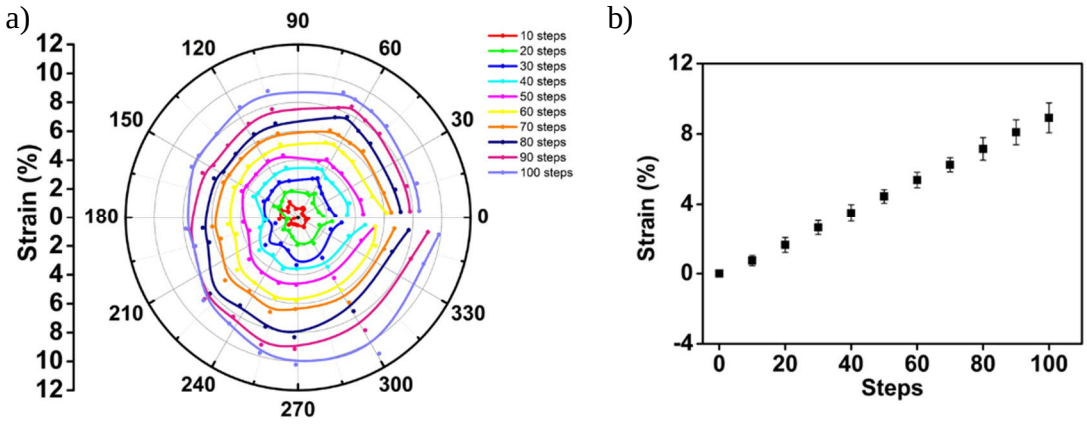

Fig. 56 Values of radial ε in the two-axes calibration mode (a) and progression of the mean values of radial ε versus the steps (b) during the biaxial stretcher two-axes calibration.

The FEM simulations were performed using the design in **Fig. 57** following the same modes adopted for the experimental procedure. For the simulations the substrate was either pulled from two opposite sides (single-axis mode) or by the four of them (two-axes mode). The previously used amount of applied deformation, 2.0 mm per side, was again applied.

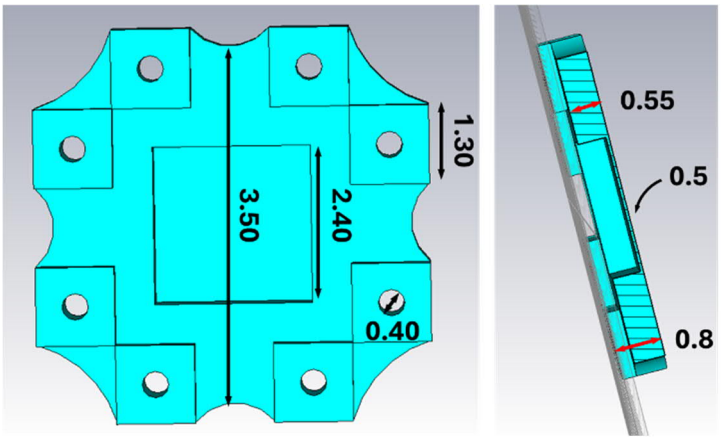

Fig. 57 FreeCad design of the PDMS substrate for the biaxial stretcher, measurements are given in centimeters.

Results from the simulation in single-axis mode in which the *y* axis was deformed (**Fig. 58**) show, as expected, a small compression along the *x* axis and an elongation along the *y* axis. In **Fig. 58c** the final ε value overlaid with the θ value of zero strain is shown, where a large central area characterized by homogeneous values of both properties is easily noticeable. The values of ε and θ mediated over the center of the well are, respectively, (8.35 ± 0.04) % and (25.0 ± 0.2) °.

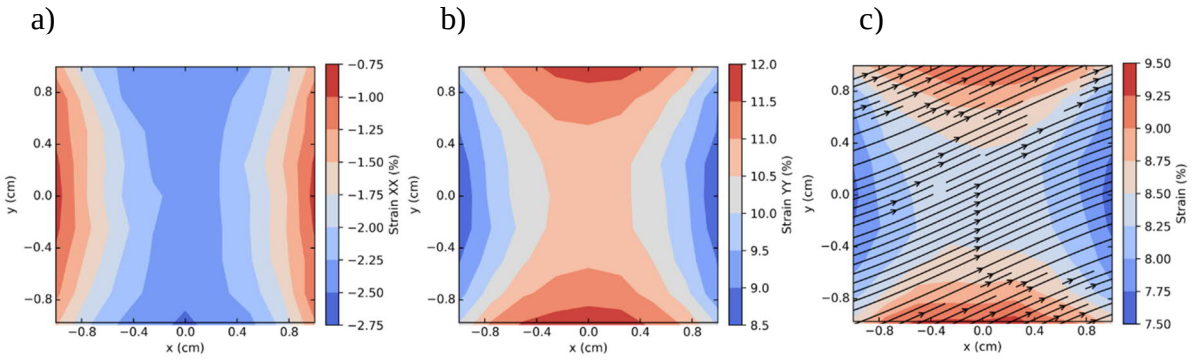

Fig. 58 Distribution of the values of ε_{xx} (a), ε_{yy} (b) and ε overlaid with the zero-strain direction (c), depicted by the black arrows. The maps hereby reported result from the single-axis mode simulation in which the *y* axis only was deformed.

The two-axes mode simulation returns the distribution maps that are illustrated in **Fig. 59**. Since the simulation is carried out in a *x*-*y* reference system, the results in panel **Fig. 59c** need to be corrected by a ½ factor, to be comparable.

$$\varepsilon_{radial} = \frac{L - L_0}{L_0} \cdot 100$$

$$\varepsilon_{area} = \frac{\Delta A}{A_0} = \frac{(A - A_0)}{A_0} \cdot 100 = \frac{(x + \Delta x) \cdot (y + \Delta y) - xy}{xy} \cdot 100$$

For very small deformations of *x* and y the formula becomes:

$$\varepsilon_{area} = \frac{(x + \delta x) \cdot (y + \delta y) - xy}{xy} \cdot 100$$

$$\varepsilon_{area} = \frac{xy + x \cdot \delta y + y \cdot \delta x + \delta x \cdot \delta y - xy}{xy} \cdot 100$$

$$\varepsilon_{area} = \left(\frac{\delta x}{x} + \frac{\delta y}{y}\right) \cdot 100 = \varepsilon_{xx} + \varepsilon_{yy}$$

In an isotropic deformation ε_{xx} and ε_{yy} are expected to be equal, which results in:

$$\varepsilon_{area} \sim 2 \cdot \varepsilon_{xx}$$

Taken into account the previous correction, the value of ε mediated in the central (0.1 x 0.1) cm^2 area given from **Fig. 59c**, (16.68 ± 0.07) %, is understandably almost two-fold the radial ε experimentally found (8.9 ± 0.9) %. The symmetry of the ε distribution reflects the application of a deformation from four orthogonal sources.

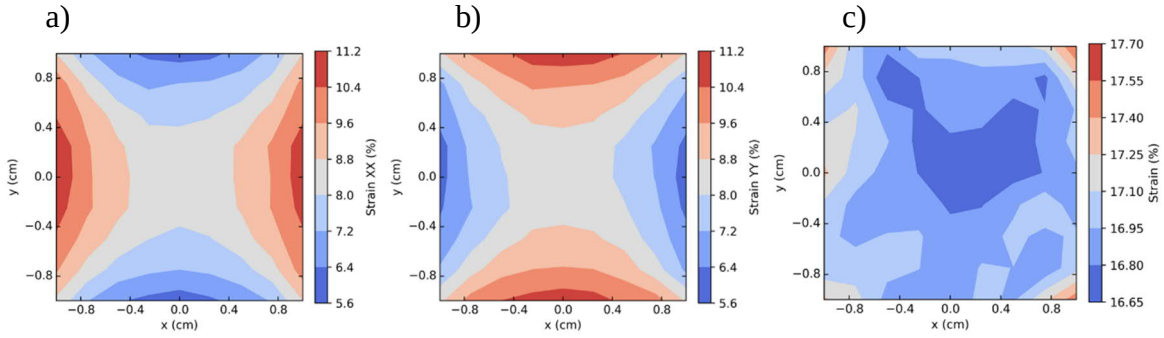

Fig. 59 Distribution of the values of ε_{xx} (a), ε_{yy} (b) and ε resulting (c) from the two-axes mode simulation.

3.3 Isotropic stretcher

The calibration of isotropic stretcher device recalls the two-axes mode adopted for the biaxial stretcher. In **Fig. 60** the results of the calibration are presented: in panel (a), the progression of the radial strain angle-wise shows a homogeneous distribution in the PDMS while panel (b) collects the mean value of ε while increasing the steps of the only stepper motor of the device. Data show a sort of initial "induction" since no appreciable bead displacement was detected until 30 steps were reached. Once surpassed 80 steps the PDMS substrate was visibly very stretched, almost reaching the breaking point, so that the experimental calibration was interrupted. The 80-steps condition was chosen as the experimentally relevant one, with a $\varepsilon = (8.3 \pm 0.3)$ %. Given the isotropy of the deformation, no $\theta_{zero\text{-}strain}$ was calculated.

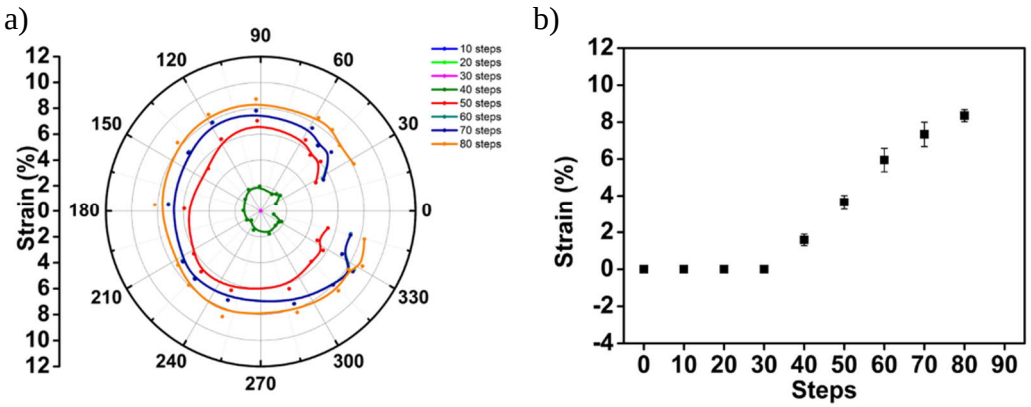

Fig. 60 Values of radial ε (a) and progression of the mean values of radial ε (b) versus the steps.

The FEM simulation was carried out applying a 2.0 mm displacement at the six poles of the design depicted in **Fig. 61**. At 80 steps, the radial deformation of the PDMS resulted to be 2.0 mm per side – which in other stretchers was achieved only at 100 steps – because of an intrinsic difference in the construction of the isotropic stretcher which makes it more efficient at pulling.

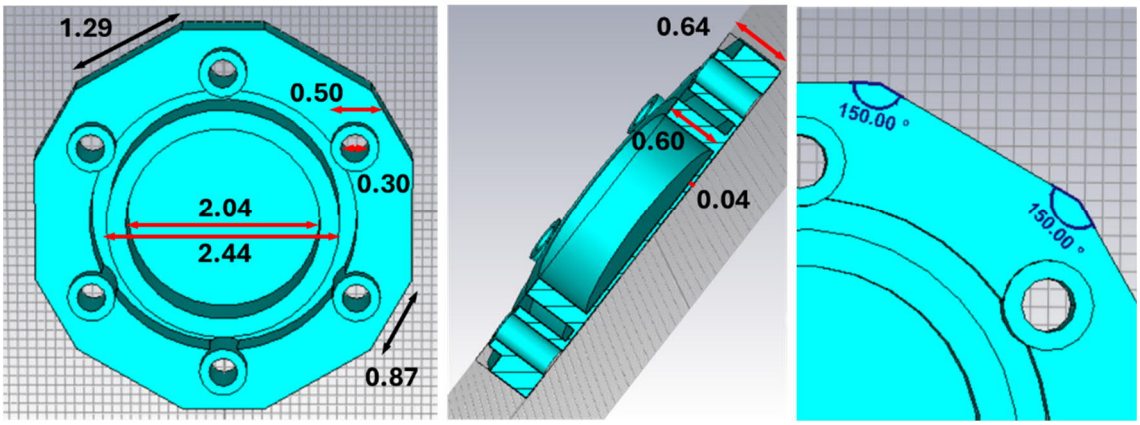

Fig. 61 FreeCad design of the PDMS substrate for the isotropic stretcher, measurements are given in centimeters.

The results obtained from the simulation show a very uniform strain distribution, **Fig. 62**, especially if we look at the final ε value (**Fig. 62c**), rather than its components ε_{xx} and ε_{yy} (panels (**a**) and (**b**)). The ε value mediated in the center of the well – in this case in a circular region of area $\pi \cdot (0.1)^2$ cm^2 – turned out to be (16.52 ± 0.03) % roughly two-fold the experimental radial value (see correction factor introduced in **Section 3.2**).

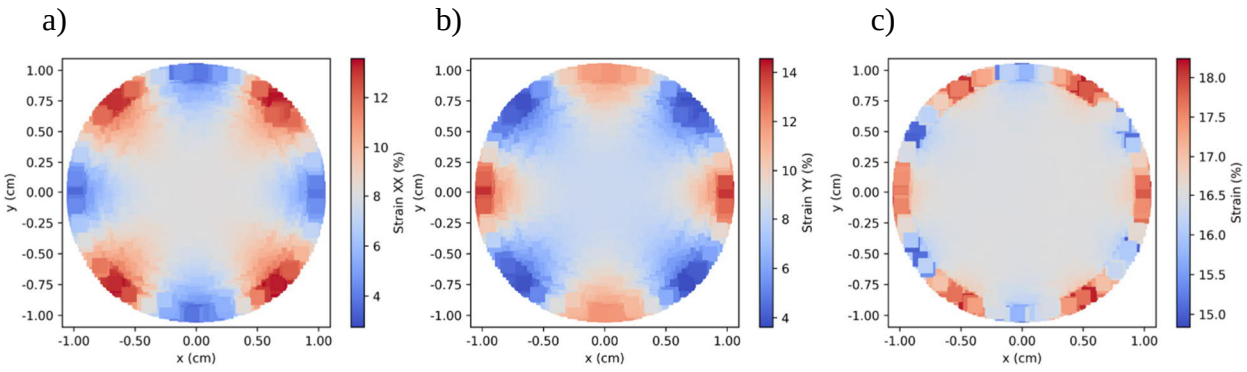

Fig. 62 Distribution of the values of ε_{xx} (a) ε_{yy} (b) and ε (c).

The results obtained from this series of calibration and validation simulations were then used to deform to certain extents the PDMS substrates during time-lapse experiments.

Chapter 4 – Results of HCF stretching experiments

In this Chapter the results obtained from cyclic stretching experiments of HCF cells are presented. In particular, in **Section 4.1** we will focus on uniaxial stretching experiments, diving into the effects of different signals with 1 Hz frequency on cells behavior. In addition to this, a brief comparison with a low-frequency signal (0.3 Hz) and an extensive analysis of the peculiarities of each stimulus are also illustrated.

In **Section 4.2** the outcomes of biaxial stretching experiments with the triangular signal at 1 and 0.3 Hz are displayed. These experiments exploit the biaxial stretcher to impose a 90°-inversion in the direction of deformation. Cell adaptation after 30 min and 1 h from the inversion point is evaluated.

For clarity reasons, the different stretching protocols will be henceforth simplified as *T* = triangular, *Q* = square, *S* = sine and *CTRL* = control conditions.

4.1 Uniaxial stretcher experiments

4.1.1 T, Q and S signals with f = 1 Hz

Orientation

Cyclic stretching quickly causes an active re-orientation of HCF cells, which starts assuming an alignment that is almost perpendicular to the direction along which the stretching stimulus is applied (**Fig. 63**).

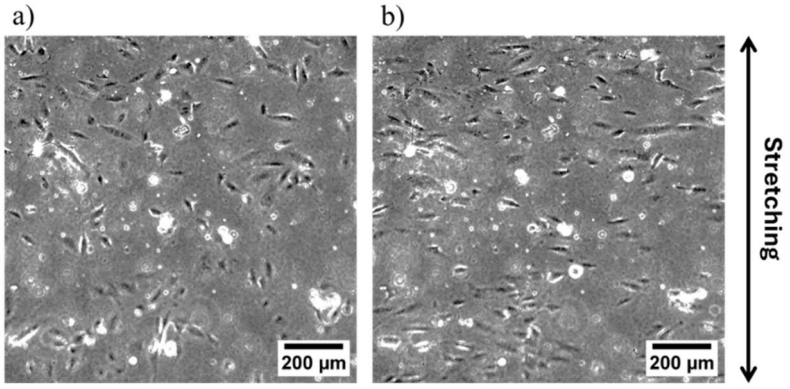

Fig. 63 Optical microscope images of HCF cells before (a) and after (b) a 3h-long stretching session with the T signal (*f* = 1 Hz).

The distribution of the final orientation reached by cells exposed to T, Q and S signals with f = 1 Hz is shown in **Fig. 64**. The distribution of the angle in control conditions is, as expected, uniformly spread in the 0 – 180 ° range, since in absence of a directional cyclic stretching cue cells orient in a random way. The application of different stretching stimuli induces cells to orient along preferential directions and, in fact, the appearance of two broad mirroring peaks in the distribution plot for the T, Q and S waves can be noticed. The position of these peaks was retrieved by fitting the plots with a Gaussian model and their position, indicated as the angles α and β, is given in **Table 4**.

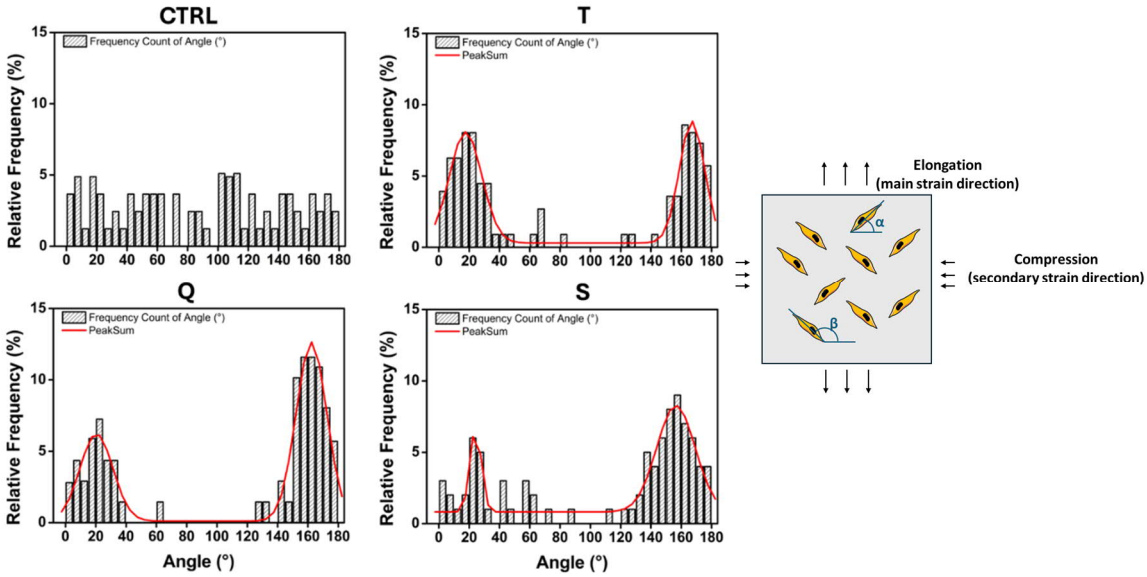

Fig. 64 Frequency distribution histograms of the orientation angles (N = 100). The red line depicts the Gaussian fitting.

Table 4 Values of orientation angles evaluated after 3 h of experiment for the different tested conditions.

Orientation angles	T	Q	S
α (°)	18 ± 1	20 ± 2	24.3 ± 0.8
β (°)	167.1 ± 0.8	162.4 ± 0.7	156 ± 1

The values of α and β are roughly in line with the zero-strain directions previously found from the experimental calibration of the uniaxial stretcher (θ_1 = (25 ± 2) ° and θ_2 = (155 ± 1) °). In particular, the sinusoidal signal results best match the α and β value to the expected ones.

To evaluate the degree of order in the orientation reached by the cells after 3 h of stimulation, the *S* parameter was calculated for every condition (**Fig. 65a**). As expected, in control conditions with no applied stimulus the orientation of the cells is randomly distributed, hence a low value of *S*, which amounts to (0.6 ± 0.3). When cyclic stretching stimuli are applied *S* increases, indicating the achievement of an ordered configuration with a value closer to +1. The tested signals provide a very similar *S* value: (0.9 ± 0.2) for the Q and S waves, (0.9 ± 0.3) for the T wave.

Concerning cell shape after 3 h, stretching results in a very subtle enhancement in the elliptical shape of the cells (see **Fig. 65b**). From a value of (0.5 ± 0.2) for the control cells, *b/a* is slightly lowered to (0.4 ± 0.2). The shape factor *b/a* remains roughly close to 0.5, describing an elliptical shape with the semi-minor axis (*b*) roughly half the major one (*a*). Even though the shape factor is not significantly changed, the fact that cells retain their fibroblast-like elongated shape could be interpreted as an index of good preservation of the cell morphology and, in general, cell health and phenotype. In fact, if the aspect ratios massively spiked to 1, the appearance of circular shaped cells could be regarded as the beginning of loss of adhesion to the substrate. Bearing this consideration in mind, we can infer that the applied stimuli are not harmful or too harsh for the cells.

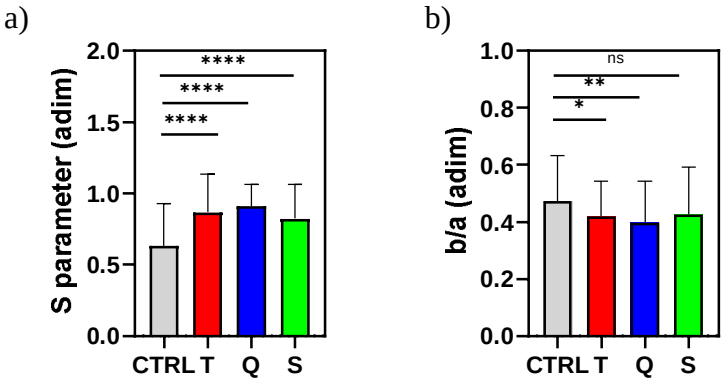

Fig. 65 Histograms of the *S* parameter (a) and shape factor *b/a* (b) (N = 100).

Single-cell migration

Regarding cell migration during the experiments, **Fig. 66** depicts the origin-normalized trajectories of the analyzed cells. In control conditions the trajectories are uniformly distributed and quite spread, while trajectories during the application of the T and S signals appear as rather "compressed" and more horizontally tilted, in addition to being slightly shorter. The trajectories observed for the Q signal are the most affected ones: the "rose" plot appears as quite shrunk, apart from some unexpectedly long paths.

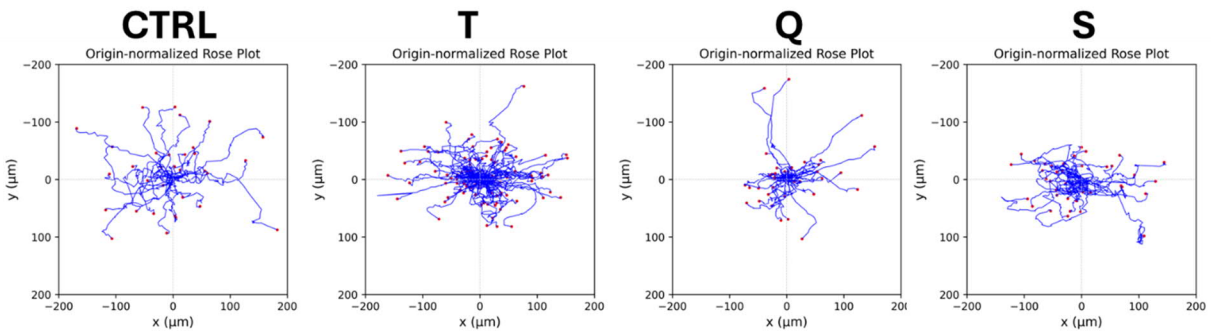

Fig. 66 Origin-normalized plots with cell trajectories. The red dots represent the final position reached after 3 h of experiment.

Fig. 67a reports the total distance traveled by the cells in each experimental condition, obtained by summing all the *i*-th steps swept along each cell's trajectory. In control conditions cells exhibit the ability to migrate for a mean value of traveled distance equal to (160 ± 61) μm. For the T signal, the distance is slightly reduced to (126 ± 46) μm which corresponds to a loss of about 21%, if compared to the CTRL condition. The Q signal sees the traveled distance further diminished (−32%), resulting in a value of (109 ± 46) μm. Unlike previous stimuli, the S signal preserves the same migration capability, ensuring a (156 ± 60) μm of traveled distance to the cells (which corresponds to a non-significant loss of 2%).

The mean speed of the analyzed samples is shown in **Fig. 67b**. In control conditions, cells exhibit a mean speed of (0.9 ± 0.3) μm/min which is completely preserved in the case of the S signal (0.9 ± 0.3) μm/min. For the T and Q signals, the mean speed value amounts to (0.7 ± 0.2) and (0.6 ± 0.3) μm/min, respectively. These speed moduli are in line with what is reported in literature, especially for mesenchymal migration.

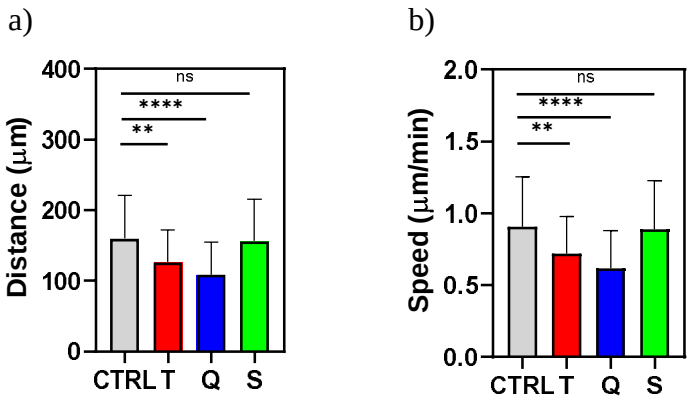

Fig. 67 Total traveled distance (a) and mean speed (b) (N = 50).

The radar plots in **Fig. 68** present the frequency distribution of the θ_{final} values, projected in the 0 – 180 ° range. In CTRL conditions the overall distribution is uniform, with no particular highlighted direction; applying either the T, Q or S signal the angular distribution favors angles close to the $\theta_{zero\text{-}strain}$ values of the uniaxial stretcher. This aspect is clearer in **Fig. 69**, where the mean value of $|sin(\theta_{final})|$ is computed. In control conditions the mean value of this quantity amounts to (0.65 ± 0.05), whereas it slightly decreases for the T (0.53 ± 0.04), Q (0.54 ± 0.05) and S signals (0.51 ± 0.05). The higher value obtained for the CTRL is close to the theoretical value for a uniform distribution (i.e. $2/\pi \sim 0.64$) while for the stretched conditions values are close to $|sin(\theta_{zero\text{-}strain})| \sim 0.42$.

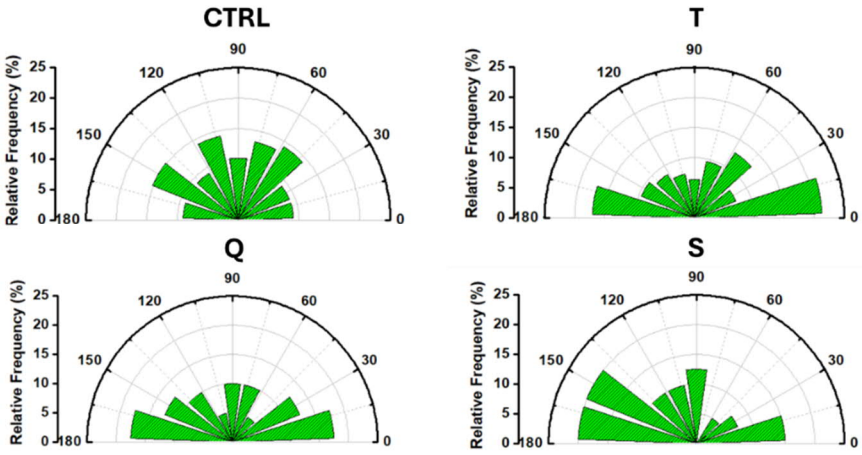

Fig. 68 Radar plots of θ_{final} (N = 50).

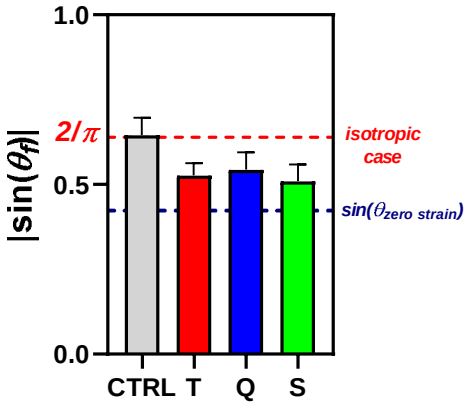

Fig. 69 Value of $|sin(\theta_{final})|$ (N = 50).

In **Fig. 70** the mean square displacement (MSD) for each experimental condition is plotted. Comparing the different curves of the stretched conditions to the CTRL one, a significant decrement of the steepness of the MSD(t) function is noticeable. To quantify the loss in the explored area over time with respect to the performance obtained in control conditions, a percentage loss was calculated as follows:

$$Loss\,\% = \frac{MSD^*(2h) - MSD(2h)}{MSD^*(2h)} \cdot 100$$

with $MSD^*(2h)$ being the final value reached in CTRL conditions.

The percentage loss for the T and S signals amounts to, respectively, 39% and 35%: these values confirm that the two protocols are, in fact, effectively similar, with the sinusoidal wave having the smallest impact on cell motility. The harsher stimulus, the Q signal, results in lower the final MSD value (at t = 2 h) by 51%, compared to the value reached in control conditions.

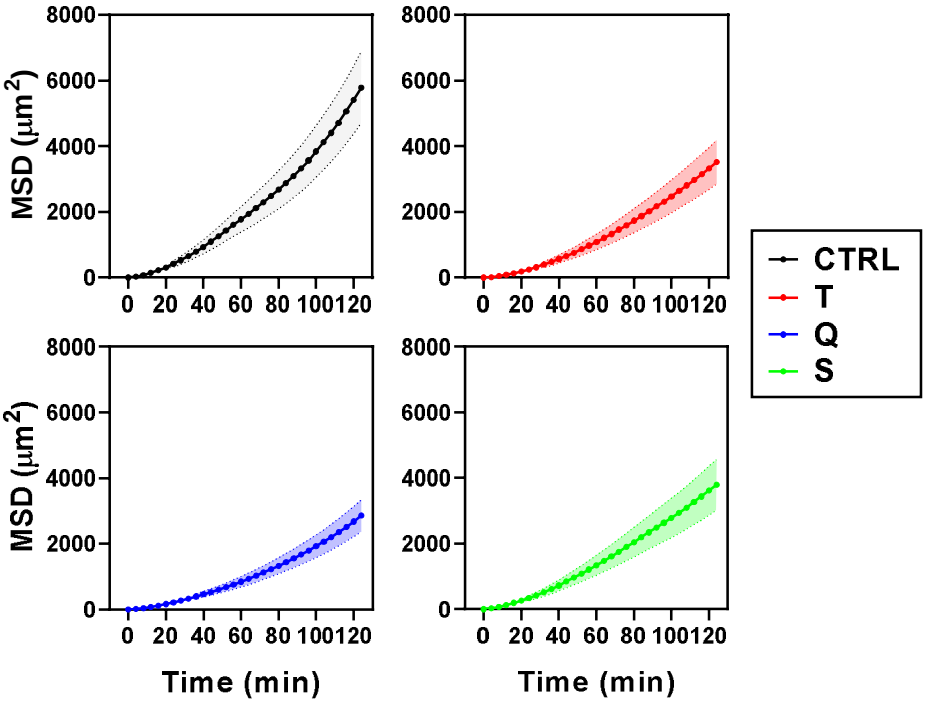

Fig. 70 Mean Square Displacement over time (N = 50).

The coefficient of diffusion *D*, as obtained from the PRW fitting, is shown in **Fig. 71**. The *D* values confirm the qualitative observations about the decaying trend found in the MSD plot (CTRL > T > Q ~ S). In particular, the resulting *D* values amount to be, (19.9 ± 0.5) μm^2/min for the CTRL conditions, (12.7 ± 0.8) μm^2/min for the T signal and, for the Q and S signals, respectively (10 ± 1) and (9.8 ± 0.6) μm^2/min.

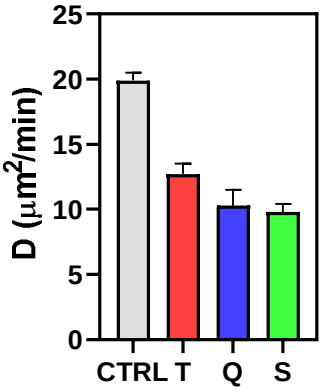

Fig. 71 Coefficient of diffusion *D* (N = 3).

Immunofluorescence

After 3 h of experiment, either with or without cyclic stretching, some cell samples were fixed with PFA 4% in PBS and stained for immunofluorescence. To better evaluate the effects of stretching on the cytoskeleton, the F-actin in stress fibers (SFs) and Focal Adhesion Kinases (FAKs) were the targets of the staining process, in addition to nuclei (with DAPI).

In **Fig. 72**, a set of images acquired in control conditions is displayed. The pictures provide an insight into the inner organization of the cytoskeleton in CTRL conditions. The F-actin signal (**Fig. 72b**) is quite evenly spread over the cell body, with hints of fibrillar structures with no specific alignment. The FAK signal (**Fig. 72c**) shows a peripheral concentration of intense spots, corresponding to focal adhesions on the borders of the cell body, as one would expect. Right below the cell nucleus different spots of FAKs, due to ventral focal adhesions supporting the cell body, are noticeable.

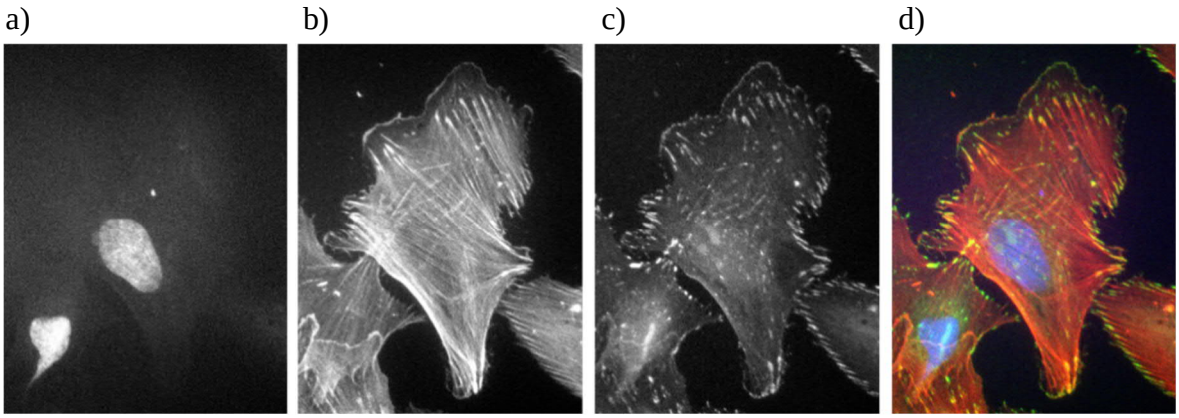

Fig. 72 Fluorescence images of HCF cells in control conditions, acquired with the 60x immersion-oil objective. Panels: a) DAPI, b) F-actin, c) FAK, d) composite.

Fig. 73 and **Fig. 74** are relative to cells stretched, respectively, with the T and the Q signal. In both cases, an enhancement in stress fibers definition and orientation is observed, as well as a qualitative elongation, which can be ascribed to the effect of the stretching stimulus. Concerning focal adhesions, even though perimetral spots are conserved, an increment in peri-nuclear signal is observed too. Furthermore, the orientation and shape of the perimetral spots of FAKs is apparently consistent with the SFs.

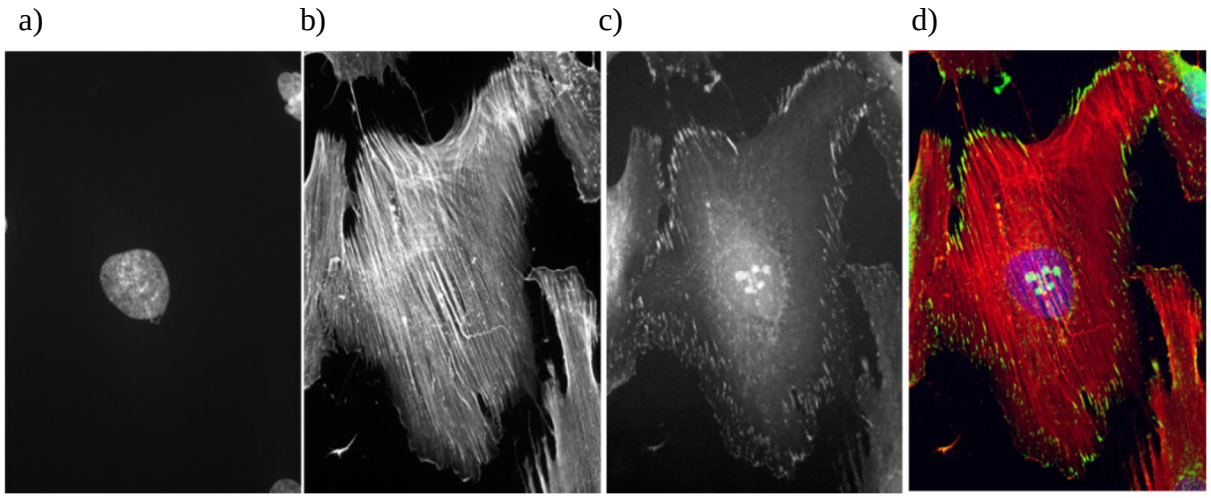

Fig. 73 Fluorescence images of HCF cells stretched with the T signal, acquired with the 60x immersion-oil objective. Panels: a) DAPI, b) F-actin, c) FAK, d) composite.

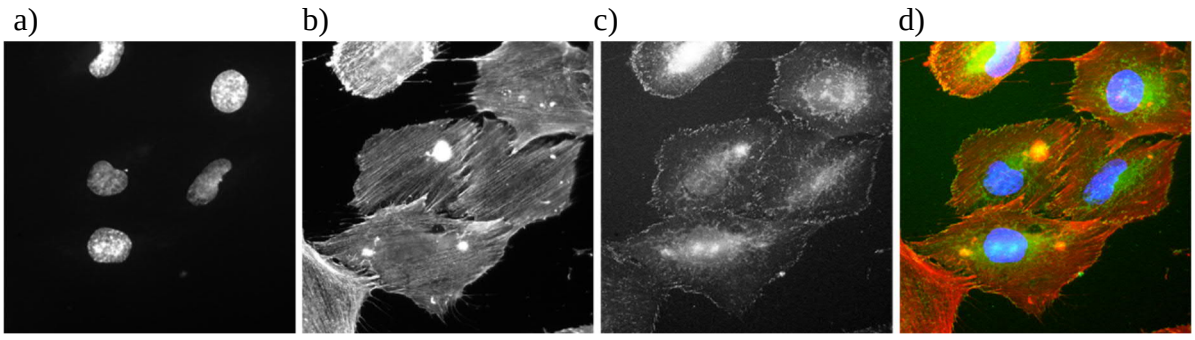

Fig. 74 Fluorescence images of HCF cells stretched with the Q signal, acquired with the 60x immersion-oil objective. Panels: a) DAPI, b) F-actin, c) FAK, d) composite.

In **Fig. 75** the absolute value of the sine of the angles associated with the semi-major axis of the nucleus, the SFs and the cell body are compared for the three different experimental conditions.

In CTRL conditions, the orientation of the nuclei, of the SFs and of the cell bodies give, as outcome, sine values roughly in line with the $2/\pi$ value expected for a uniform distribution. In addition to this, the fact that these values are similar suggests an agreement between the orientation of the cytoskeletal components – SFs and nuclei – with the external body of the cell as it is perceived by the eye.

For the stretched conditions, the value of $\sin(\theta_{zero\text{-}strain})$, marked by the blue dashed line, was added to the plot as a benchmark, useful to understand if also cytoskeletal components of the cell body orient themselves according to this direction. Regarding the T signal, we can notice an overall agreement between nuclei and cell bodies orientation and the sine of $\theta_{zero\text{-}strain}$.

Conversely, the sine of θ_{SF} is slightly higher which leads to infer from the analysis of the cell orientation alone, one would slightly underestimate the sine of θ_{SF} but, still, an acceptable compromise is reached.

Moving to the Q signal, the most evident piece of information regards SFs, which are closer to the $\theta_{zero\text{-}strain}$ reference. Moreover, all three orientational parameters are very similar, reassuring that evaluating the cell body shape still provides an adequate estimate of the orientation of the SFs. The discrepancy between the orientation of the SFs and the $\theta_{zero\text{-}strain}$ direction might find an explanation in a "lag" in the cytoskeleton reorientation. This delay is probably due to a phenomenon named "fluidization", an umbrella term to address the partial disruption of structures in the cytoskeleton which cannot be explained in detail on single-molecule level, but is rather thought to be a broader whole-body response [30].

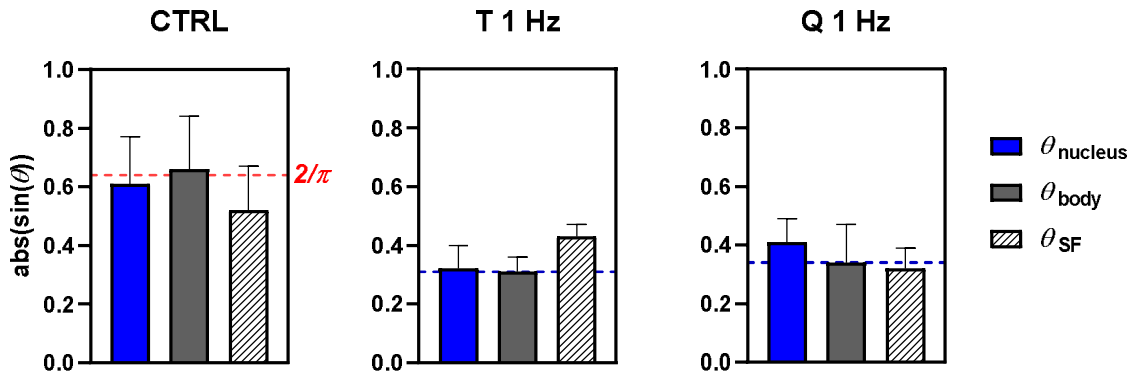

Fig. 75 Absolute values of sin(θ) evaluated for the nuclei, for the body and for the stress fibers (SF) of immunostained cells. The red dashed line represents the sine of a uniform distribution while the blue dashed line is the sine of $\theta_{zero\text{-}strain}$ (N = 20).

To assess the localization of the FAs, the N/C ratio of the FAK fluorescent signal is compared in **Fig. 76a**, for the CTRL, T and Q conditions. In the presence of applied stretching stimuli, the N/C ratio grows in favor of the peri-nuclear compartment, reaching a maximum value for the Q signal. These higher values can be explained by a higher density of FAs below and close to the nucleus which might be an attempt of cells to resist the mechanical perturbation they sense.

In addition to FAK quantification, the YAP localization was carried out too, for a cyclically stretched sample (T 1 Hz) (**Fig. 76b**): showing that the ratio between nuclear and cytoplasmic YAP signal is increased in the presence of an applied stimulus, as recent studies also reported [30], [82].

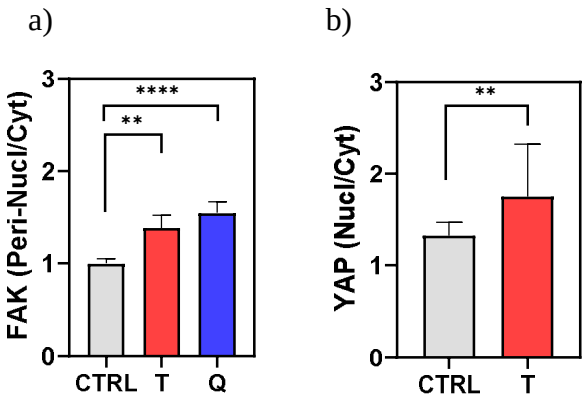

Fig. 76 N/C ratio of the FAK (a) and YAP (b) signals (N = 20).

Gene expression of cyclically stretched cells (RT-qPCR)

The Relative Normalized Expression levels of the genes chosen for the RT-qPCR technique are hereby reported.

In **Fig. 77** the expression levels for the T signal are shown. The TNC gene, responsible for the expression of tenascin, a protein known to interact with fibronectin and able to modify cell adhesion, is upregulated. TNC is also known to be associated with inflammatory responses as reported in [83]. In addition to this, both MMP2 and TIMP, metalloproteinases involved in the degradation of the extracellular matrix, are upregulated. MMP2 upregulation is correlated with transitioning away from the myofibroblast phenotype [84]. This evidence might suggest that cells stretched with the T signal are more prone to inflammation and to engaging interaction with the ECM.

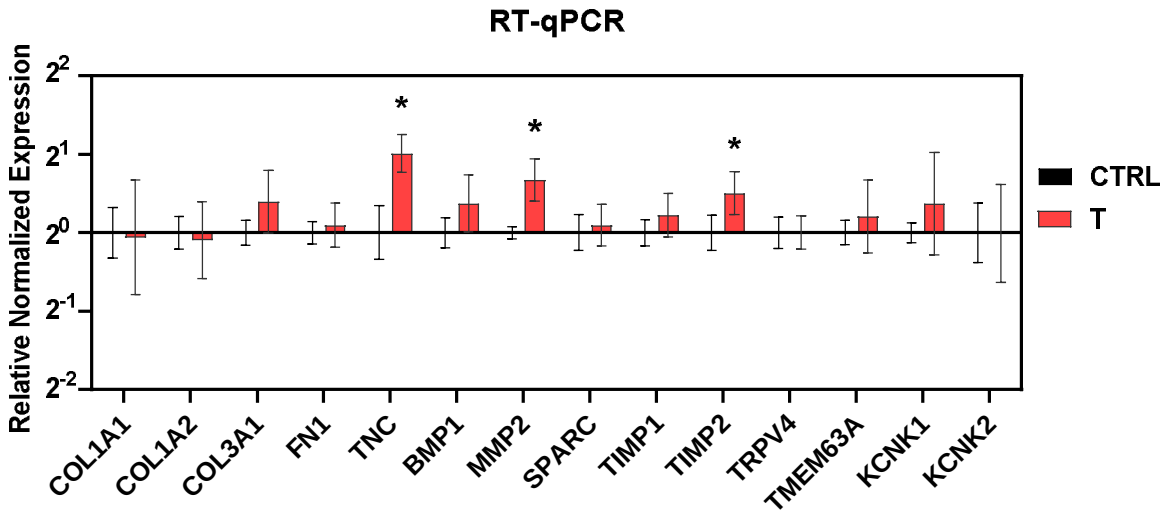

Fig. 77 Relative Normalized Expression values for the different target genes after stretching with the T signal compared to non-stretched controls (CTRL) (N = 3).

The PCR results for the Q signal are reported in **Fig. 78**. From the expression levels, we find the COL1A1 and COL1A2 genes are down-regulated, together with the TRPV4 and TMEM63A ion channels and the potassium channels KCNK1 and 2.

In particular, the KCNK1 and KCNK2 genes are, respectively, ~2 and 4-fold downregulated when compared to the CTRL. KCNK2, in particular, is known to be related to the fibroblast-to-myofibroblast transition. Its over-expression was found to increase differentiation [85] while its depletion and absence is linked to a cardio-protection effect against fibrosis [86]. The downregulation of TRPV4 can also be interpreted as an anti-fibrotic response, since its role was found to be linked with the progression of cardiac fibroblasts into myofibroblasts in mice and its absence was found to reduce fibrosis [87]. In general, considering also TMEM63A, every gene which is responsible for the expression of ion channels, appears to be less expressed. These anti-fibrotic responses could also be linked to the lowered expression of the collagen and fibronectin-related genes.

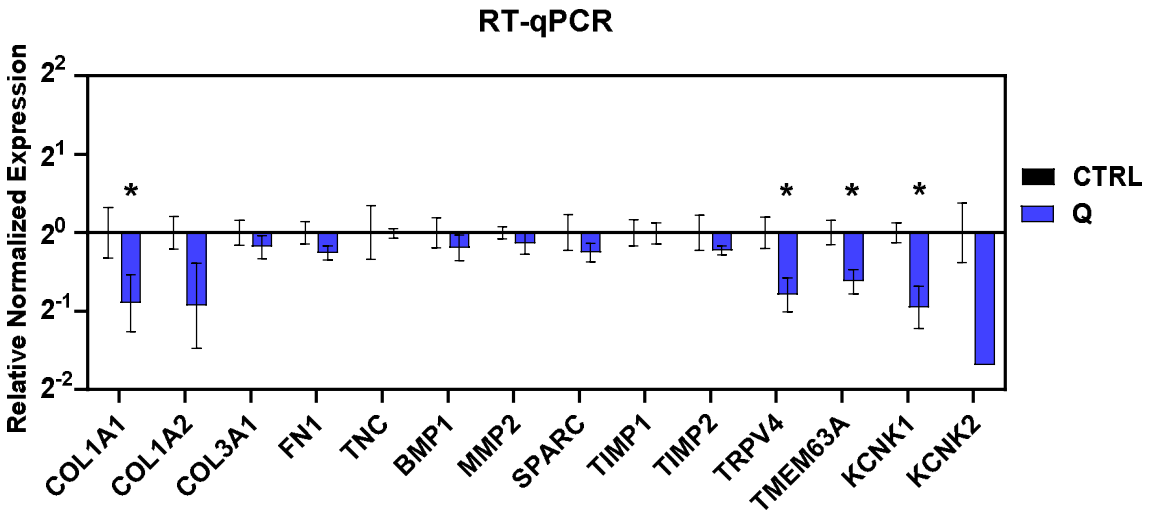

Fig. 78 Relative Normalized Expression values for the different target genes after stretching with the Q signal compared to non-stretched controls (CTRL) (N = 3).

The great difference between the expression levels in the samples exposed to the T and Q points to the major role that the waveform may play in cells response. While the T signal seems to cause inflammation and ECM-degradation, the Q wave triggers a protective response in cells, in particular in mechanosensitive ion channels. In both cases, cells seem to answer positively to the stretching.

4.1.2 Comparison with T signal with f = 0.3 Hz

After scouting the effects induced by different signals, in this Section we will focus on the effect of the stretching frequency. In particular, the results from stretching experiments with the T 0.3 Hz signal, with the same amplitude, are presented. In this way, the two experimental setups presented in this Section and in the former one are performed with different strain rates.

Orientation

In **Fig. 79**, the analysis of the orientation angle after 3 h is shown. Similarly to previous experiments, two mirroring peaks, centered at α = (22 ± 1) ° and β = (155 ± 1) °, are detected.

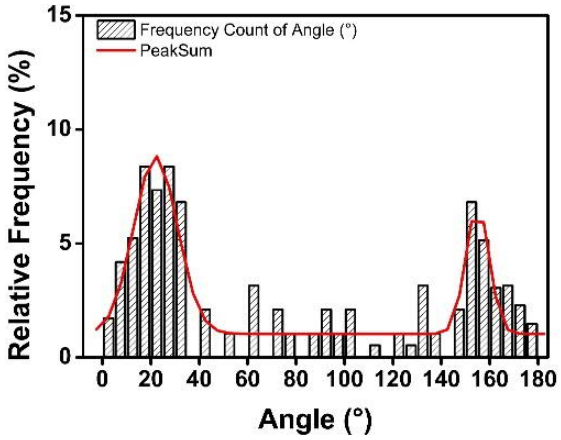

Fig. 79 Frequency distribution histogram of the orientation angles. The red line depicts the output of the Gaussian fit (N = 100).

These orientation angles better match, if compared to the α and β values obtained for T 1 Hz, with the $\theta_{zero\text{-}strain}$ directions of the experimental calibration of the uniaxial stretcher. Comparing the α and β values also with other waveforms at 1 Hz, a strong resemblance with the values for the S 1 Hz signal can be seen. This leads to hypothesize that the orientation process can be finetuned/enhanced either applying softer waveforms at high frequency or harder waveforms at low frequency. In **Section 4.1.3** a better definition of hard and soft signal will be given.

Calculating the *S* parameter a value of (0.7 ± 0.4) is obtained, showing a good degree of accordance between angles and, in general, of ordered configuration. The *b/a* aspect ratio, (0.4 ± 0.2), confirms a slight enhancement in ellipticity in the cell shape, as well as what was observed in the previous cases (**Fig. 80**).

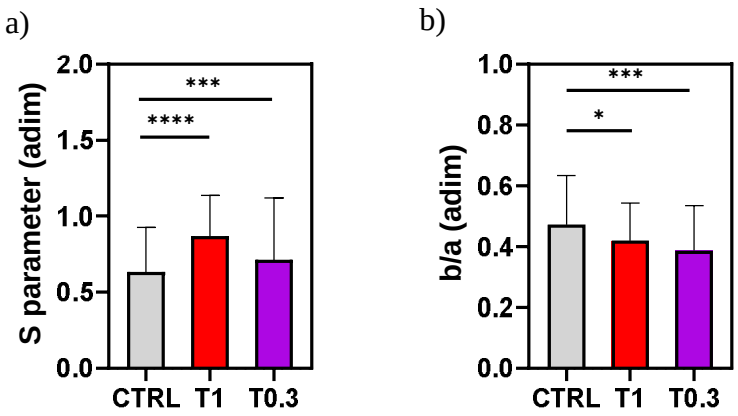

Fig. 80 Histograms of the *S* parameter (a) and the shape factor *b/a* (b) (N = 100).

Single-cell migration

The origin-normalized plot of the analyzed cell trajectories for the T 0.3 Hz signal is shown in **Fig. 81**. The plot reveals a rather uniform distribution of trajectories, with a quite long-range spanning, very similar if not superior to the CTRL condition (see **Fig. 66**). This appearance suggests that cells migrate quite freely over the PDMS surface and might benefit from a slightly enhanced migration.

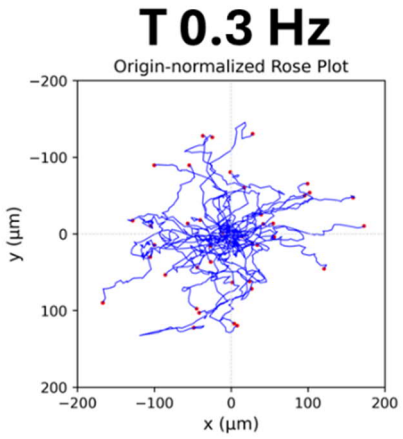

Fig. 81 Origin-normalized plot with the trajectories of cells. The red dots represent the final position reached in 3 h of experiment.

The same observation finds confirmation by looking at the traveled distance (**Fig. 82a**) and MSD plots (**Fig. 83**), where we can see that cells subjected to the T 0.3 Hz signal travel a mean distance of (206 ± 65) µm and that the MSD(t) curve is slightly higher than the CTRL. From the PRW fitting of the MSD(t) curve, also the coefficient of diffusion *D*, results increased,

with a corresponding a value of (14 ± 4) μm^2/min. The mean speed of the cell sample (**Fig. 82b**) further justifies the more rapid migration as it amounts to (1.2 ± 0.4) μm/min, the maximum value registered in the different experimental setups.

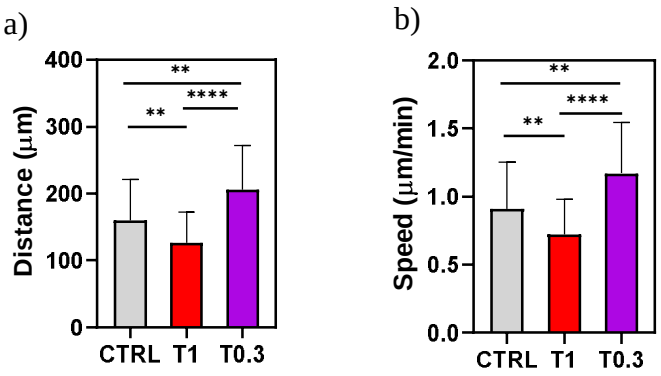

Fig. 82 Histograms of the traveled distance (a) and the mean speed (b) (N = 50).

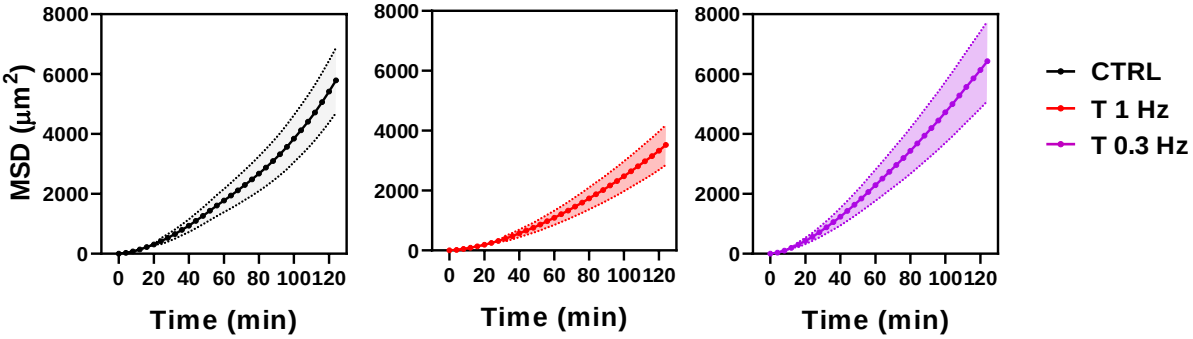

Fig. 83 Mean Square Displacement over time (N = 50).

In the case of the 0.3 Hz triangular signal, migration appears less oriented, as proven by the radar plot of the overall migration angle θ_{final} (**Fig. 84a**) which is less defined if compared to previous data. The same information can be seen also in the histogram that presents the absolute values of the sine of θ_{final} (**Fig. 84b**): the reached mean value, (0.59 ± 0.05), is quite close to the $2/\pi$ value of a uniform distribution.

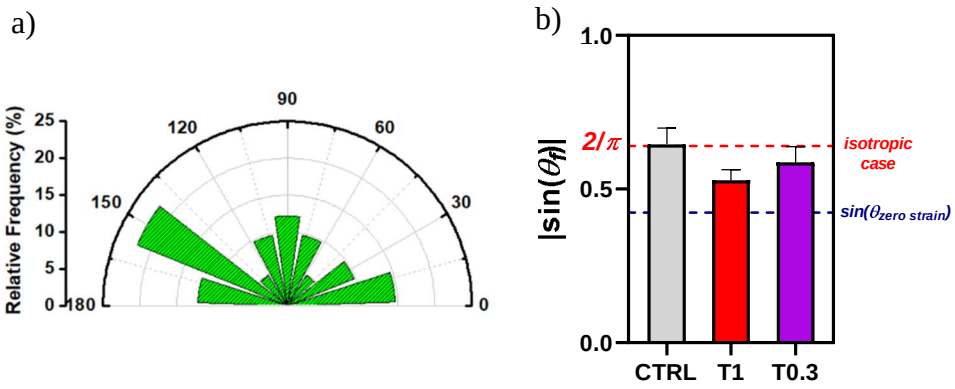

Fig. 84 Radar plot of $|\theta_{final}|$ (a) and of histogram of $|sin(\theta_{final})|$ (b) (N = 50).

4.1.3 Breakdown of the different stretching protocols

The previous Sections aimed at evaluating the impact of different waveforms and frequencies in cell migration and orientation, without characterizing the different stretching cues we provided. In this Section, a comparison between the different signals is provided as well as a qualitative classification of the protocols in terms of "hardness/softness".

In **Fig. 85** top row, the different waveform profiles, with f = 1 Hz and 100 step peak-to-peak amplitude, are given by the black lines. The graphs in the bottom row (blue lines) represent the deformation rate while the red dots highlight either the discontinuity points in which the rate is subject to a sudden change or the points in which the stepper motors changed their direction (points with the same x value were counted only once). We can think of these as "critical points" that periodically "hit" the system.

As it is quite evident, each waveform is characterized by its own peculiarities and a direct comparison between signals is not immediate. In **Table 5** an overview of each protocol's key characteristics is thus provided.

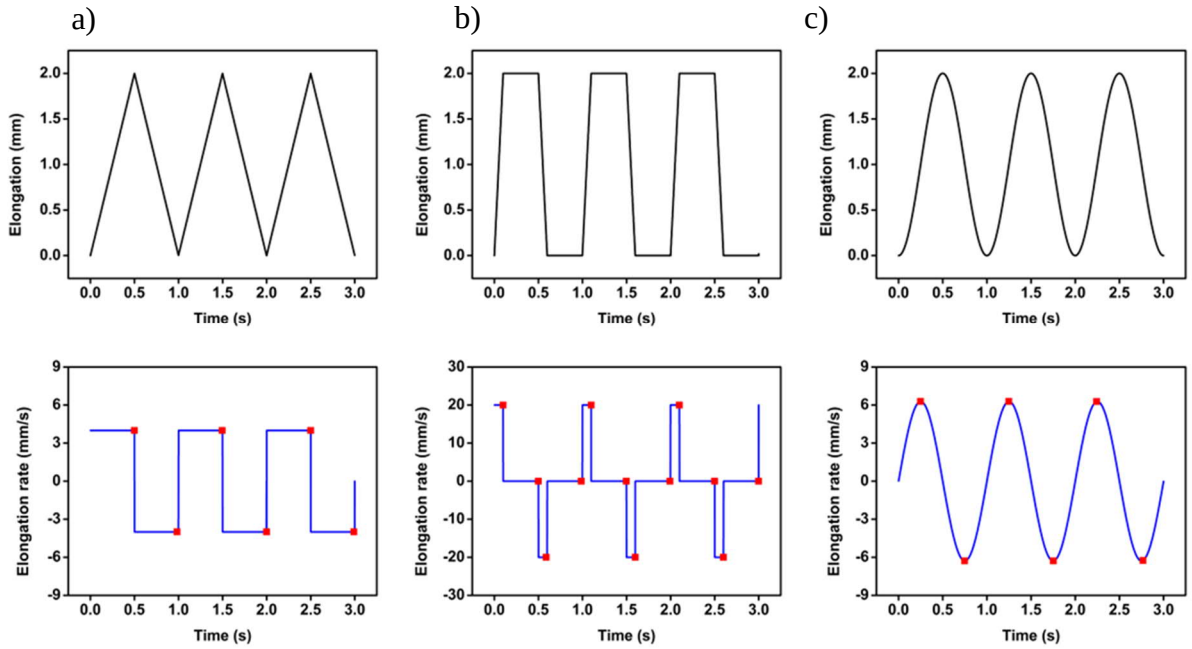

Fig. 85 Top row: elongation profiles supplied per side of the PDMS substrate by the a) T, b) Q and c) S stretching signals (black line) with 100 steps peak-to-peak amplitude and f = 1 Hz. Bottom row: elongation rate for each condition; in red, the critical points.

The triangular signal (**Fig. 85a**) gradually deforms the PDMS substrate providing a constant modulus of the deformation rate (4 mm/s). The discontinuity points for this signal, corresponding to a change in the rate sign, occur when the maximum deformation is reached and at the beginning of every new cycle of stretching. In these points (2 per cycle) the stepper motors of the stretcher device abruptly change their rotation direction, providing about ~ 32 000 sudden variations in a 3-hour-long experiment.

The square signal (**Fig. 85b**) is clearly the steepest and applies the highest rate in absolute value, which amounts to 20 mm/s. The waveform was purposedly designed to apply the most deformation in the shortest time possible for the stepper motors. Moreover, the number of discontinuity points provided by this signal is very high (6 per cycle), as there are not only the points in which the stepper motors change direction, but also the points in which the pauses in applying the deformation are quickly interrupted. Counting how many times these abrupt changes occur in 3 h of experiment, they amount to ~ 43 000 hits. This extremely rapid deformation and these “turbulence” points might disturb the survival of the focal adhesion complexes, thus hindering migration, in agreement with the shrunk trajectories observed. This interpretation is also supported by the higher N/C ratio of the FAK signal, as discussed in **Section 4.1.1**, in which FAs concentrate in the peri-nuclear area rather than in the perimeter of

the cell body. Another confirmation of the disruptive effect of high loading rates is also provided by the molecular motor-clutch, in the occurrence of frictional slippage in the system.

Even though its profile strongly resembles the triangular one, the sinusoidal signal (**Fig. 85c**) is intrinsically different. Its deformation rate is not constant but smoothly increased and decreased. In fact, the signal starts with rate zero, which is then gradually risen to a maximum value of 6 mm/s, at about half of the maximum elongation. After that, prior to reaching the maximum elongation, the rate is gradually reduced to zero again. No discontinuity point is detected, since the waveform is a continuous function with a continuous first derivative, but 2 inversion points per cycle, due to the stepper motors inversion, are counted (~ 32 000 hits in 3 h). This gentle "bouncing" between acceleration and deceleration ramps in absence of abrupt rate changes provides a moderate stimulus to cells. This could be the explanation as to why the S signal, as discussed in **Section 4.1.1**, provides the best re-orientation of cells while preserving most of their motility among the 1 Hz signals.

Lastly, the triangular signal with f = 0.3 Hz is analyzed (**Fig. 86**). The signal provides a constant value of rate modulus equal to 1.2 mm/s and counts the same 2 discontinuity points per cycle previously observed for the T 1 Hz signal, amounting to ~ 6 500 hits in 3 h. The T 0.3 Hz signal was proven to be the better compromise for both orienting cells while preserving their motility, suggesting that the milder the stimulus the better the cells performance.

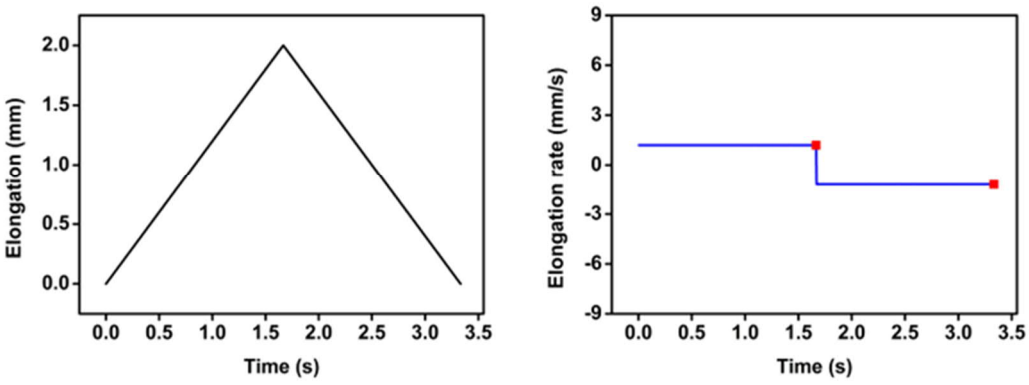

Fig. 86 Elongation profile per side of the PDMS substrate supplied by the T stretching signal (black line) with 100 steps peak-to-peak amplitude and f = 0.3 Hz. The blue line depicts the deformation rate; in red, the critical points.

From this semi-quantitative analysis, in the last column of **Table 5**, a classification of the stretching protocols is proposed in terms of softness/hardness, based on the order of magnitude of the number of critical points encountered during an experiment (**Fig. 87**).

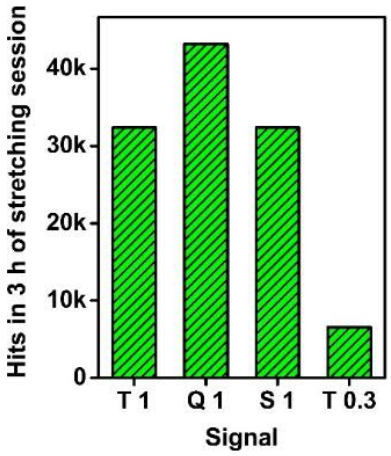

Fig. 87 Estimation of the number of critical points in 3 h of experiment with the different signals.

Table 5 Summary of the details about the different stretching protocols.

Waveform	Amplitude (steps)	*f* (Hz)	Max rate (mm/s)	Rate application	Critical pts in 3 h	Classification
T	100	1	4	Constant rate modulus, abrupt change in sign	~ 32 000 (2/cycle)	Moderate
Q	100	1	20	Constant rate modulus, abrupt change in sign and pauses points	~ 43 000 (6/cycle)	Hard
S	100	1	6	Variable rate, smoothly variated	~ 32 000 (2/cycle)	Moderate
T	100	0.3	1.2	Constant rate modulus, abrupt change in sign	~ 6 500 (2/cycle)	Soft

4.2 Biaxial stretcher experiments (90°-inversion experiments)

In this Section, the effects induced by a 90°-inversion in the stretching direction are presented. The series of experiments here reported were performed stretching cells with the T signal, at f = 1 and f = 0.3 Hz for an initial session lasting 3 h. Next, the stretching direction was rotated by 90° and cells were fixed after 30 min or 1 h.

4.2.1 T signal with f = 1 Hz

Orientation

During the first 3 h of stretching protocol, when cells are subjected to a stimulus applied along the x motor-axis, the same responses already discussed in **Section 4.1** are consistently found with minor differences due to the different geometry of the stretcher device. In brief, cell bodies align preferentially close to the zero-strain mirror directions experimentally found for the single-axis working mode of the biaxial stretcher: θ_1 = (17 ± 11) ° and θ_2 = (158 ± 10) ° (**Table 3** in **Chapter 3**). The outcome of this first stretching session is plotted in **Fig. 88a**, where the frequency distribution of the orientation angle at t = 3 h returns two peaks, centered at α = (20.1 ± 0.8) ° and β = (165.5 ± 0.6) °.

Once the direction of perturbation is switched to the y-motor axis, cells promptly sense the new stimulus and start chasing the new zero-strain directions which now are θ_1 = (68 ± 11) ° and θ_2 = (109 ± 10) °.

The frequency distribution of the orientation angles after 30 min of stretching along y are shown **Fig. 88b**, where a single broad peak appears at (86 ± 3) °.

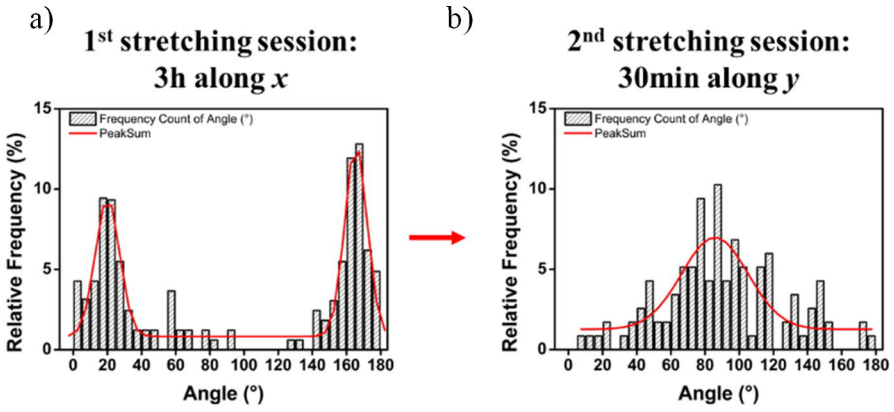

Fig. 88 Frequency distribution histograms of the orientation angles (N = 100). The red line depicts the output of the Gaussian fit.

Allowing the second stretching session to last until 1 h, the frequency distribution of the orientation angles (**Fig. 89**) finally shows two peaks now centered at α = (70 ± 2) ° and β = (102 ± 2) °.

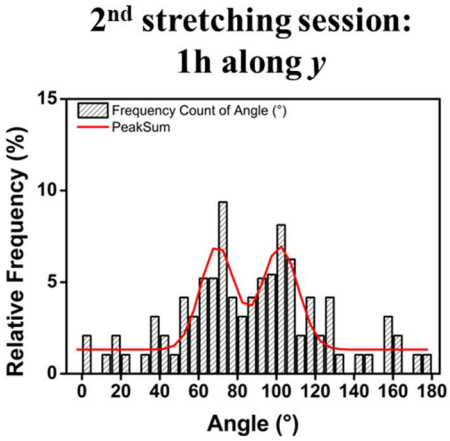

Fig. 89 Frequency distribution histograms of the orientation angles (N = 100). The red line depicts the output of the Gaussian fit.

By comparing the orientation distributions achieved at different times it is possible to estimate the fraction of cells that have not yet recovered their orientation after 30 min, meaning that, if they had more time, they would have reached the peaks found after 1 h (**Fig. 90**). The dashed blue area depicts the fraction of cells that, after 30 min, have already reached the same orientation they would retain at 1 h. This portion of cells results to be around 80% of the entire sample. Next to this, the gray area represents the fraction of cells that could benefit from a longer time scale, amounting to 20% of the sample. One could draw the conclusion that 30 min is a sufficient time to recover most of the orientation but that finetuning to the zero-strain directions requires at least 1 h.

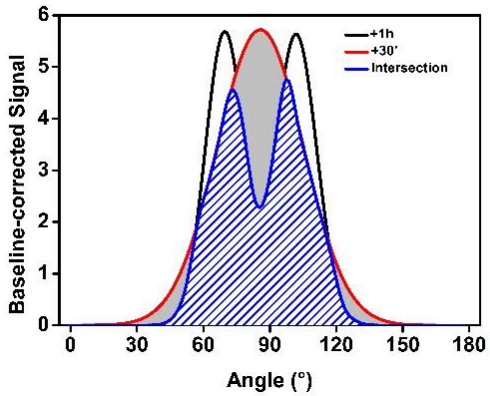

Fig. 90 Comparison of the orientation effectiveness at different duration of the second stretching session. The dashed blue area is given by the intersection of the baseline-corrected plots at 1 h (black line) and 30 min (red line).

Evaluating the *S* parameter (**Fig. 91a**), prior to inversion, the 3-hour-long first stretching session provides an *S* value of (0.9 ± 0.3) which is superimposable to the corresponding value found in uniaxial experiments. After the inversion, *S* drops momentarily to lower values and then starts increasing as cells regain orientation; in particular, after 30 min *S* is restored to (0.7 ± 0.3) and, at 1 h it is slightly larger, (0.8 ± 0.4). The *b/a* factor (**Fig. 91b**) also underlines a small loss in ellipticity in cell shape, which is more accentuated at short (0.5 ± 0.1) rather than at long times (0.4 ± 0.1).

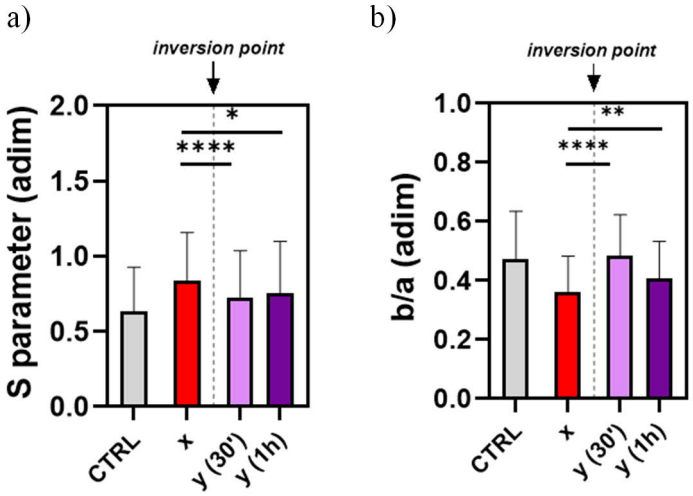

Fig. 91 Histograms of the *S* parameter (a) and the shape factor *b/a* (b) (N = 100).

Immunofluorescence

Fig. 92 a, b report immunofluorescence images of the F-actin signal of samples of cells 30 min and 1 h after the inversion. In both cases, the signal results to be blurry and spread over the whole cell body, without distinct well-defined fibers. At high magnification (**Fig. 92 c, d**), in some cells, very thin and short strands could be noticed, maybe interpretable as proto-fibrillar structures. This sort of "solubilization" of the F-actin signal makes the FFT processing for establishing their orientation inconclusive, since it returns a homogeneous output with no defined angular contributions.

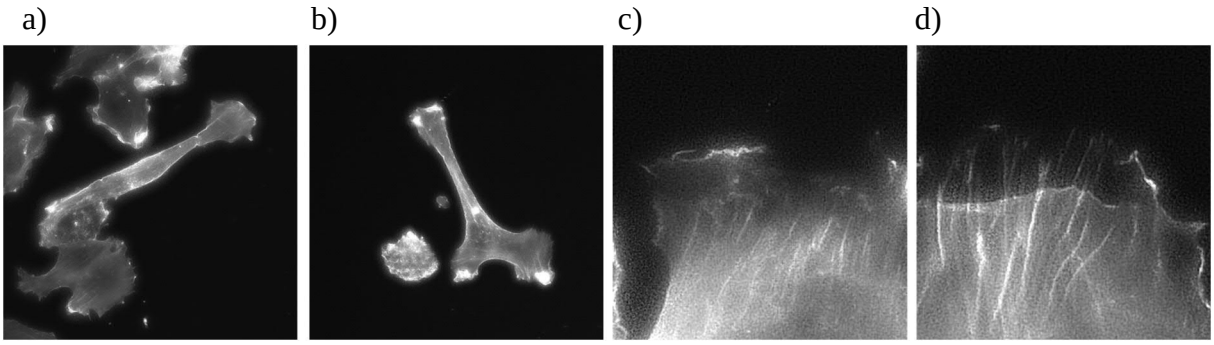

Fig. 92 Fluorescence images of the F-actin in HCF cells 30 min (a) and 1 h (b) post-inversion acquired with the 40x objective. (c, d) Zoom into proto-fibrillar structures.

Below, in **Fig. 93**, paxillin-stained samples are reported: control cells in the top row and stretched samples after 30 min and 1 h from the inversion point, respectively middle and bottom rows. In CTRL cells, paxillin spots are well-defined, in correspondence of the ventral region and quite distributed in the cell body. Considering 90°-inversion experiments, paxillin becomes more concentrated at the cell borders while in the peri-nuclear region a faint blurry halo appears.

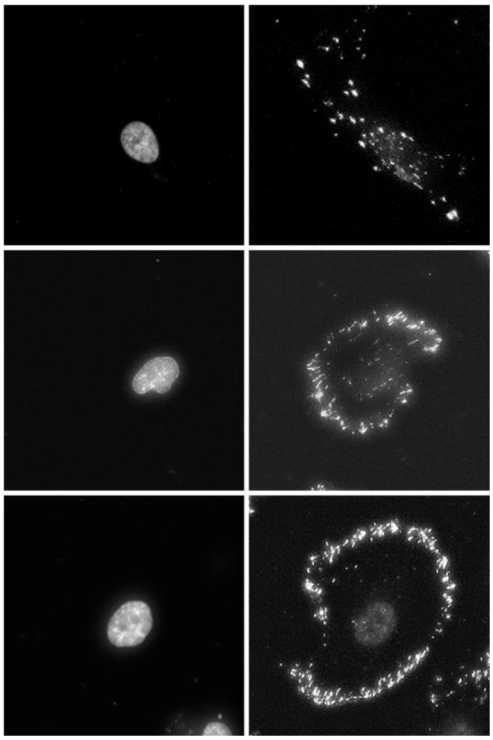

Fig. 93 Fluorescence images of paxillin in HCF cells acquired at the 40x. Top row, control cells; middle row, cells after 30 min from inversion; bottom row, after 1 h.

From the quantification of the N/C ratio for the peri-nuclear and the cytoplasmic fluorescent signals of paxillin (**Fig. 94**) it is confirmed that the protein is effectively mainly located in the peri-nuclear area in CTRL conditions. At the end of the first stretching session the N/C ratio remains unaltered but, 30 minutes after the inversion, a significant drop describing the recruitment of paxillin in the cytoplasm is registered [88].

This aspect is related to the disassembly of the focal adhesions, caused by the abrupt application of a new stretching stimulus, and could also be linked to a fluidization phenomenon. At longer times of the second stretching session the pristine paxillin distribution is restored.

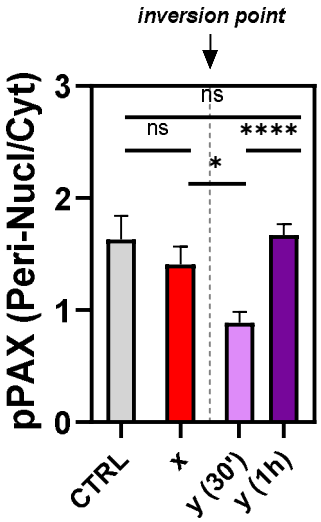

Fig. 94 N/C ratio of the paxillin signal in HCF cells (N = 20).

4.2.2 T signal with f = 0.3 Hz

Orientation

Unlike the 1 Hz experiment previously presented, the recovery of cell orientation after the inversion point at 0.3 Hz takes more time to occur. The first stretch session of the duration of 3 h results in α = (23 ± 3) ° and β = (164 ± 1) °, as expected. Surprisingly, the comparison between the orientation achieved after 30 min and 1 h from the inversion point returns, in both cases, only one broad peak, centered at (93 ± 2) ° and (80 ± 2) ° respectively (**Fig. 95**). The only parameter which might suggest an onset in orientation recovery after 1 h is the full width at half maximum (FWHM): in fact, the FWHM for the peak at 30 min is 56 ° and, at 1 h, it is 67 °. This subtle detail might hint at a partitioning of two populations (which were always referred to as α and β angles in previous Sections) which is probably just about to start, if given more time.

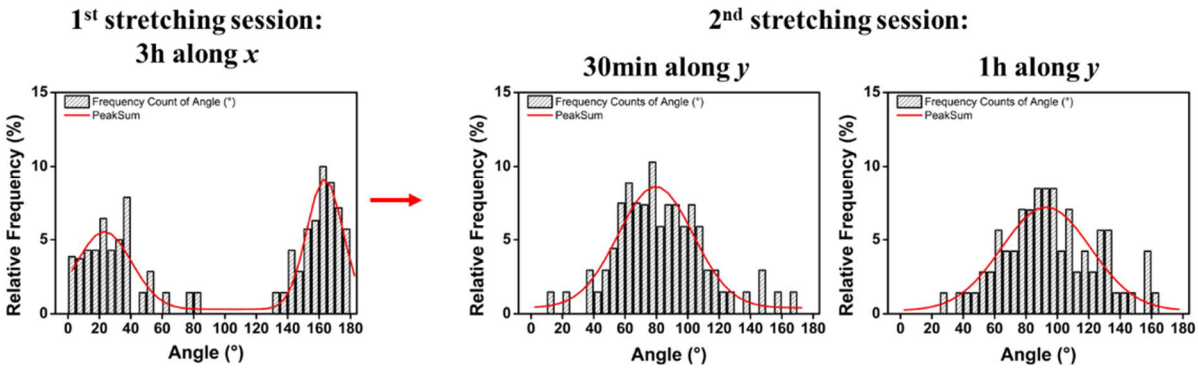

Fig. 95 Frequency distribution histograms of the orientation angles (N = 100). The red line depicts the output of the Gaussian fit.

In **Fig. 96a** the evolution of the *S* parameter is presented. The first stretching session, along the *x* axis, provides an *S* value of (0.7 ± 0.3), in line with the uniaxial case observed for the T 0.3 Hz signal (**Section 4.1.2**). After the inversion, the *S* value increases to (0.8 ± 0.2). No relevant difference is observed comparing the order parameters achieved after 30 min *versus* 1 h and no reduction is revealed. This evidence suggests that the application of a different stimulus is an event that cells deal with quite smoothly, switching to chasing the new zero-strain direction without losing the degree of order they previously achieved.

Regarding cell shape, after 30 min from the inversion point the shape factor becomes relevantly more circular (**Fig. 96b**) and then recovers, after 1 h, to the same initial values.

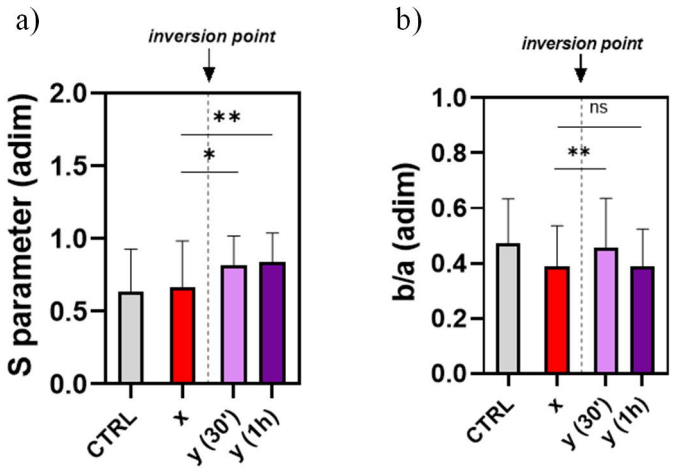

Fig. 96 Histograms of the *S* parameter (a) and the shape factor *b/a* (b) (N = 100).

Immunofluorescence

In **Fig. 97** the immunofluorescence of cells after 30 min (top row) and 1 h (bottom row) from the inversion are reported. Looking at the b panels, which present the F-actin signal, the same findings presented in the previous Section are still valid. F-actin is again poorly condensed in fibers, but rather in feeble filaments. The aspect of the paxillin signal (panel **c**) as well recalls what was discussed previously.

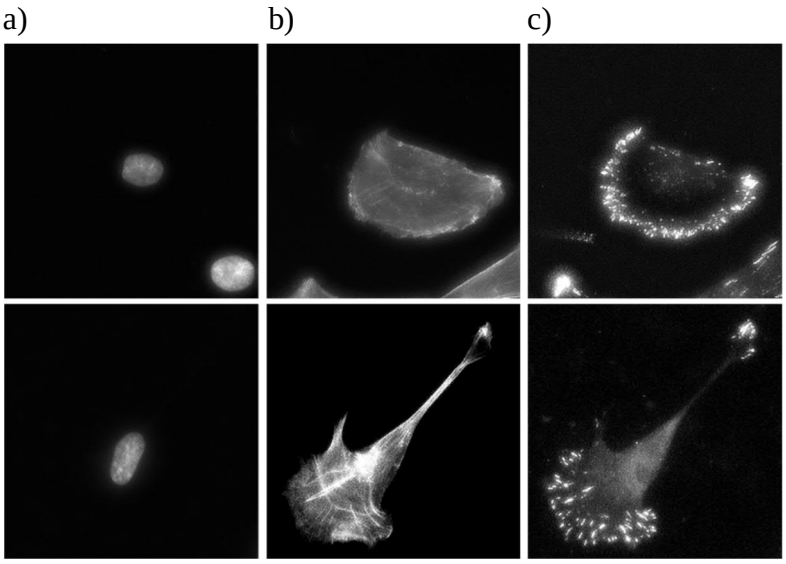

Fig. 97 Fluorescence images of HCF cells acquired at the 40x. In the top row, cells after 30 min from inversion; bottom row, after 1 h. DAPI (a), F-actin (b), paxillin (c) channels.

The N/C ratio of paxillin seems to remain constant over the whole experiment course, which could support the hypothesis that the inversion, in the T 0.3 Hz signal, results in a less destructive event for cells (**Fig. 98**).

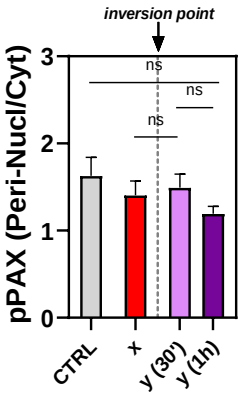

Fig. 98 N/C ratio of the paxillin signal in HCF cells (N = 20).

4.2.3 Mechanisms of re-orientation

The re-orientation process in response to a stretching stimulus for fibroblasts is already known to occur following two main modes [43], which have been defined as the *strain mode* and the *rotation mode* [89] (**Fig. 99**). In the first case, cells orient themselves assuming a circular shape, depolymerizing existing stress fibers and, in a second instance, re-forming them; the second case can be described as a rigid body rotation, in which cell shape is not significantly altered and the whole cell cytoskeleton is simply rotated towards a new direction.

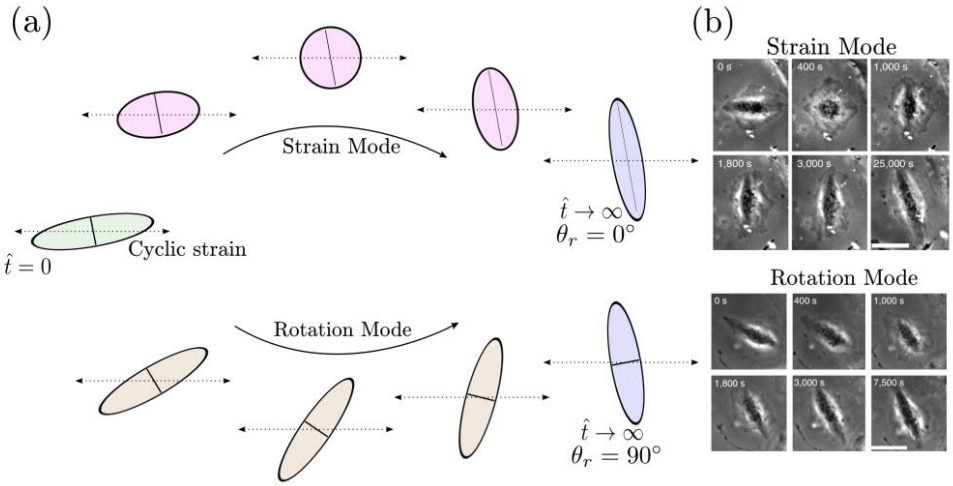

Fig. 99 On the left, schematic representation of the two orientation modes taken from [89]. On the right, optical images of fibroblasts undertaking both modes [43].

Similarly to Livne et al.'s observations, also HCF fibroblasts reorient according to the same two mechanisms, especially when a second stretching session, perpendicular to the previous one, is applied. In **Fig. 100** and **Fig. 101** two examples of HCF cells during the 90°-inversion experiments have been reported. In particular, **Fig. 100** depicts a cell undergoing the strain mode, while the cell in **Fig. 101** prefers the rigid-body rotation.

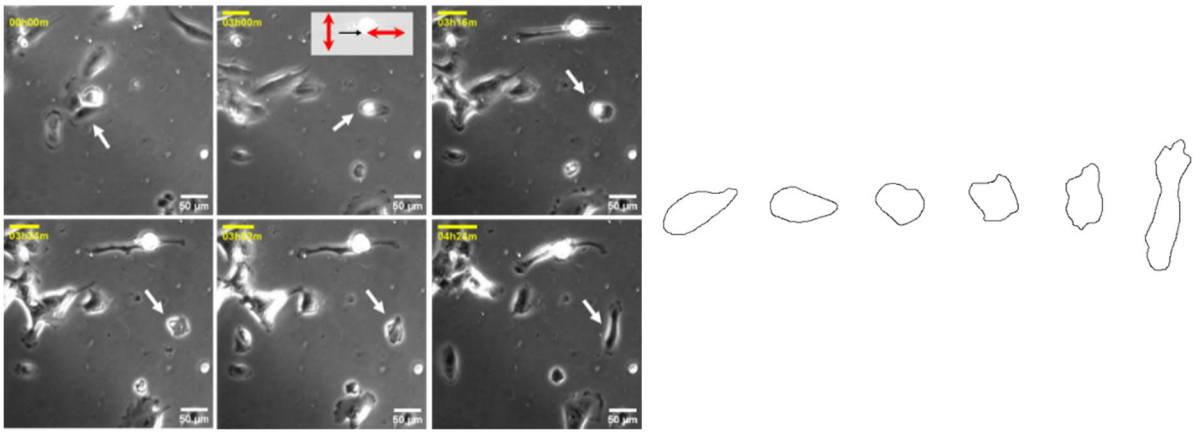

Fig. 100 Example of a HCF cell (pointed by the white arrow) that contracts and then spreads in response to the new stretching direction. At the side, its contour at the same time points of the pictures on the left.

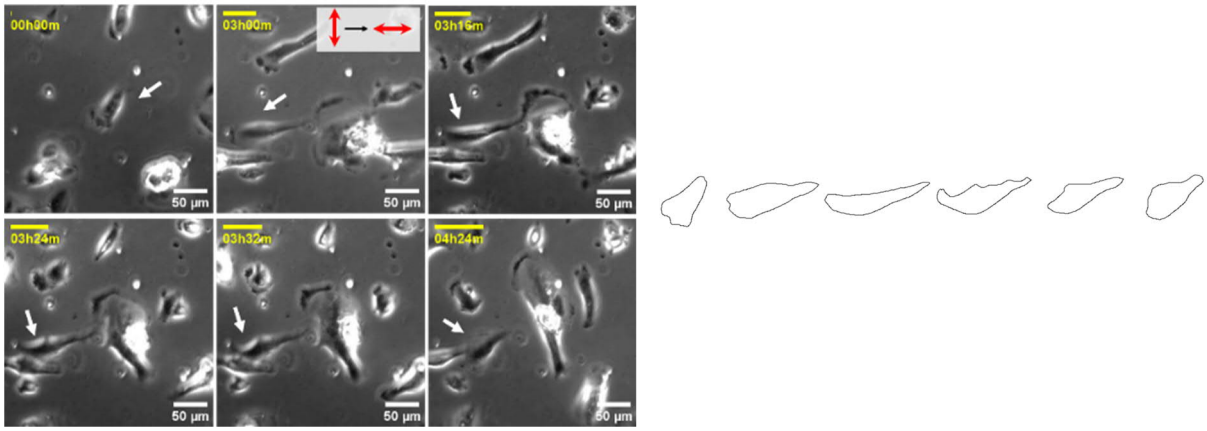

Fig. 101 Example of a HCF cell (pointed by the white arrow) that rotates keeping its shape in response to the new stretching direction. At the side, its contour at the same time points of the pictures on the left.

Parallel to these images, the progression in time of the orientation angle and the shape factor *b/a* of both cells is reported below in **Fig. 102**. In the strain mode orientation (**Fig. 102a**), the *b/a* value spikes to high values right afterwards the inversion point, describing a loss in cell orientation which is later recovered. Alongside that, the angle progression shows that the cell undergoes rotation in a clockwise direction and keeps the same direction even after the inversion point. In the rigid-body rotation mode (**Fig. 102b**) cell orientation is preserved for the whole time-lapse, while the angle evolution describes firstly, a clockwise rotation, which is then turned into counterclockwise after the inversion. These two behaviors are both present in the 90°-inversion experiments performed and discussed previously. Interestingly, we found that the partitioning of cells undergoing either mode depends on the frequency of cyclic stretching.

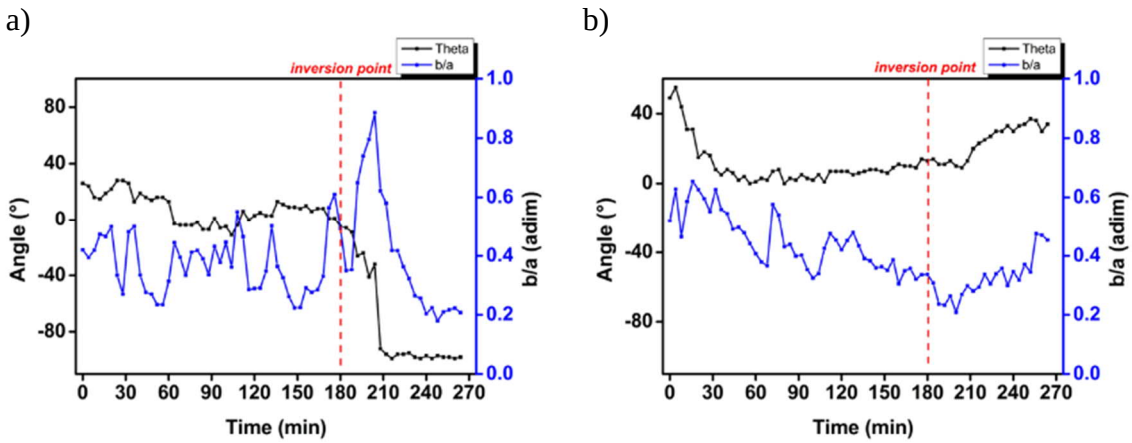

Fig. 102 Progression of the angle and *b/a* ratio for two cells orienting according to the strain mode (a) and rotation mode (b).

When the stretching direction is switched with the T 1 Hz signal the majority of cells are found to prefer the strain mode to the rigid rotation, with an estimated distribution of 75% *versus* 25%. Conversely, with the T 0.3 Hz signal, the two modes occur approximately with a 50-50 distribution.

4.3 Conclusions

Uniaxial stretching experiments with constant amplitude and frequency (100 steps, 1 Hz) provided a foundational basis for outlining the HCF response to mechanical stimuli and for interpreting more complex experiments. Under these conditions, the different applied waveforms (triangular, square, sinusoidal) produced similar results regarding cell orientation and migration. Generally, stretching leads to a more or less pronounced loss in cell migration capability (noticeable in the total distance, mean square displacement and diffusion coefficient) and in cell speed, in addition to directing the overall migration direction toward the zero-strain directions. Moreover, cell orientation and the degree of alignment indicate that cells align, to a reasonable extent, along the zero-strain directions [38] and that highly ordered configurations are attained. Minor differences in the outcomes hint that milder signals, especially the sinusoidal waveform, allow to achieve better orientation results and inhibit the migration capability of the cells to a minor extent. Immunofluorescence imaging reveals that stretching causes YAP to translocate to the nucleus, activating gene expression, while paxillin and FAK signals in the cytoplasm suggest that peripheral focal adhesions are disrupted by the stimulus. Stress fibers align approximately along the zero-strain directions, although a slight "delay" in

achieving perfect alignment is observed for harsher signals (square waveform), possibly indicating cytoplasmic fluidization. Expression levels of specific genes suggest that different waveforms yield a fingerprint signature in gene expression. Cells stretched with the triangular and square signal returned different expression profiles; however, in both cases, the response indicated a possible positive adaptation to the stretching stimulus.

From the comparison with a low-frequency stimulus, we find that smoother and gentler cues help preserve cell migration capability while achieving a better degree of orientation.

The biaxial stretcher device was then exploited to pre-condition cells with an initial uniaxial stretching stimulus and then to impose an abrupt change in the stretching direction, simulating an injury. The initial stretching session produced results consistent with those obtained in the previous series of (uniaxial) experiments. When the stretching direction is switched to the perpendicular one, cell re-orientation was found to occur in two modes already documented in the literature, the strain mode and the rotation mode. The distribution into these two re-orientation mechanisms was found to be sensitive to frequency, with high frequency favoring the strain mode. Immunofluorescence imaging reveals that the paxillin distribution between cytoplasmic and peri-nuclear areas is disturbed by the application of high frequency signals: 30 minutes after the inversion a greater cytoplasmic concentration is detected, which is then recovered after 1 h. For low-frequency signals, this response does not occur, with the distribution of paxillin remaining unaltered. However, in both cases, stress fibers are heavily interested by the inversion in the stretching direction and only feeble and wobbly threads of actin filaments were found, leading us to hypothesize that fluidization of the cytoskeleton might play an important role in the response mechanism to heart tissue injuries.

Below, **Fig. 103** and **Fig. 104** offer a summary of the results achieved by stretching HCF cells with uniaxial and biaxial stretch respectively.

Fig. 103 Schematic overview of the effects of uniaxial stretch.

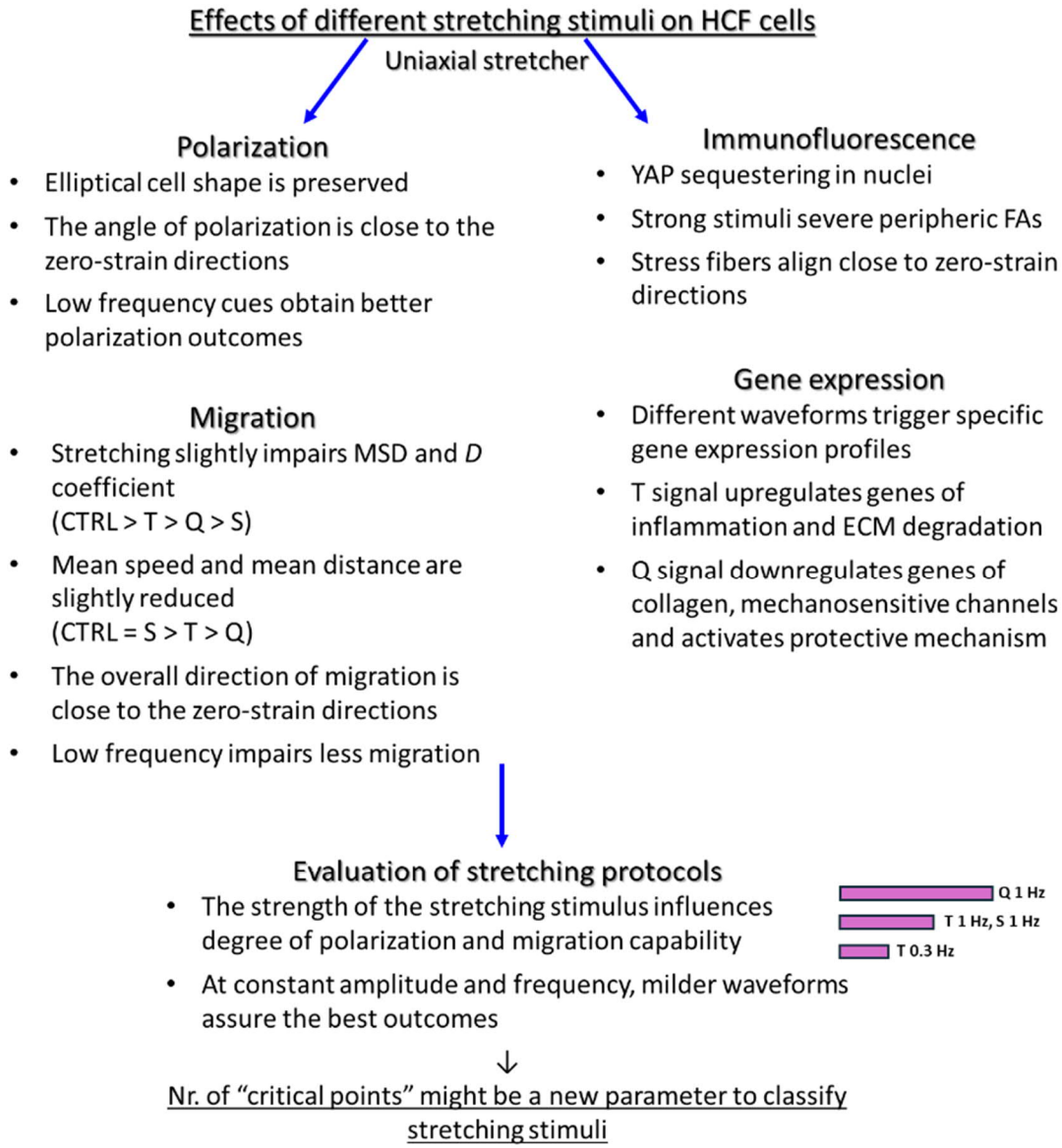

Fig. 104 Schematic overview of the effects of biaxial stretch.

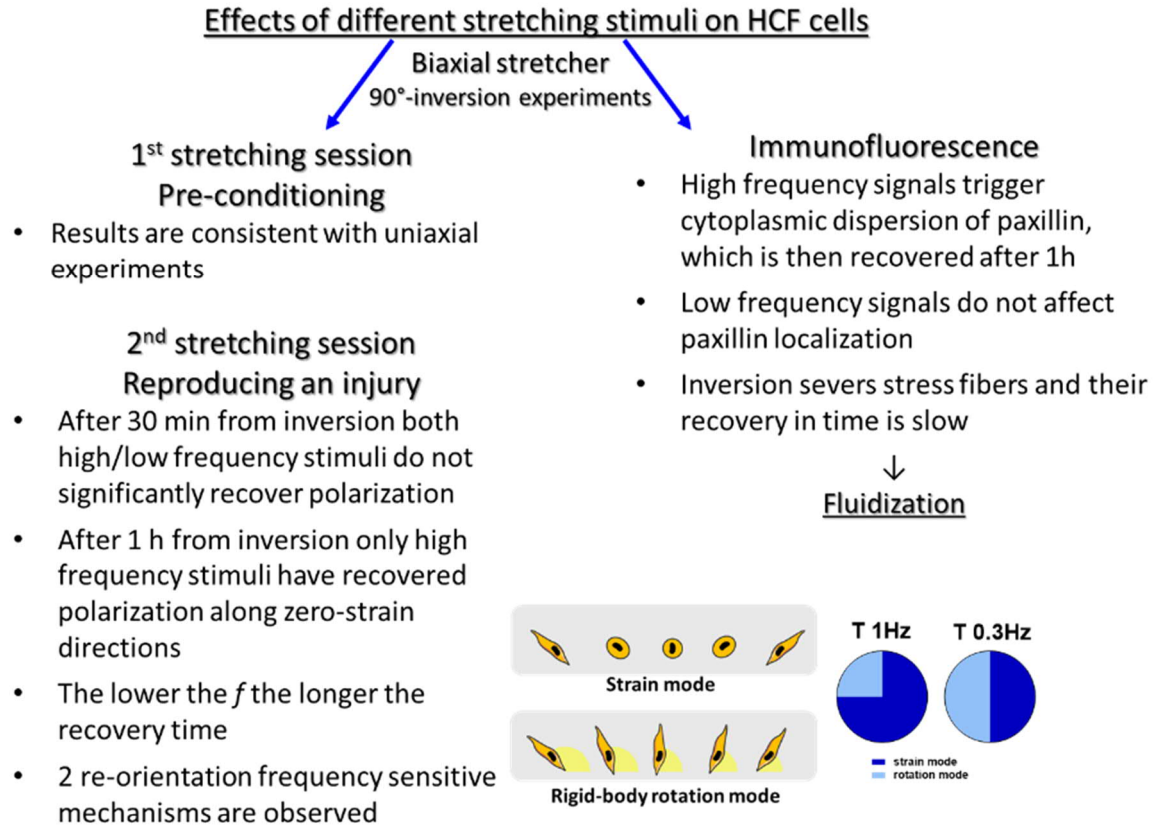

Chapter 5 – Results of the experiments with U87MG

This Chapter focuses on the results achieved with U87MG experiments.

In **Section 5.1** the results of the treatment of U87MG cells cultured in multi-wells and treated with 1*g* are presented. In particular, in **5.1.1**, a focus on the effects of the drug at low concentrations, investigating its influence on both single-cell migration and on cell duplication is given. In **5.1.2** an evaluation of the collective migration of the cells treated with 1*g* 20 μM is presented.

In **Section 5.2** the effects of spatial confinement on cell migration are analyzed, presenting the outcomes of experiments with U87MG cells cultured on μ-patterned PDMS substrates and treated with different concentrations of blebbistatin.

5.1 Effects induced on U87MG cells by the treatment with 1*g*

5.1.1 Effects of low concentration treatments in single-cell experiments

Single-cell migration

Fig. 105 portrays the origin-normalized trajectories of the cells tracked to evaluate migration. Qualitatively speaking, there is no very evident difference between the trajectories spanned by each cell sample but, in **Fig. 106**, the MSD(t) curves better distinguish each case.

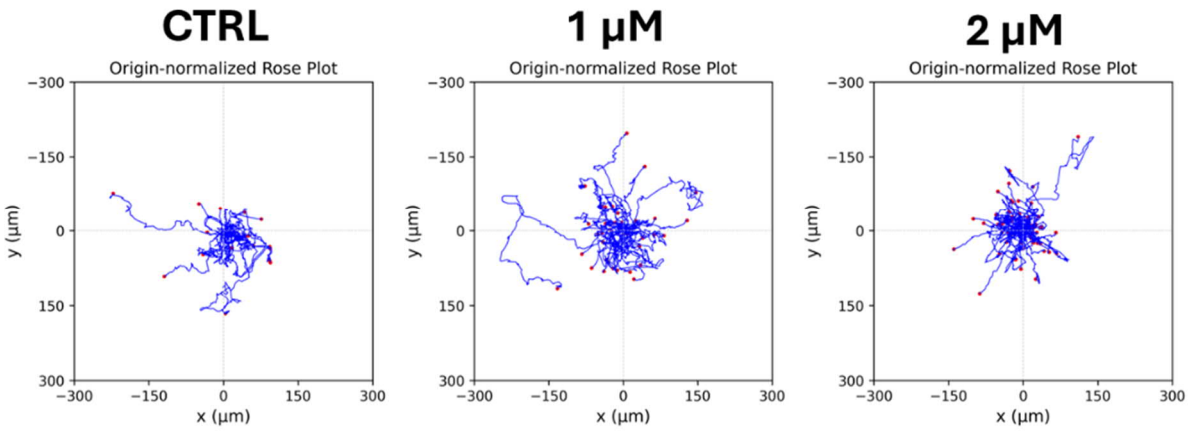

Fig. 105 Origin-normalized plots with the trajectories of U87MG cells tracked in the migration assay. The red dots represent the final position reached in 6 h of experiment.

The different MSD(t) curves point out that 1*g* slightly impairs migration: the MSD value of 1 μM sample, at t = 6 h, is approximately 30% smaller than the CTRL, while the 2 μM is about 60%.

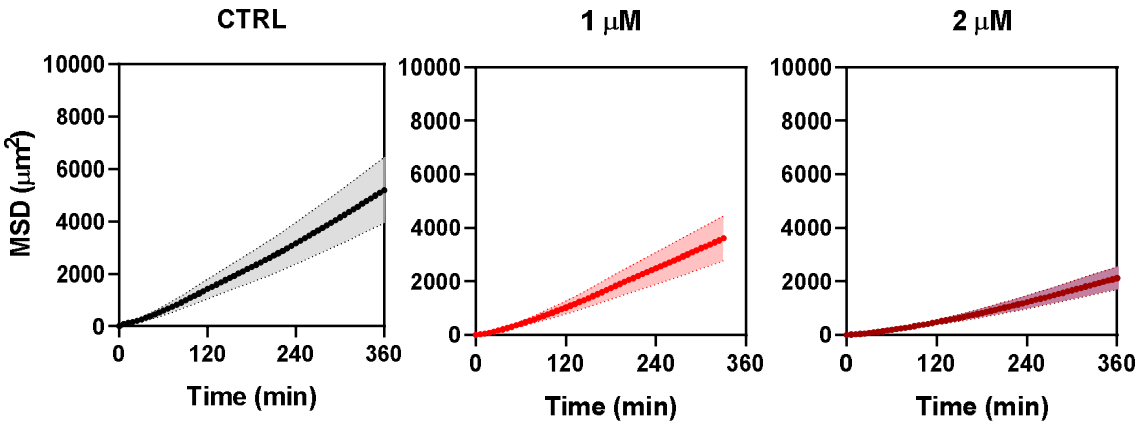

Fig. 106 Mean Square Displacement of U87MG cells treated with different concentration of 1*g* (N = 20).

The traveled distance supports the loss in the migration already noticed: in CTRL conditions cells travel up to about (381 ± 42) μm, while in presence of 1*g* it amounts to (279 ± 40) μm for 1 μM-condition and (211 ± 24) μm for the 2 μM-condition (**Fig. 107**).

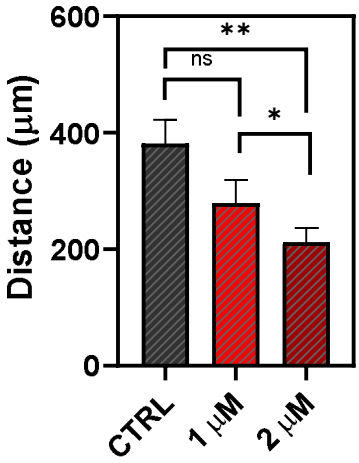

Fig. 107 Traveled distance of U87MG cells treated with different concentrations of 1*g* (N = 20).

Even cell mean speed is lowered in presence of 1*g* (**Fig. 108**): from the (0.54 ± 0.04) μm/min of the control conditions the speed slightly drops at (0.44 ± 0.02) and (0.34 ± 0.01) μm/min of the 1 μM- and 2 μM-conditions.

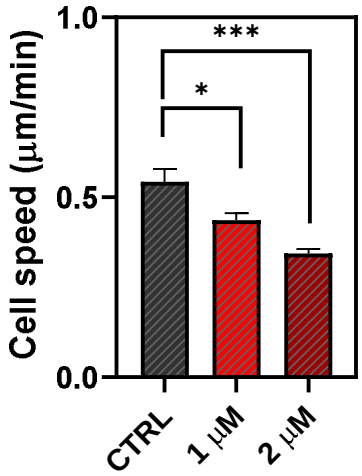

Fig. 108 Mean cell speed of U87MG cells treated with different concentrations of 1*g* (N = 20).

Finally, the *D* coefficient sums up the aspects previously discussed, decreasing from the starting value for the CTRL cells (approx. 4.2 μm^2/min) to 3.0 and 1.9 μm^2/min for the 1 μM and 2 μM 1*g* respectively (**Fig. 109**).

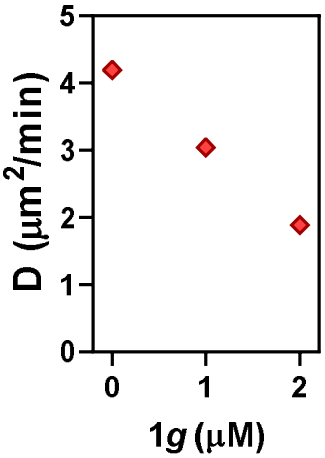

Fig. 109 Mean cell speed of U87MG cells treated with different concentrations of 1*g*.

Effects on cell duplication

The 1*g* treatment is already known to affect the process of cell mitosis, in particular hindering the G_2/M transition, interfering with the dynamic of assembly of the mitotic spindle and resulting in cells unable to divide [9], [10], [In preparation].

From the time-lapse imaging, an effect on cell duplication is rather evident just by comparing the number of cells present at $t = 0$ vs $t = 24$ h (**Fig. 110**) even though cell shape remains quite unaltered.

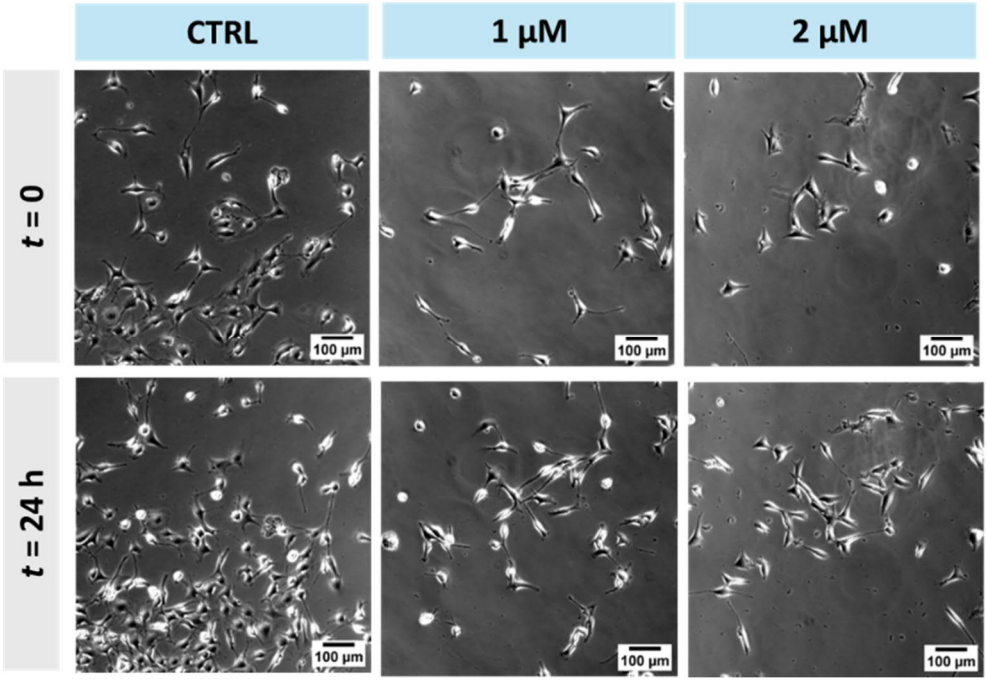

Fig. 110 Pictures at the optical microscope (10x magnification) of U87MG in control condition, treated with 1 µM and 2 µM 1*g* at $t = 0$ and $t = 24$ h.

The duplication time, intended as the time elapsed from the frame in which cells became round to the frame at which two daughter cells can be clearly identified, and started separating, was hence evaluated (**Fig. 111**). The delay in cytokinesis was found to be dose-dependent, but statistically significant only for the 2 µM case. In particular, $\Delta t_{duplication}$ was found to be (16 ± 3) min for the CTRL conditions, (38 ± 5) and (54 ± 4) min for the 1 µM and 2 µM treatments respectively.

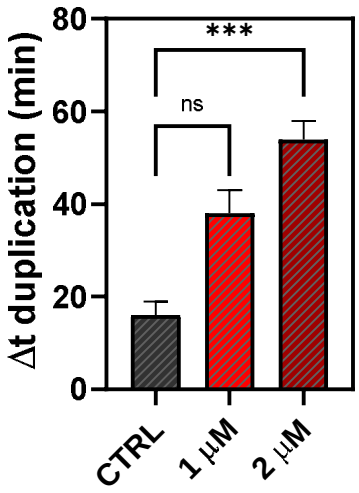

Fig. 111 Duplication time for U87MG cells treated with different concentrations of 1*g* (N = 20).

5.1.2 Wound healing assays

During wound healing assays the effect of the 1*g* treatment is quite evident, as it can be observed in **Fig. 112**, in which images of the cell fronts in different conditions, at the beginning and at the end of the time-lapse imaging, are placed side-by-side.

The remaining wound gap is surely thinner in CTRL conditions, where cells also appear with an elongated and well spread shape. After 24 h of 1*g* treatment the closed gap between cell fronts is small and cells appearance is very different: most of them are in fact round, probably stuck in the G_2/M phase, continuously trying without success to complete the duplication process.

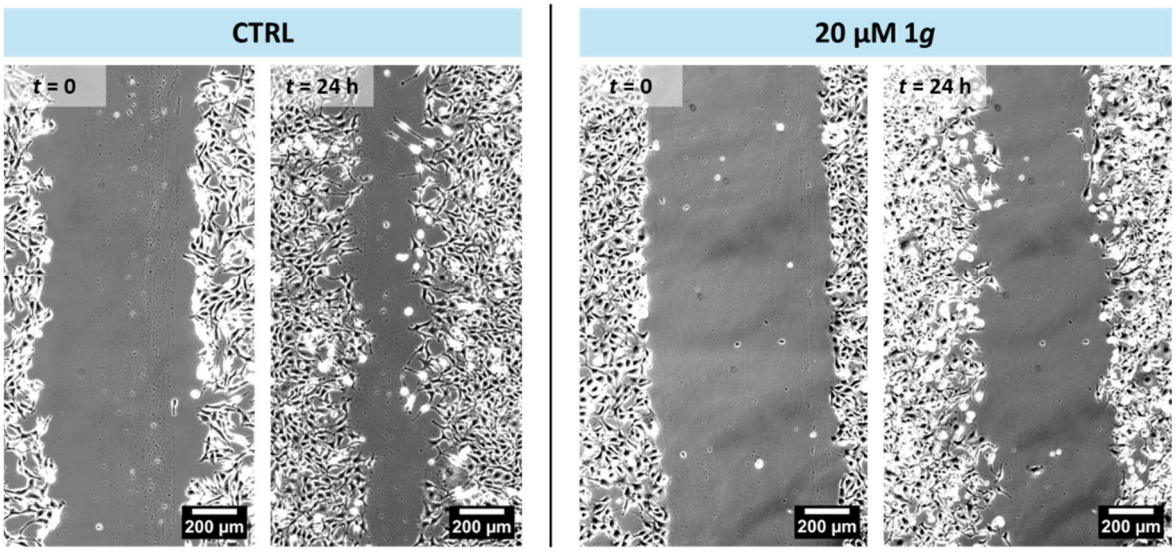

Fig. 112 Images at the optical microscope (10x) of the wound healing assay of U87MG cells in CTRL conditions (left) and 20 µM 1*g* (right) at *t* = 0 and at *t* = 24 h.

The different gap closure is further explored in **Fig. 113**, where the progress of the wound area over time is presented. As mentioned before, treated cells tend to slow down their migration resulting in a larger uncovered wound area.

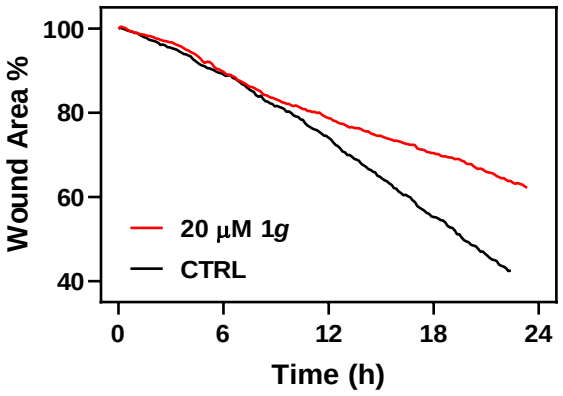

Fig. 113 Evolution of the Wound Area (%) in Wound Healing assays of U87MG in control conditions (black line) and with 20 µM 1*g* treatment (red line).

At the end of the experiment, after 24 hours, the final wound repair was quantified and the recovered area was found to amount to (63 ± 2) % in CTRL conditions *versus* (36 ± 7) % for the 1*g*-treated condition (**Fig. 114**).

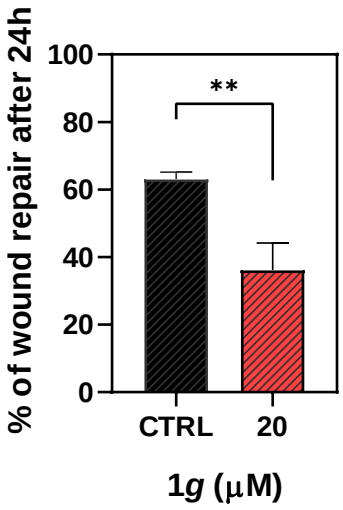

Fig. 114 Percentage of wound repair after 24 h of collective migration (N = 3).

The mean front displacement accounts for the advancement of the cell leaflet border over time. In **Fig. 115a** the front progression of the tested conditions is displayed. While the CTRL condition progresses farther it also shows a scattered aspect, which could be due to cells at the front elongating prior to moving on. The 1*g*-treated condition shows a slower advancement and a more packed aspect, a probable effect of the smoothing of the front borders due to cells rounding. The aspect of the front of advancing cells is also studied by the complexity ratio, *L/D*, (**Fig. 115b**), with *L* being the actual length of the contour of the front and *D* the dimension of the image. Over time, the *L/D* ratios progressively increase, describing fronts which get rougher: in CTRL conditions this can be explained by cells individually detaching from the front while in the 1*g*-treated case it is caused by holes created by cells retracting to round up.

a) b)

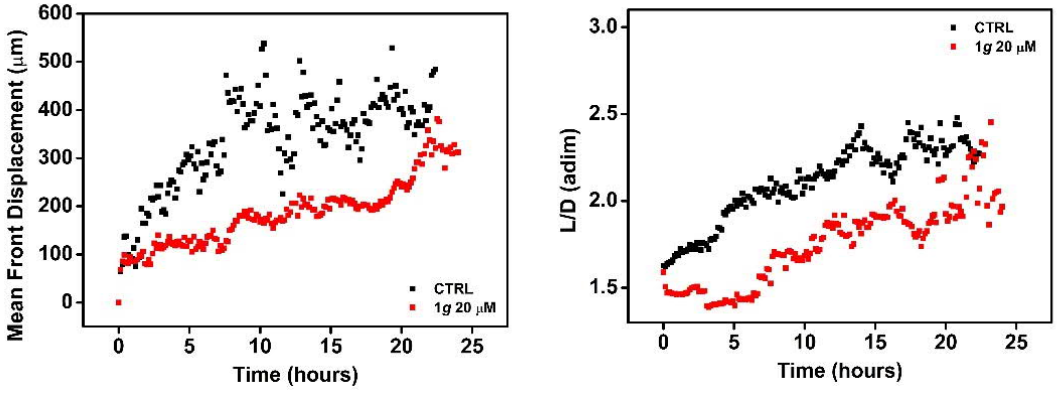

Fig. 115 Evolution over time of the mean front displacement (a) and of the complexity ratio *L/D* (b).

Fig. 116 reports the distribution of the speed of the cell fronts, extracted from the comparison of the initial and the last frames of the time-lapse sequences. In CTRL conditions cell fronts move within a wide range of speed, with its mean value at (14 ± 5) μm/h. Inversely, the 1*g*-treated samples show a narrower and slower speed distribution, with mean value equal to (8 ± 3) μm/h.

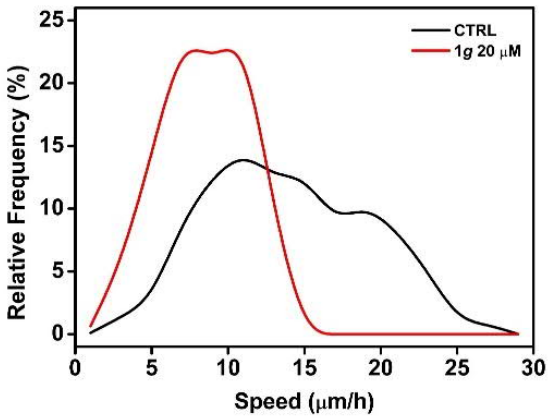

Fig. 116 Frequency distribution of the cell fronts speed.

Finally, the angular dispersion of the direction of the front progression is shown in **Fig. 117**. This parameter can summarize the efficacy of cell tissues at closing the gap, moving altogether with a collective migration process. The mean angle for the collective migration is (0 ± 30) ° for CTRL cells, and (0 ± 38) ° for 1*g*-treated cells. Close-to-zero angle values are expected, since cell fronts move perpendicularly to their edge and are not particularly relevant. On the other hand, the standard deviation values, which account for data dispersion, can be interpreted as loss of migration efficacy upon treatment and a tendency of cells to acquire a random-walk-like migration. This loss of "compactness" in collective migration can be interpreted as a reduced cooperation among cells and a diminished invasive attitude of the cell sheets.

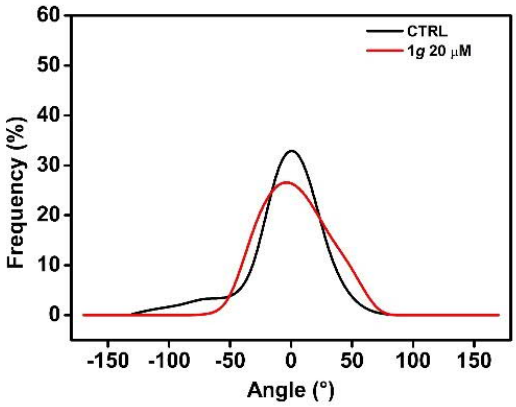

Fig. 117 Frequency distribution of the cell fronts angle.

5.1.3 Conclusions

This brief overview of the effects of the treatment with 1*g* on U87MG cells establishes that low-concentration treatments are effective in reducing single-cell migration and cell speed. As demonstrated in more extensive studies on the effect of 1*g* on this cell type, this drug is able to strongly decrease the area explored by these cells in 2D free migration. However, unlike at higher concentrations, low concentrations of 1*g* do not affect cell shape while reducing migration. This evidence suggests that 1*g* intrinsically affects cell migration, even when not losing cell polarity. The drug not only inhibits cell duplication but also induces a “frozen” state in which cells struggle to complete cytokinesis and are hindered in migration as well. Wound healing assays assert that collective migration is also impaired in presence of 1*g*: front speed, mean front displacement and the closure of the wound area over time all show a poorer performance compared to control cells. The angular dispersion of the front movement direction suggests an increment in cells that tend to behave as individual migrating entities, moving in a pattern resembling a random walk process.

5.2 Cell migration in a confined quasi-3D environment

Samples characterization

Cells cultured on the μ-patterned PDMS appear drastically different from those cultured on a flat PDMS surface (**Fig. 118a, b**). Cell and nuclear morphology are quite affected by the confined environment: cytoplasm protrusions try to scan the surrounding inter-pillar space, aligning along "corridors" in the μ-pattern (**Fig. 118c**) while the nuclei are often cross-shaped as a result of their trapping (**Fig. 118d, e**).

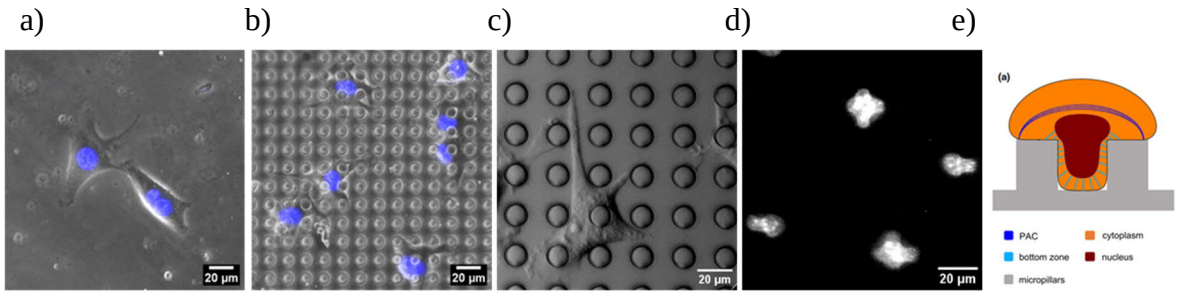

Fig. 118 Hoechst-stained U87MG cells cultured on flat (a) and μ-patterned (b) PDMS. Details of cytoplasm protrusions (c) and some nuclei (d). Schematic representation (e) of the nucleus entrapped between μ-pillars and pulled by actin fibers in contact with the lateral surface of the pillars, from: [90].

While nuclei position themselves at the bottom of the pattern, in between pillars, exploiting inter-pillar spacing, protrusions are able to move around more freely. This was clear studying samples fixed with glutaraldehyde and dehydrated with ethanol and observed at the Scanning Electron Microscope. Micrographs in **Fig. 119** show, in fact, that cell protrusions can spread wherever they prefer, tightly embracing pillars or grasping them from the top.

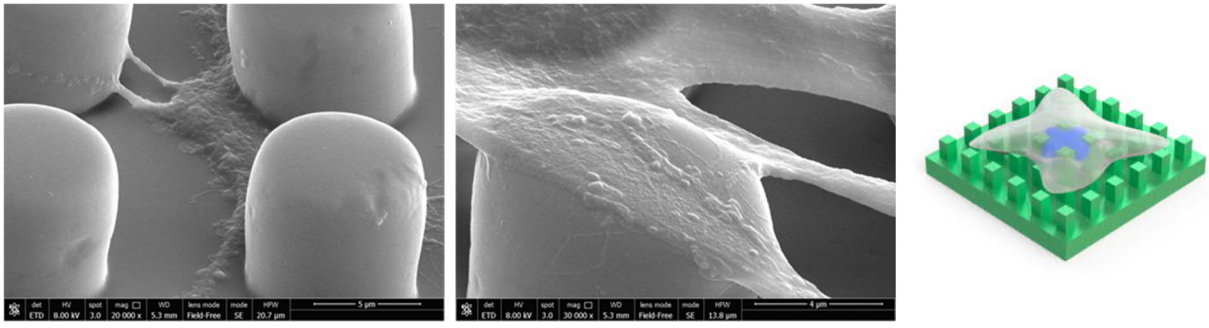

Fig. 119 On the left, SEM micrographs of U87MG cell cultured on μ-patterned PDMS. On the right, a picture from [91] of the possible configuration adopted by cells cultured on the pillars.

Single-cell migration

Below, in **Fig. 120**, the origin-normalized plots of the trajectories swept by the cells highlight the behavior of control cells and cells treated with blebbistatin (a drug blocking the activity of myosin II), showing a bimodal response to blebbistatin concentration. At low concentrations an enlargement of the "wind-rose" occurs, which is then followed, at higher concentrations, by a contraction. In addition to this, in the plot acquired for cells on the micropillars, a tendency to move perpendicularly along pattern corridors is understandably present. Moreover, some unexpectedly long trajectories were noticed and in **Fig. 120** they are pointed at by black arrows.

A high magnification of the plots (**Fig. 121**) shows a smoothing effect in cells trajectory due to blebbistatin up to 10-15 μM, as if the pharmacological treatment made cell movement "more fluid". At 20 μM the effect wears out.

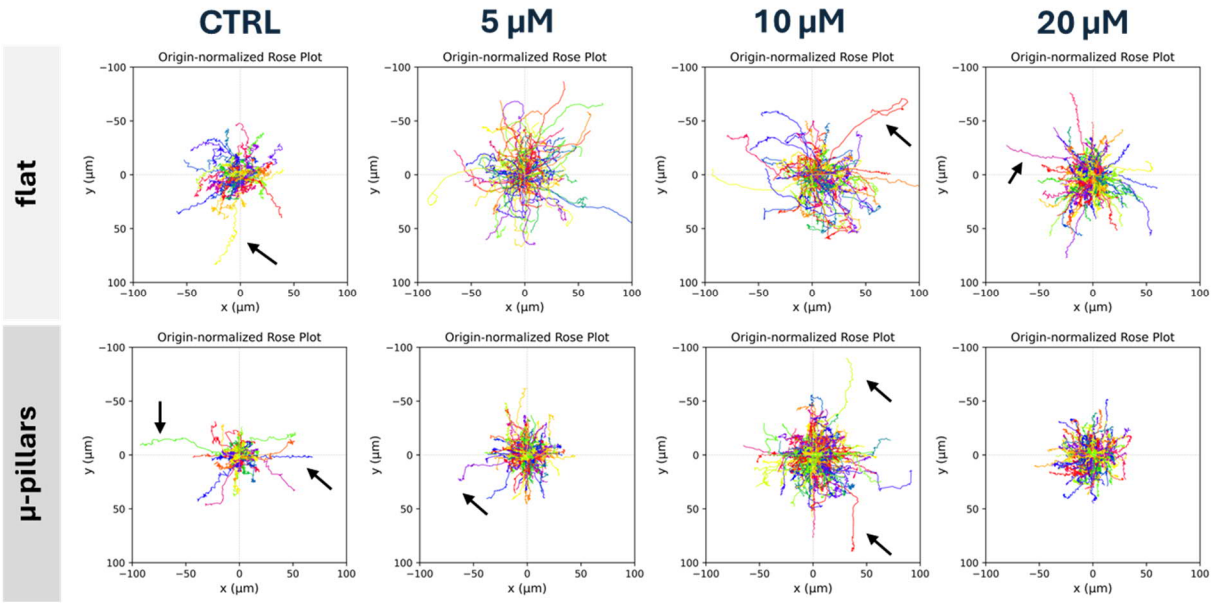

Fig. 120 Origin-normalized plots with the cell trajectories run in 6 h of experiment. Black arrows point at some cells whose trajectory was unexpectedly long.

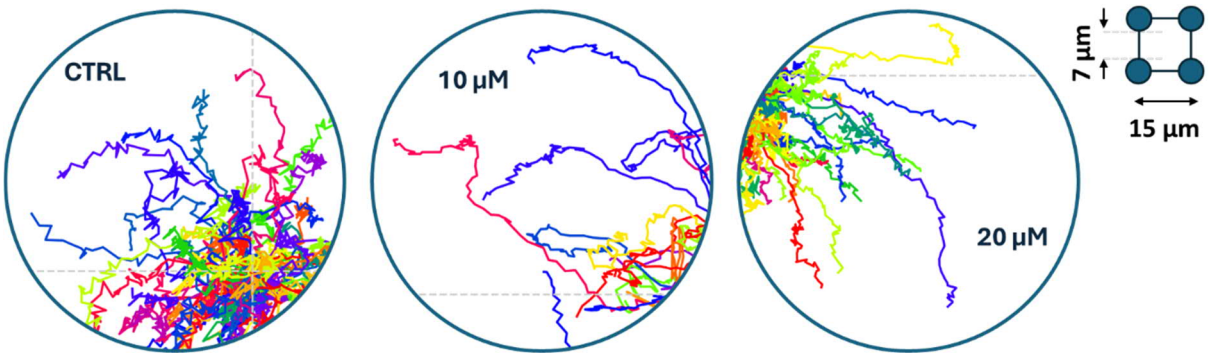

Fig. 121 Detail of the smoothing effect of blebbistatin (zooms of plots from **Fig. 120**).

In **Fig. 122** the MSD(t) curves for every experimental condition are plotted. Starting by comparing CTRL cells on flat *versus* patterned PDMS, an effect due to the sole presence of the micropillars is already detectable. The µ-pattern slightly hinders cell migration as a probable consequence of the entrapment of the nucleus. Treatment with increasing concentrations of blebbistatin causes, for cells in both topological conditions, a bimodal response in the MSD over time with a maximum in the explored area for a concentration of 10 µM. Nonetheless, cells on the µ-pattern still preserve an impaired MSD.

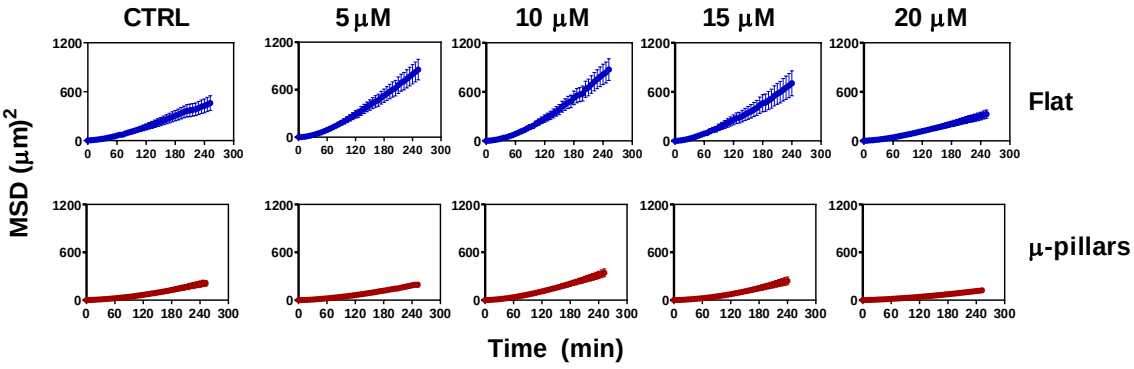

Fig. 122 MSD(t) plots of U87MG cells cultured on flat (top row) and µ-patterned (bottom row) PDMS (N = 100).

The same observations still hold when discussing the diffusion coefficient *D* which, for 10 µM blebbistatin, reaches the respective maximum values amounting to (1.2 ± 0.2) and (0.6 ± 0.1) µm^2/min for the flat and micropillared conditions (**Fig. 123**), respectively.

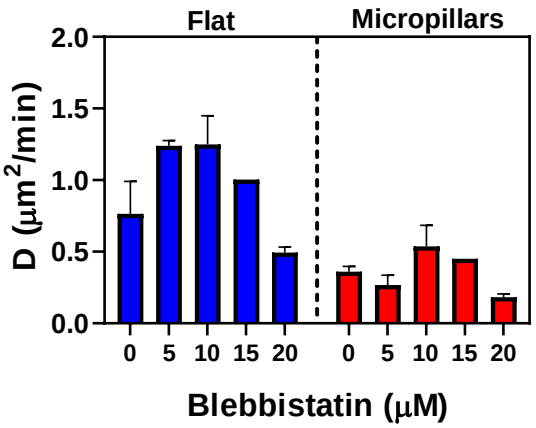

Fig. 123 Coefficient of diffusion *D* of U87MG cells cultured on flat and μ-patterned PDMS (N = 3).

Taking into account other migration parameters such as mean speed, distance and displacement, we can understand that the differences observed for the MSD behavior are not due to an enhanced speed but rather to an improved directionality in migration. In fact, comparing the different plots in **Fig. 124**, a decrease in cell speed can be noted from panel (**a**), which could be the result of a loss in functional actin fibers in the cells due to blebbistatin. From panel (**b**), one could see that the traveled distance is almost constant, which could be interpreted as an index of preserved cell motility. Panel (**c**) depicts the vectorial displacement of the U87MG cells and shows, interestingly, that for ~10 μM blebbistatin cells move farther in both topological scenarios.

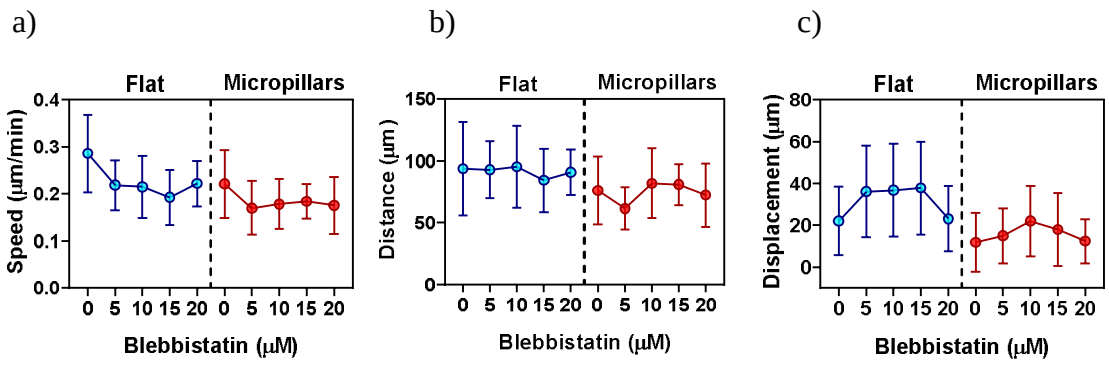

Fig. 124 Speed (a), distance (b) and displacement (c) of U87MG cells treated with different concentrations of blebbistatin (N = 100).

Delving into the displacement achieved by the cells, the frequency distribution plots reveal that different cell "populations", from a behavioral point of view, are present at work (**Fig. 125**, **Fig. 126**). This heterogeneity in the phenotype of the cells of glioblastoma multiforme is an aspect already reported in literature and characteristic of the tumor [92], [93].

Based on the modulus of the displacement $\vec{s}$, three cell populations were proposed:

- for $|\vec{s}|$ values in the 0 – 10 μm range → *twirl* cells
- for $|\vec{s}|$ values in the 10 – 30 μm range → *short* cells
- finally, for $|\vec{s}|$ values > 30 μm → *long* cells

Twirl cells do not move very far but rather move back and forth in the whereabouts of their initial position; conversely, short and long cells travel farther.

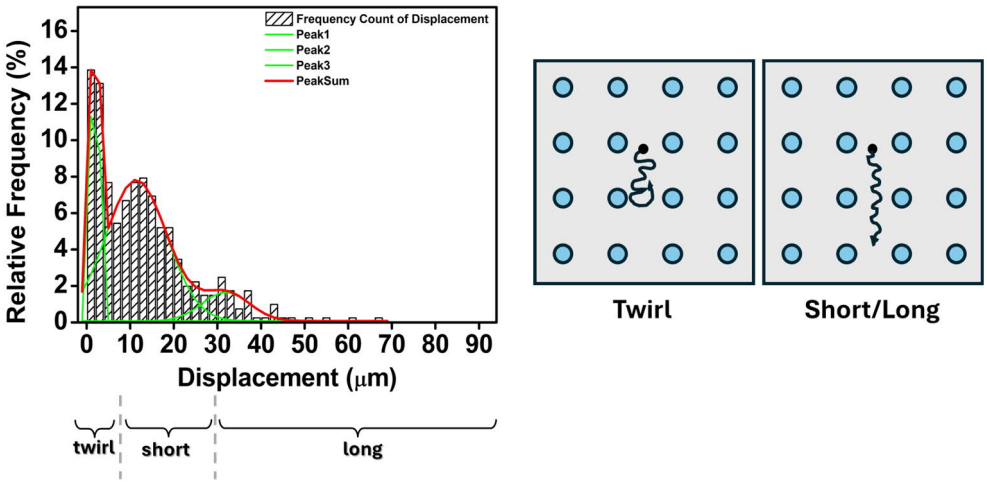

Fig. 125 On the left, frequency distribution plot of the displacement in a sample of U87MG cells cultured on μ-patterned PDMS. On the right, schematic representation of the trajectory of twirl and short/long cells.

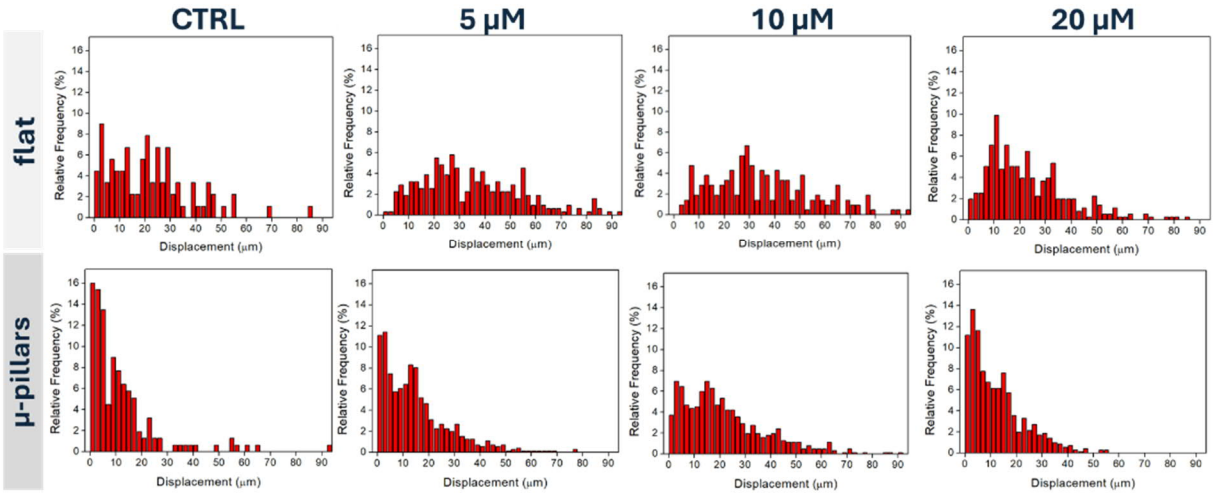

Fig. 126 Frequency distribution plots of the displacement of U87MG in the different experimental conditions (N = 100).

Bearing this displacement-based classification in mind, the distribution into twirl, short and long cells varies with the concentration of blebbistatin and is affected by the substrate topography (**Fig. 127a**). On flat surfaces, most cells belong to the farther migratory types, short and long, contributing to a better performance of flat MSD curves with respect to µ-pillared MSD curves. Accordingly, these second set of curves are the result of a predominance of twirl and short cells, lowering the overall migration capability. Plotting the long-to-short ratio (**Fig. 127b**) an index of propension towards transitioning to the long cell type is obtained. The ratio shows that the transition is more marked onto the flat surfaces, but, in both cases, it is more accentuated at 10-15 µM and drops at 20 µM blebbistatin.

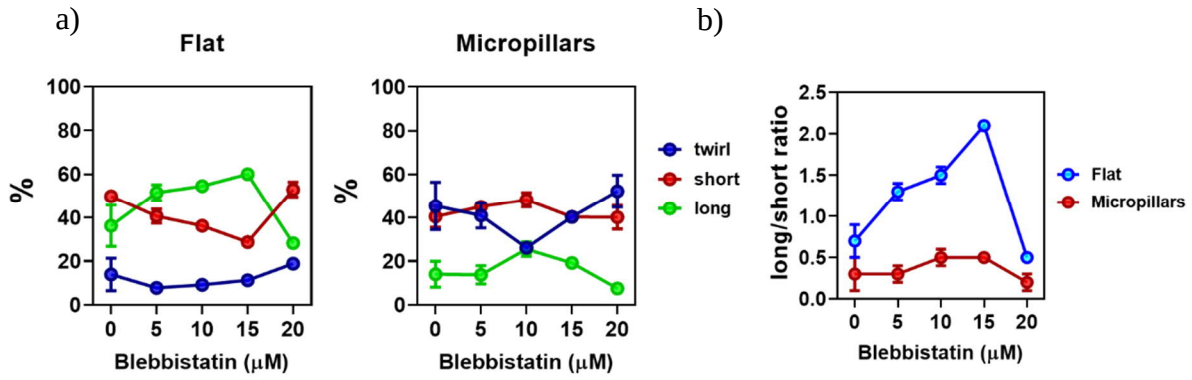

Fig. 127 (a) Distribution into the different populations of U87MG cells. (b) Long-to-short ratio in different experimental conditions (N = 3).

Nuclei appearance

In addition to cell migration, the effect of confinement in nuclear area and shape were evaluated, analyzing the signal of the Hoechst-stained nuclei. In **Fig. 128** the nuclei area over time is plotted for both flat and μ-pillared surfaces. Comparing the CTRL curves (black lines) obtained for flat and μ-pillared samples in the absence of blebbistatin, a loss in nuclear area occurs.

Nuclei in the patterned environment, in fact, project on the *x*-*y* plane an area that appears about 20% smaller. This loss in projected nuclear area could be explained with an adjustment of cell nuclei in the inter-pillar spacing and it is probably followed by a partial vertical re-location of the nuclear matter in the *z* direction.

Treating cells with blebbistatin provokes a gentle decrease in nuclei area over the first hours of drug application; after some time, areas reach a constant value which is very similar between flat and μ-pillared cells (red and blue lines). The projected area of nuclei of blebbistatin-treated cells has been documented to reduce upon treatment, as a consequence of the increment of the height of the nuclei in the *x*-*z* plane [94]. Apparently, the differences in non-treated conditions caused by the μ-pattern are leveled when blebbistatin is added; in fact, once treated, cells on both flat and patterned surfaces exhibit similar areas.

This effect can be explained recalling the role that perinuclear F-actin plays in shaping the cell nucleus [95]; apparently, the effect blebbistatin enacts in cells does not depend on the different topological conditions.

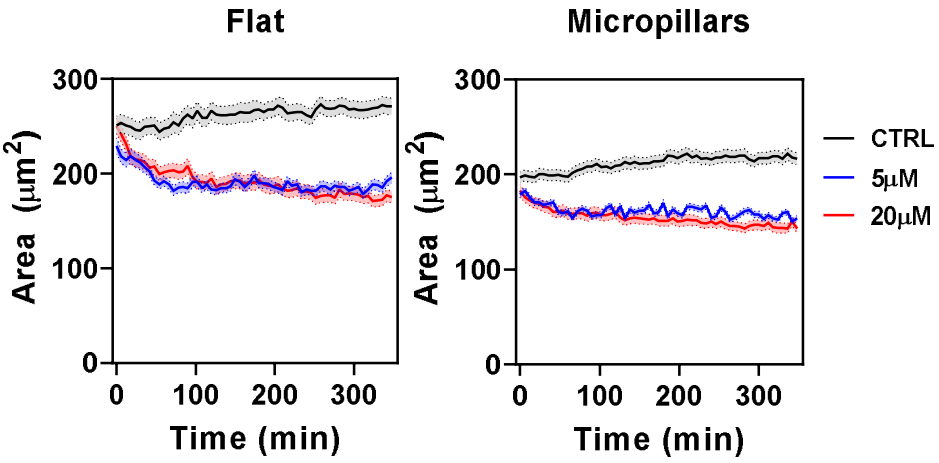

Fig. 128 Nuclear area over time of U87MG treated with blebbistatin (N = 100).

The *b/a* ratio from the elliptical fit of the nuclei shape reveals that blebbistatin treatment does not alter significantly the cell shape over time, but it rather remarks on the effect of spatial confinement (**Fig. 129**). Regardless of blebbistatin, cells onto flat PDMS appear with an almost perfect round shape which is retained over time; conversely, cells in the μ-patterned substrate appear slightly more elliptical.

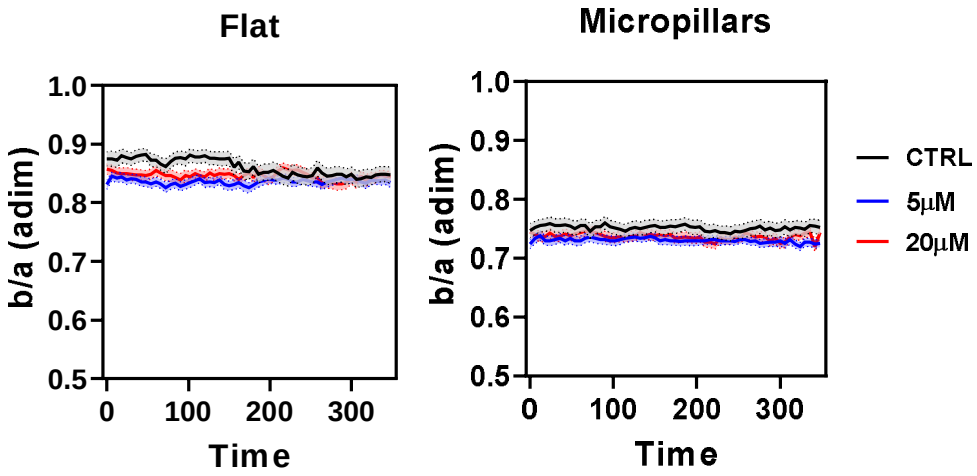

Fig. 129 Shape factor *b/a* over time of U87MG treated with blebbistatin (N = 100).

Cell viability to blebbistatin

To rule out the possibility of any influence of blebbistatin on cell viability, a vitality test (Cell Counting Kit-8, Sigma Aldrich) with U87MG cells treated at different concentrations of blebbistatin was performed. Viability was assessed after 6 h of treatment, to cover the whole duration of the imaging experiments. In **Fig. 130** the results of the CCK test prove that no significant loss of viability is observed even for blebbistatin concentrations up to 100 μM.

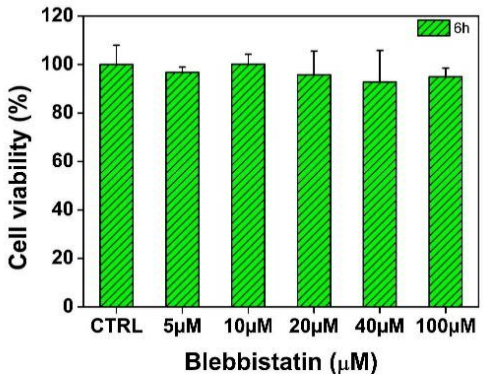

Fig. 130 Cell viability after 6 h of treatment with blebbistatin at different concentrations (N = 3).

5.2.1 Conclusions

The results presented here suggest that micropatterned substrates could provide a viable alternative to complex three-dimensional substrates. The confinement provided by micropillars challenges cells to overcome obstacles and squeeze their nuclei (up to 20%) in order to slip along corridors in the pattern. The nuclear compression provided by the μ-pattern geometry could be exploited in future applications to study the process of nuclear mechanosensing. Cells use their nuclei as an inner sense to measure the extent of the spatial confinement they are subjected to [96], leading to shifts in cell migration modes driven by spatial availability. Confinement in the μ-patterned substrate does not significantly induce variations in cell speed and displacement, but rather enhances directionality in single-cell migration. This latter effect is quite reasonable, since cells are keen to form pseudopodia along corridors. From a behavioral point of view, three distinct cell populations are identified based on their ability to sustain either long or short displacements during locomotion, as opposed to oscillating back and forth (twirl) with limited forward movement. Cell distribution into these different populations is found to be directly affected by the μ-patterning.

To validate the effect of the proposed μ-patterned substrates, we treated cells with blebbistatin, as data from 3D experiments with blebbistatin-treated glioma cells migrating through Transwell pores (diam. ~ 8 μm) were already available in the literature [63]. Treatment with blebbistatin induced different responses in cells adherent to the flat and to the μ-pillared surfaces, further highlighting the distinctions between the two environments. In particular, the increase in MSD recorded for blebbistatin-treated cells in the μ-pillared substrate might support and partially align with the findings of Inukai et al. [63], confirming a resemblance between 7 μm-spaced μ-pillars and 8 μm-in-diameter Transwell pores. A possible explanation for the increased displacement upon blebbistatin treatment may lie in cell stiffness. AFM studies point out that blebbistatin not only lowers the stiffness of the cytoskeleton by disrupting its contractile fibers [97], but that the stiffness of the nucleus is affected as well [94]. In [94], the nuclei of osteosarcoma U2OS cells were found to soften as a consequence of the treatment with blebbistatin, attributing this effect to the homeostatic role of perinuclear F-actin in maintaining nuclear stiffness through its interaction with lamin A.

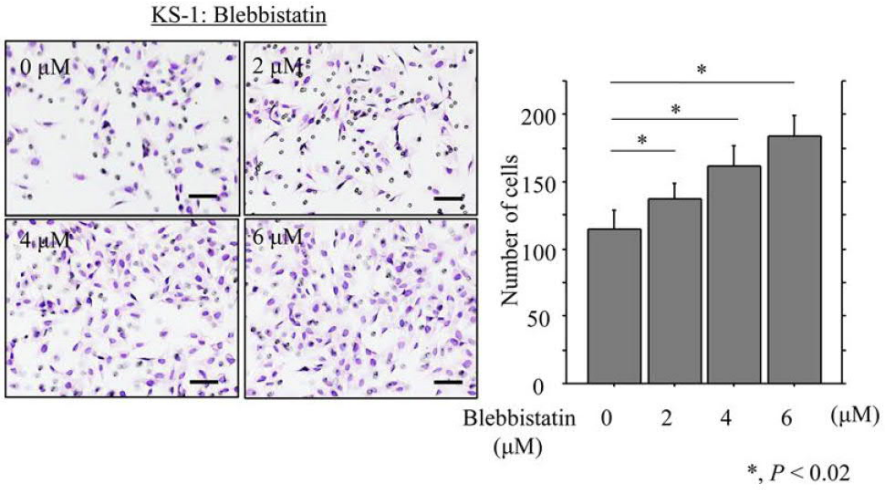

Fig. 131 Results of migration across 3D Transwell pores of glioma cells treated with blebbistatin, from [63].

In the next page, in **Fig. 132**, a schematic summary of the effects induced by µ-patterning and blebbistatin treatment on confined U87MG cells is presented.

Fig. 132 Schematic representation of the effect of µ-patterning and spatial confinement on cell migration.

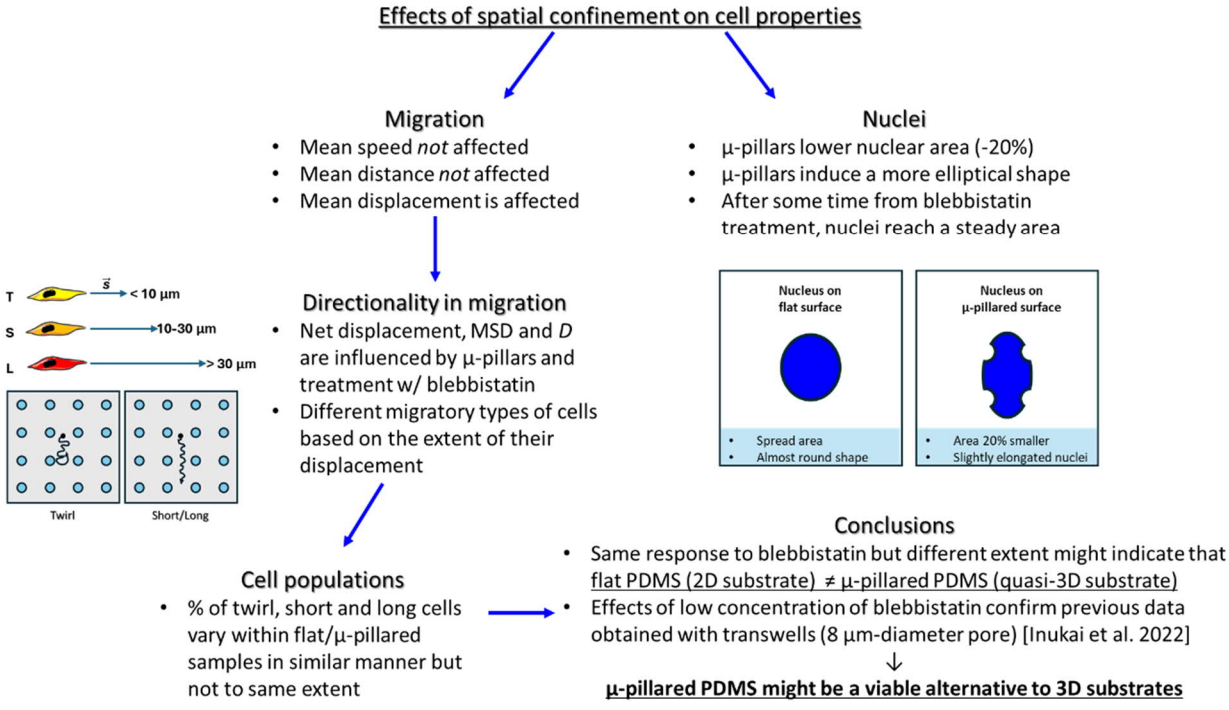

Chapter 6 – Results of the experiments with HCT166

This Chapter focuses on the results achieved from wound healing experiments with HCT166 cells overexpressing NF-YAs/NF-YAl isoforms. These results have been included in the publication by Rigillo et al. [65].

6.1 Wound healing experiments

As previously described in [68] the two NF-YA isoforms cause differences in cell phenotype. In **Fig. 133** the fronts of empty (control cells), NF-YAl and NF-YAs cells after 24 h of wound healing are displayed. From the comparison of these pictures, it is quite evident that each cell type deeply influences the behavior and the aspect of the cell front.

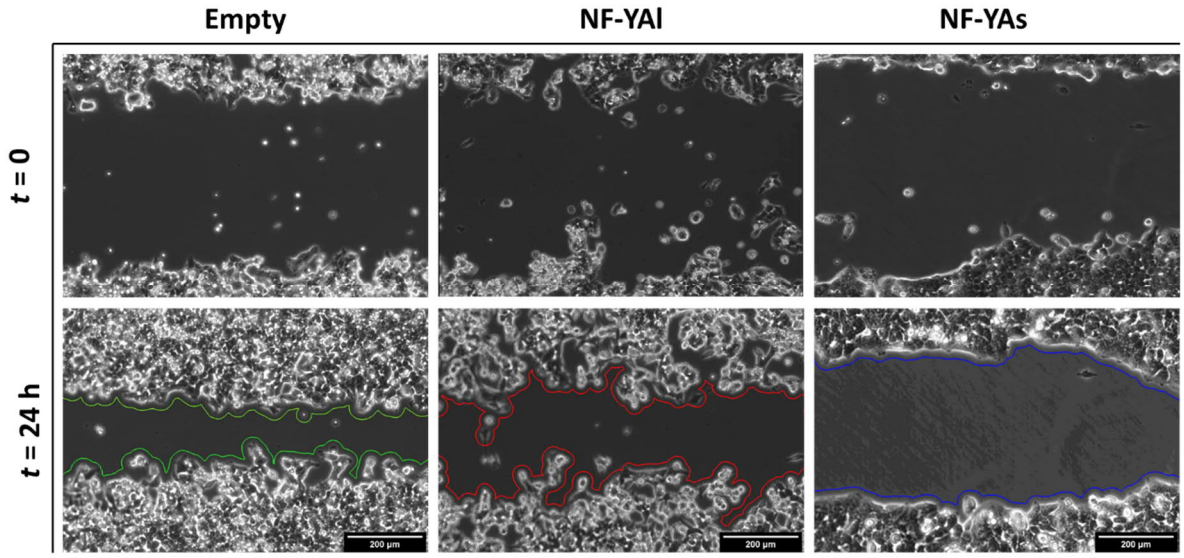

Fig. 133 Cell fronts of empty, NF-YAl and NF-YAs HCT166 cells.

From the detection of the cell fronts over time, the mean front displacement and the complexity ratio *L/D* were extracted and plotted in **Fig. 134**. From these plots we can deduce that the NF-YAl cells are characterized by a quicker front displacement and by a jagged front appearance with high *L/D* values. NF-YAs cells move with a vaguely lower speed which still is greater than the control conditions and present a similar cell front complexity, with low values of *L/D*.

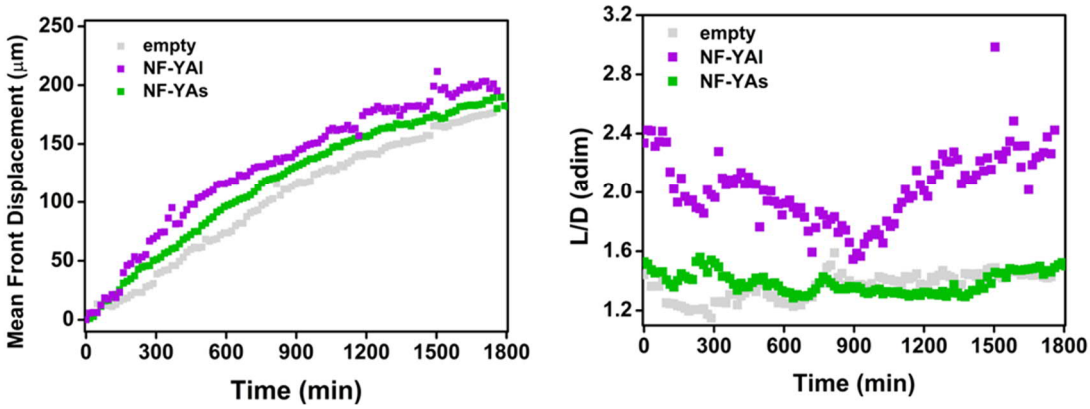

Fig. 134 Mean front displacement (left) and front complexity ratio (right) of HCT166 cells.

In NF-YAl conditions, some individual cells with a different morphology were spotted both in collective migration assays (**Fig. 135a**) and in sub-confluent cultures, as the fluorescence image in **Fig. 135b** portrays, where a cell with a large lamellipodium is evident. From the wound closure time-lapse movies, we see that these amoeboid-like cells move faster (see **Fig. 135b**, central panel) than the others and, once they reach the cell front, they start dragging other cells forward. Conversely, NF-YAs cells tend to move more cohesively, in a collective manner, as the absence of amoeboid-like cells and a compact PIV output both prove.

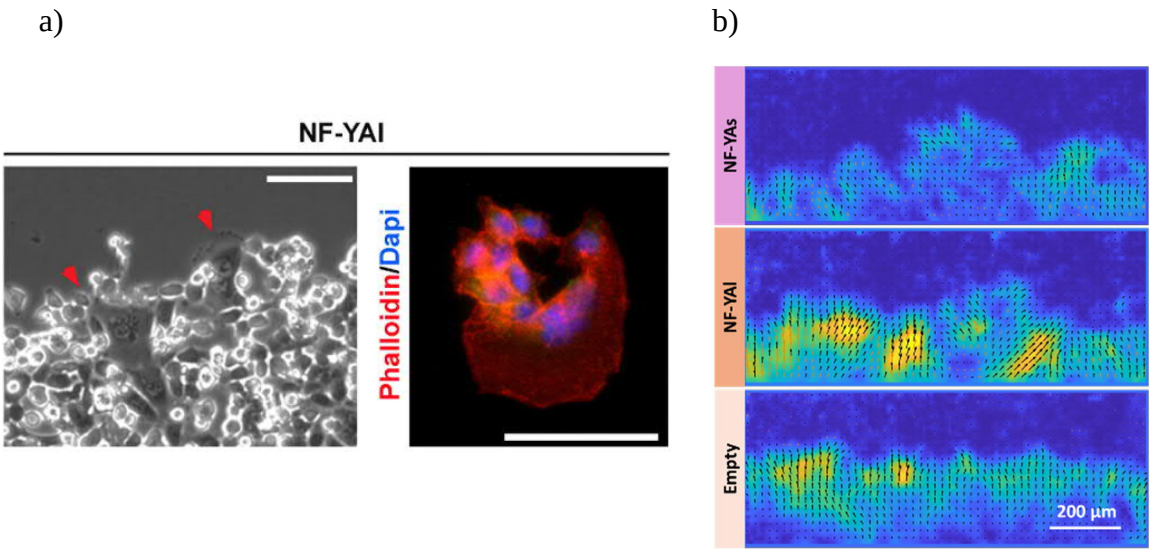

Fig. 135 (a) Close-up of the front of NF-YAl cells; red arrows highlight amoeboid-like cells. At the side a fluorescent image of non-confluent NF-YAl cells. Scale bar = 50 µm. (b) PIV analysis performed on cells fronts. The false-color scale represents the magnitude of the speed vectors represented by arrows: dark blue = low speed, yellow = fast speed.

This different degree of “cohesion” in NF-YAs and NF-YAl can be observed also from the interpretation of the frequency distribution plots of the front speed and the angle of front progression, depicted in **Fig. 136a**, **b** respectively.

Plots about NF-YAs cells show a rather uniform speed distribution, with a mean value that amounts to ~2 μm/h, and a narrow angle distribution. NF-YAl cells, on the other hand, display a higher speed, with a peak centered at ~4 μm/h and a shoulder at ~5 μm/h. From **Fig. 136b** we notice that also the angle distribution is less homogeneous, with an uneven and large peak.

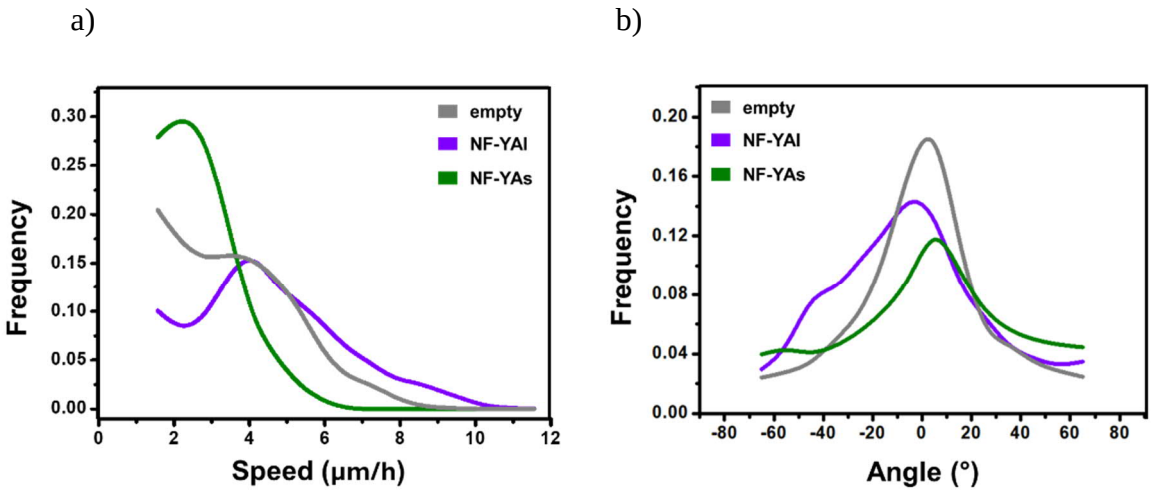

Fig. 136 Frequency distribution plots of the front speed (a) and angle (b).

6.2 Multicellular spheroids

In **Fig. 137** images from the time-lapse acquisition of multicellular spheroids of HCT166 overexpressing cells, after 0, 24 and 48 h, are shown. From the comparison of the different cell types, the effect of the NF-YA isoform is rather evident. Empty and NF-YAs cells exhibit “wetting” of the substrate, with cells that adhere to it, although the spreading of the cells is quite different in the two conditions. Notably, NF-YAs cells present a very large area covered by the adherent cells, constituting a cell monolayer. On the contrary, NF-YAl cells tend not to wet the surface, but rather engage in single-cell migration, avoid cell-cell adhesion and leave the spheroid body.

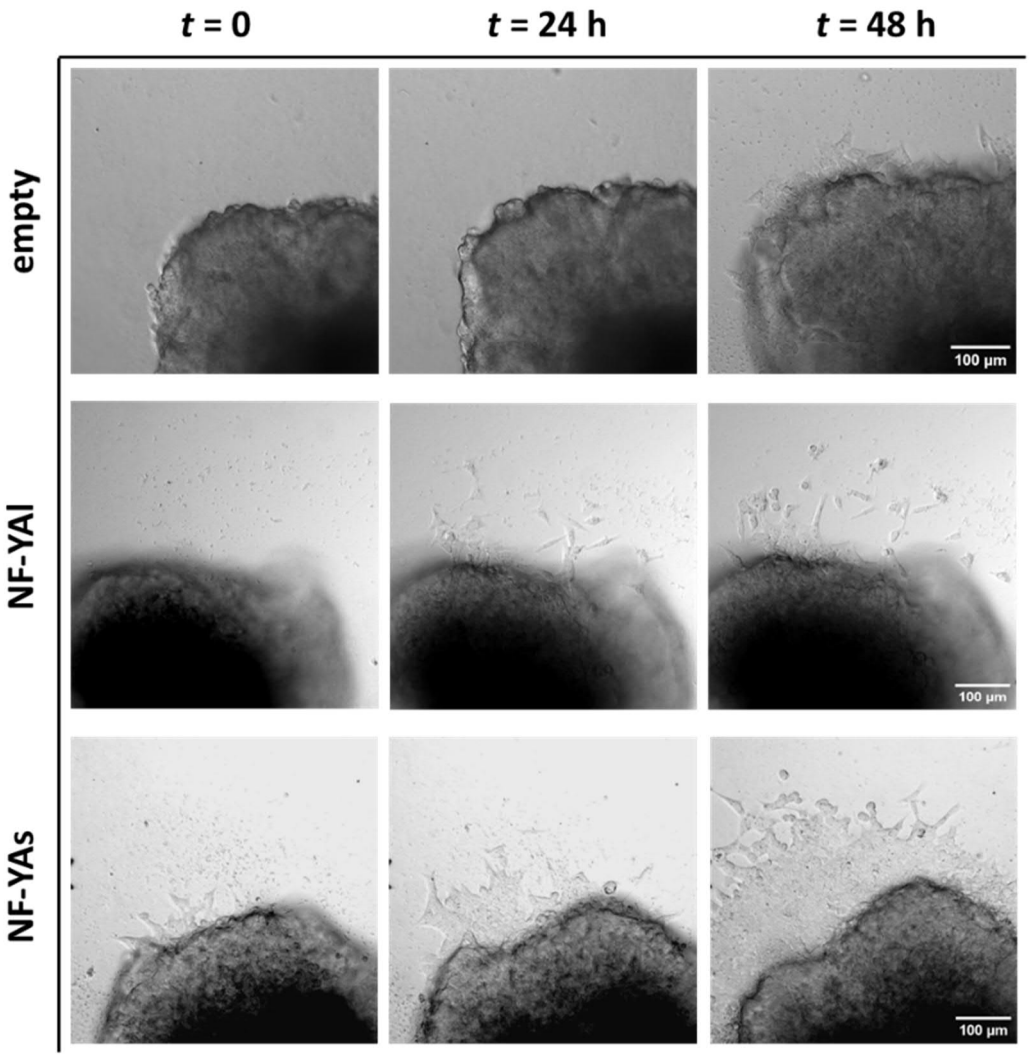

Fig. 137 Snapshots from the time-lapse sequences acquired by optical microscopy of HCT166 spheroids.

6.3 Conclusions

The previous findings confirm that the two isoforms of the transcription factor subunit NF-YA induce cells to behave differently in the process of collective migration, displaying different phenotypes. Wound healing assays show, in fact, that the aspect of cell fronts and their evolution over time are strongly affected by cell type. NF-YAs-overexpressing cells migrate preferentially as a cohesive unit, in an orderly manner and with a uniform speed. In contrast, NF-YAl-overexpressing cells tend, at least partially, to engage in individual cell migration, exhibiting a less ordered motion and a non-uniform speed distribution.

The observation of spheroids of HCT166 cells overexpressing each NF-YA isoform confirms its strong impact on collective cells behavior in a 3D environment. NF-YAs cells act as invasive aggregates, quickly wetting the substrate surface and forming cell monolayers still connected

to the basis of the spheroid. Conversely, NF-YAl cells avoid wetting the substrate and detach from the spheroid body, initiating migration as individuals and rather behaving as metastatic cells.

These findings suggest that the isoforms of the NF-YA transcription factor subunit strongly modulate HCT166 cells in their migration. The isoforms may serve as potential candidates to establish a molecular signature useful in characterizing the stage of tumor progression: while the NF-YAs isoform appears to enhance collective migration, acting as an index of invasive growth, the NF-YAl isoform is associated to a likely metastatic behavior.

In the next page, in **Fig. 138**, a schematic summary of the main findings relative to NF-YAs/NF-YAl HCT166 cells is presented.

Fig. 138 Summary of the results from collective migration experiments of HCT166 overexpressing cells.

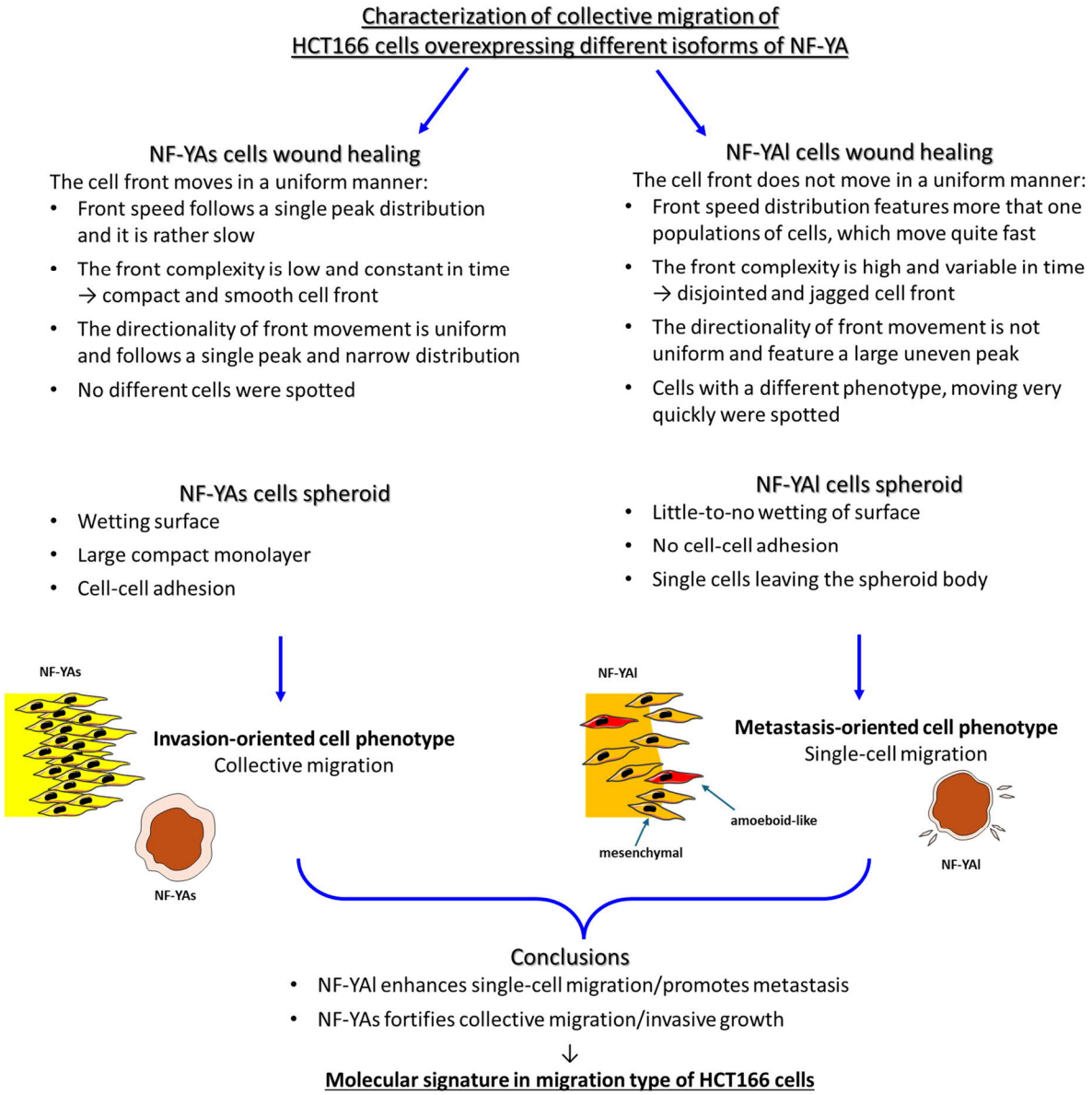

Final remarks

This Thesis aimed to explore different applications of mechanobiology and to prove its value to the scientific community. It presented a variety of approaches and techniques used to investigate physiological and pathological conditions which are relevant to medicine, with particular emphasis on the adaptation of cells to mechanical stimuli.

Specifically, this Thesis covered the following main points:

(i) A thorough presentation and calibration of cell stretchers developed by our group and exploited for time-lapse imaging of cyclically stretched cells was presented. Following that, a preliminary characterization of the response of human cardiac fibroblasts cultured on PDMS to uniaxial and biaxial cyclic stretching was reported. Cell response to stretching stimuli differing for waveform, frequency and direction was evaluated in terms of migration, orientation, alignment of stress fibers and preservation of focal adhesions. These initial results lay the basis for further experiments with increasingly complex mechanical perturbations, facilitating a better characterization of the repair mechanisms and the fibrotic processes in which fibroblasts play a primary role. In particular, the reorientation process of fibroblasts was studied after a period of cell adaptation to a periodic stretching signal, simulating an injury.

(ii) A quasi-3D PDMS-based substrate was successfully developed and tested to investigate the migration of glioblastoma cells, serving as an alternative experimental setup to bridge the gap between 2D and 3D models. To validate our "in-between" approach, we analyzed the confined migration of blebbistatin-treated U87MG cells, finding similarities between our results and existing data from Transwell experiments with a pore size close to our inter-pillar spacing.

In support of previously established projects, this Thesis also investigated:

(iii) The response of U87MG cells to '1*g*', a potential novel candidate for pharmacological cancer treatment, was investigated, finding that the drug is effective at hindering single-cell migration, collective migration and significantly reduces tumor invasiveness. The specificity of the drug against glioma cells was also studied.

(iv) The behavior of colon tumor cells (HCT166) overexpressing different isoforms of the NF-Y transcription factor (short and long isoforms, NF-YAs and NF-YAl, respectively) was characterized, demonstrating that these alternative protein versions affect cell

behavior concerning cancer invasiveness and metastatic potential, serving as putative molecular markers for assessing cancer stage.

Publications

Published articles:

- Rigillo, G.; Belluti, S.; Campani, V.; Ragazzini, G.; Ronzio, M.; Miserocchi, G.; Bighi, B.; Cuoghi, L.; Mularoni, V.; Zappavigna, V.; Dolfini, D.; Mercatali, L.; Alessandrini, A.; Imbriano, C. «The NF–Y splicing signature controls hybrid EMT and ECM-related pathways to promote aggressiveness of colon cancer», *Cancer Lett.*, vol. 567, p. 216262, Jul. 2023, doi: 10.1016/j.canlet.2023.216262.

- Bighi, B.; Ragazzini, G.; Gallerani, A.; Mescola, A.; Scagliarini, C.; Zannini, C.; Marcuzzi, M.; Olivi, E.; Cavallini, C.; Tassinari, R.; Bianchi, M.; Corsi, L.; Ventura, C.; Alessandrini, A. «Cell stretching devices integrated with live cell imaging: a powerful approach to study how cells react to mechanical cues», *Prog. Biomed. Eng.*, vol. 7, no. 1, p. 012005, Jan. 2025, doi: 10.1088/2516-1091/ad9699.

Articles under review:

- Ragazzini, G.; Mescola, A.; Tassinari, R.; Gallerani, A.; Zannini, C.; Di Rosa, D.; Cavallini, C.; Marcuzzi, M.; Taglioli, V.; Bighi, B.; Ettari, R.; Zappavigna, V.; Ventura, C.; Alessandrini, A.; Corsi, L. «A novel benzodiazepine-derived molecule interferes with the bio-mechanical properties of glioblastoma-astrocytoma cells altering their proliferation and migration», *Int. J. Mol. Sci.*

Articles in preparation:

- …, Bighi, B. … «Effects of uniaxial and biaxial cyclic stretching on human cardiac fibroblasts»

Poster sessions:

- Bighi, B.; Gallerani, A.; Scagliarini, C.; Ragazzini, G.; Alessandrini, A. «Towards accessible mechanobiology experiments: a DIY cell stretcher with time-lapse imaging» - 7th international symposium “Nanoengineering for Mechanobiology - Mechanobiology of Molecular and Cellular Systems” (3rd-7th of March 2024, Camogli, Genova, Italy)

Bibliography

[1] K. A. Jansen, D. M. Donato, H. E. Balcioglu, T. Schmidt, E. H. J. Danen, and G. H. Koenderink, "A guide to mechanobiology: Where biology and physics meet," *Biochim. Biophys. Acta BBA - Mol. Cell Res.*, vol. 1853, no. 11, pp. 3043–3052, Nov. 2015, doi: 10.1016/j.bbamcr.2015.05.007.

[2] U. S. Schwarz, "Mechanobiology by the numbers: a close relationship between biology and physics," *Nat. Rev. Mol. Cell Biol.*, vol. 18, no. 12, pp. 711–712, Dec. 2017, doi: 10.1038/nrm.2017.109.

[3] B. Coste *et al.*, "Piezo1 and Piezo2 Are Essential Components of Distinct Mechanically Activated Cation Channels," *Science*, vol. 330, no. 6000, pp. 55–60, Oct. 2010, doi: 10.1126/science.1193270.

[4] M. J. Caterina, M. A. Schumacher, M. Tominaga, T. A. Rosen, J. D. Levine, and D. Julius, "The capsaicin receptor: a heat-activated ion channel in the pain pathway," *Nature*, vol. 389, no. 6653, pp. 816–824, Oct. 1997, doi: 10.1038/39807.

[5] S. Phuyal and F. Baschieri, "Endomembranes: Unsung Heroes of Mechanobiology?," *Front. Bioeng. Biotechnol.*, vol. 8, p. 597721, Oct. 2020, doi: 10.3389/fbioe.2020.597721.

[6] S. Kumar and V. M. Weaver, "Mechanics, malignancy, and metastasis: The force journey of a tumor cell," *Cancer Metastasis Rev.*, vol. 28, no. 1–2, pp. 113–127, Jun. 2009, doi: 10.1007/s10555-008-9173-4.

[7] B. Alberts, *Molecular biology of the cell*, Sixth edition. New York, NY: Garland Science, Taylor and Francis Group, 2015.

[8] S. Parenti *et al.*, "A novel 2,3-benzodiazepine-4-one derivative AMPA antagonist inhibits G2/M transition and induces apoptosis in human leukemia Jurkat T cell line," *Life Sci.*, vol. 152, pp. 117–125, May 2016, doi: 10.1016/j.lfs.2016.03.051.

[9] V. Pirani *et al.*, "A novel benzodiazepine derivative that suppresses microtubule dynamics and impairs mitotic progression," *J. Cell Sci.*, vol. 133, no. 7, p. jcs239244, Apr. 2020, doi: 10.1242/jcs.239244.

[10] G. Ferraro, M. Mozzicafreddo, R. Ettari, L. Corsi, and M. C. Monti, "A Proteomic Platform Unveils the Brain Glycogen Phosphorylase as a Potential Therapeutic Target for Glioblastoma Multiforme," *Int. J. Mol. Sci.*, vol. 23, no. 15, p. 8200, Jul. 2022, doi: 10.3390/ijms23158200.

[11] C. Argentati *et al.*, "Insight into Mechanobiology: How Stem Cells Feel Mechanical Forces and Orchestrate Biological Functions," *Int. J. Mol. Sci.*, vol. 20, no. 21, p. 5337, Oct. 2019, doi: 10.3390/ijms20215337.

[12] M. Millard, S. Odde, and N. Neamati, "Integrin Targeted Therapeutics," *Theranostics*, vol. 1, pp. 154–188, 2011, doi: 10.7150/thno/v01p0154.

[13] M. Vicente-Manzanares, X. Ma, R. S. Adelstein, and A. R. Horwitz, "Non-muscle myosin II takes centre stage in cell adhesion and migration," *Nat. Rev. Mol. Cell Biol.*, vol. 10, no. 11, pp. 778–790, Nov. 2009, doi: 10.1038/nrm2786.

[14] S. Choi, Ed., *Encyclopedia of Signaling Molecules*. Cham: Springer International Publishing, 2018. doi: 10.1007/978-3-319-67199-4.

[15] J. A. Spudich, "The myosin swinging cross-bridge model," *Nat. Rev. Mol. Cell Biol.*, vol. 2, no. 5, pp. 387–392, May 2001, doi: 10.1038/35073086.

[16] J. Limouze, A. F. Straight, T. Mitchison, and J. R. Sellers, "Specificity of blebbistatin, an inhibitor of myosin II," *J. Muscle Res. Cell Motil.*, vol. 25, no. 4–5, pp. 337–341, Jul. 2004, doi: 10.1007/s10974-004-6060-7.

[17] M. Kovács, J. Tóth, C. Hetényi, A. Málnási-Csizmadia, and J. R. Sellers, "Mechanism of Blebbistatin Inhibition of Myosin II," *J. Biol. Chem.*, vol. 279, no. 34, pp. 35557–35563, Aug. 2004, doi: 10.1074/jbc.M405319200.

[18] F. Martino, A. R. Perestrelo, V. Vinarský, S. Pagliari, and G. Forte, "Cellular Mechanotransduction: From Tension to Function," *Front. Physiol.*, vol. 9, p. 824, Jul. 2018, doi: 10.3389/fphys.2018.00824.

[19] A. J. Maniotis, C. S. Chen, and D. E. Ingber, "Demonstration of mechanical connections between integrins, cytoskeletal filaments, and nucleoplasm that stabilize nuclear structure," *Proc. Natl. Acad. Sci.*, vol. 94, no. 3, pp. 849–854, Feb. 1997, doi: 10.1073/pnas.94.3.849.

[20] F. Haque *et al.*, "SUN1 Interacts with Nuclear Lamin A and Cytoplasmic Nesprins To Provide a Physical Connection between the Nuclear Lamina and the Cytoskeleton," *Mol. Cell. Biol.*, vol. 26, no. 10, pp. 3738–3751, May 2006, doi: 10.1128/MCB.26.10.3738-3751.2006.

[21] G. P. De Freitas Nader and J. M. García-Arcos, "Cell migration in dense microenvironments," *C. R. Biol.*, vol. 346, no. G2, pp. 89–93, Sep. 2023, doi: 10.5802/crbiol.124.

[22] E. C. Tapley and D. A. Starr, "Connecting the nucleus to the cytoskeleton by SUN–KASH bridges across the nuclear envelope," *Curr. Opin. Cell Biol.*, vol. 25, no. 1, pp. 57–62, Feb. 2013, doi: 10.1016/j.ceb.2012.10.014.

[23] J. Leng, C. Wang, Z. Liang, F. Qiu, S. Zhang, and Y. Yang, "An updated review of YAP: A promising therapeutic target against cardiac aging?," *Int. J. Biol. Macromol.*, vol. 254, p. 127670, Jan. 2024, doi: 10.1016/j.ijbiomac.2023.127670.

[24] G. Nardone *et al.*, "YAP regulates cell mechanics by controlling focal adhesion assembly," *Nat. Commun.*, vol. 8, no. 1, p. 15321, May 2017, doi: 10.1038/ncomms15321.

[25] F. D. Camargo *et al.*, "YAP1 Increases Organ Size and Expands Undifferentiated Progenitor Cells," *Curr. Biol.*, vol. 17, no. 23, pp. 2054–2060, Dec. 2007, doi: 10.1016/j.cub.2007.10.039.

[26] N. P. Talele, J. Fradette, J. E. Davies, A. Kapus, and B. Hinz, "Expression of α-Smooth Muscle Actin Determines the Fate of Mesenchymal Stromal Cells," *Stem Cell Rep.*, vol. 4, no. 6, pp. 1016–1030, Jun. 2015, doi: 10.1016/j.stemcr.2015.05.004.

[27] S. Yang, F. Huang, F. Zhang, X. Sheng, W. Fan, and W. L. Dissanayaka, “Emerging Roles of YAP/TAZ in Tooth and Surrounding: from Development to Regeneration,” *Stem Cell Rev. Rep.*, vol. 19, no. 6, pp. 1659–1675, Aug. 2023, doi: 10.1007/s12015-023-10551-z.

[28] B. C. Low, C. Q. Pan, G. V. Shivashankar, A. Bershadsky, M. Sudol, and M. Sheetz, “YAP/TAZ as mechanosensors and mechanotransducers in regulating organ size and tumor growth,” *FEBS Lett.*, vol. 588, no. 16, pp. 2663–2670, Aug. 2014, doi: 10.1016/j.febslet.2014.04.012.

[29] P. Gaspar and N. Tapon, “Sensing the local environment: actin architecture and Hippo signalling,” *Curr. Opin. Cell Biol.*, vol. 31, pp. 74–83, Dec. 2014, doi: 10.1016/j.ceb.2014.09.003.

[30] I. Andreu *et al.*, “The force loading rate drives cell mechanosensing through both reinforcement and cytoskeletal softening,” *Nat. Commun.*, vol. 12, no. 1, p. 4229, Jul. 2021, doi: 10.1038/s41467-021-24383-3.

[31] A. Elosegui-Artola *et al.*, “Force Triggers YAP Nuclear Entry by Regulating Transport across Nuclear Pores,” *Cell*, vol. 171, no. 6, pp. 1397-1410.e14, Nov. 2017, doi: 10.1016/j.cell.2017.10.008.

[32] D. Y. M. Leung, S. Glagov, and M. B. Mathews, “A new in vitro system for studying cell response to mechanical stimulation,” *Exp. Cell Res.*, vol. 109, no. 2, pp. 285–298, Oct. 1977, doi: 10.1016/0014-4827(77)90008-8.

[33] A. Roshanzadeh *et al.*, “Mechanoadaptive organization of stress fiber subtypes in epithelial cells under cyclic stretches and stretch release,” *Sci. Rep.*, vol. 10, no. 1, p. 18684, Oct. 2020, doi: 10.1038/s41598-020-75791-2.

[34] N. Campillo *et al.*, “A Novel Chip for Cyclic Stretch and Intermittent Hypoxia Cell Exposures Mimicking Obstructive Sleep Apnea,” *Front. Physiol.*, vol. 7, Jul. 2016, doi: 10.3389/fphys.2016.00319.

[35] J. Zhao, F. Meng, J. Qian, Y. Huang, and Y. Fan, “In vitro cell stretching devices and their applications: From cardiomyogenic differentiation to tissue engineering,” *Med. Nov. Technol. Devices*, vol. 18, p. 100220, Jun. 2023, doi: 10.1016/j.medntd.2023.100220.

[36] I. Constantinou and E. E. Bastounis, “Cell-stretching devices: advances and challenges in biomedical research and live-cell imaging,” *Trends Biotechnol.*, p. S0167779922003328, Jan. 2023, doi: 10.1016/j.tibtech.2022.12.009.

[37] L. Terracio, B. Miller, and T. K. Borg, “Effects of cyclic mechanical stimulation of the cellular components of the heart: In vitro,” *In Vitro Cell. Dev. Biol.*, vol. 24, no. 1, pp. 53–58, Jan. 1988, doi: 10.1007/BF02623815.

[38] H. Wang and E. S. Grood, “Cell Orientation Response to Cyclically Deformed Substrates: Experimental Validation of a Cell Model”.

[39] G. Ragazzini, J. Guerzoni, A. Mescola, D. Di Rosa, L. Corsi, and A. Alessandrini, “A Fully Integrated Arduino-Based System for the Application of Stretching Stimuli to Living Cells and Their Time-Lapse Observation: A Do-It-Yourself Biology Approach,”

Ann. Biomed. Eng., vol. 49, no. 9, pp. 2243–2259, Sep. 2021, doi: 10.1007/s10439-021-02758-3.

[40] V. Barron *et al.*, "The effect of physiological cyclic stretch on the cell morphology, cell orientation and protein expression of endothelial cells," *J. Mater. Sci. Mater. Med.*, vol. 18, no. 10, pp. 1973–1981, Sep. 2007, doi: 10.1007/s10856-007-3125-3.

[41] J. H.-C. Wang, P. Goldschmidt-Clermont, J. Wille, and F. C.-P. Yin, "Specificity of endothelial cell reorientation in response to cyclic mechanical stretching," *J. Biomech.*, vol. 34, no. 12, pp. 1563–1572, Dec. 2001, doi: 10.1016/S0021-9290(01)00150-6.

[42] C. Giverso, N. Loy, G. Lucci, and L. Preziosi, "Cell orientation under stretch: A review of experimental findings and mathematical modelling," *J. Theor. Biol.*, vol. 572, p. 111564, Sep. 2023, doi: 10.1016/j.jtbi.2023.111564.

[43] A. Livne, E. Bouchbinder, and B. Geiger, "Cell reorientation under cyclic stretching," *Nat. Commun.*, vol. 5, no. 1, p. 3938, May 2014, doi: 10.1038/ncomms4938.

[44] S. Chagnon-Lessard, H. Jean-Ruel, M. Godin, and A. E. Pelling, "Cellular orientation is guided by strain gradients," *Integr. Biol.*, vol. 9, no. 7, pp. 607–618, 2017, doi: 10.1039/C7IB00019G.

[45] S. Seetharaman and S. Etienne-Manneville, "Cytoskeletal Crosstalk in Cell Migration," *Trends Cell Biol.*, vol. 30, no. 9, pp. 720–735, Sep. 2020, doi: 10.1016/j.tcb.2020.06.004.

[46] K. Paňková, D. Rösel, M. Novotný, and J. Brábek, "The molecular mechanisms of transition between mesenchymal and amoeboid invasiveness in tumor cells," *Cell. Mol. Life Sci.*, vol. 67, no. 1, pp. 63–71, Jan. 2010, doi: 10.1007/s00018-009-0132-1.

[47] J. E. Bear and J. M. Haugh, "Directed migration of mesenchymal cells: where signaling and the cytoskeleton meet," *Curr. Opin. Cell Biol.*, vol. 30, pp. 74–82, Oct. 2014, doi: 10.1016/j.ceb.2014.06.005.

[48] J. Schick and E. Raz, "Blebs—Formation, Regulation, Positioning, and Role in Amoeboid Cell Migration," *Front. Cell Dev. Biol.*, vol. 10, p. 926394, Jul. 2022, doi: 10.3389/fcell.2022.926394.

[49] G. Charras and E. Paluch, "Blebs lead the way: how to migrate without lamellipodia," *Nat. Rev. Mol. Cell Biol.*, vol. 9, no. 9, pp. 730–736, Sep. 2008, doi: 10.1038/nrm2453.

[50] T. Mitchison and M. Kirschner, "Cytoskeletal dynamics and nerve growth," *Neuron*, vol. 1, no. 9, pp. 761–772, Nov. 1988, doi: 10.1016/0896-6273(88)90124-9.

[51] C. E. Chan and D. J. Odde, "Traction Dynamics of Filopodia on Compliant Substrates," *Science*, vol. 322, no. 5908, pp. 1687–1691, Dec. 2008, doi: 10.1126/science.1163595.

[52] B. L. Bangasser, S. S. Rosenfeld, and D. J. Odde, "Determinants of Maximal Force Transmission in a Motor-Clutch Model of Cell Traction in a Compliant Microenvironment," *Biophys. J.*, vol. 105, no. 3, pp. 581–592, Aug. 2013, doi: 10.1016/j.bpj.2013.06.027.

[53] A. Elosegui-Artola, X. Trepat, and P. Roca-Cusachs, “Control of Mechanotransduction by Molecular Clutch Dynamics,” *Trends Cell Biol.*, vol. 28, no. 5, pp. 356–367, May 2018, doi: 10.1016/j.tcb.2018.01.008.

[54] M. Yao, B. T. Goult, H. Chen, P. Cong, M. P. Sheetz, and J. Yan, “Mechanical activation of vinculin binding to talin locks talin in an unfolded conformation,” *Sci. Rep.*, vol. 4, no. 1, p. 4610, Apr. 2014, doi: 10.1038/srep04610.

[55] Z. Xu, F. Xu, and B. Cheng, “The motor-clutch model in mechanobiology and mechanomedicine,” *Mechanobiol. Med.*, vol. 2, no. 3, p. 100067, Sep. 2024, doi: 10.1016/j.mbm.2024.100067.

[56] M. Pesce *et al.*, “Cardiac fibroblasts and mechanosensation in heart development, health and disease,” *Nat. Rev. Cardiol.*, Nov. 2022, doi: 10.1038/s41569-022-00799-2.

[57] X. Fu *et al.*, “Specialized fibroblast differentiated states underlie scar formation in the infarcted mouse heart,” *J. Clin. Invest.*, vol. 128, no. 5, pp. 2127–2143, May 2018, doi: 10.1172/JCI98215.

[58] K. C. M. Hermans, E. P. Daskalopoulos, and W. M. Blankesteijn, “The Janus face of myofibroblasts in the remodeling heart,” *J. Mol. Cell. Cardiol.*, vol. 91, pp. 35–41, Feb. 2016, doi: 10.1016/j.yjmcc.2015.11.017.

[59] S. W. M. Van Den Borne, J. Diez, W. M. Blankesteijn, J. Verjans, L. Hofstra, and J. Narula, “Myocardial remodeling after infarction: the role of myofibroblasts,” *Nat. Rev. Cardiol.*, vol. 7, no. 1, pp. 30–37, Jan. 2010, doi: 10.1038/nrcardio.2009.199.

[60] M. D’Urso and N. A. Kurniawan, “Mechanical and Physical Regulation of Fibroblast–Myofibroblast Transition: From Cellular Mechanoresponse to Tissue Pathology,” *Front. Bioeng. Biotechnol.*, vol. 8, p. 609653, Dec. 2020, doi: 10.3389/fbioe.2020.609653.

[61] T. C. L. Bracco Gartner *et al.*, “Advanced *In Vitro* Modeling to Study the Paradox of Mechanically Induced Cardiac Fibrosis,” *Tissue Eng. Part C Methods*, vol. 27, no. 2, pp. 100–114, Feb. 2021, doi: 10.1089/ten.tec.2020.0298.

[62] C. Beadle, M. C. Assanah, P. Monzo, R. Vallee, S. S. Rosenfeld, and P. Canoll, “The Role of Myosin II in Glioma Invasion of the Brain,” *Mol. Biol. Cell*, vol. 19, no. 8, pp. 3357–3368, Aug. 2008, doi: 10.1091/mbc.e08-03-0319.

[63] M. Inukai *et al.*, “A functional role of S100A4/non-muscle myosin IIA axis for pro-tumorigenic vascular functions in glioblastoma,” *Cell Commun. Signal.*, vol. 20, no. 1, p. 46, Dec. 2022, doi: 10.1186/s12964-022-00848-w.

[64] N. V. Krakhmal, M. V. Zavyalova, E. V. Denisov, S. V. Vtorushin, and V. M. Perelmuter, “Cancer Invasion: Patterns and Mechanisms,” *Acta Naturae*, vol. 7, no. 2, pp. 17–28, Jun. 2015, doi: 10.32607/20758251-2015-7-2-17-28.

[65] G. Rigillo *et al.*, “The NF–Y splicing signature controls hybrid EMT and ECM-related pathways to promote aggressiveness of colon cancer,” *Cancer Lett.*, vol. 567, p. 216262, Jul. 2023, doi: 10.1016/j.canlet.2023.216262.

[66] D. Dolfini, M. Minuzzo, G. Pavesi, and R. Mantovani, “The Short Isoform of NF-YA Belongs to the Embryonic Stem Cell Transcription Factor Circuitry,” *STEM CELLS*, vol. 30, no. 11, pp. 2450–2459, Nov. 2012, doi: 10.1002/stem.1232.

[67] D. Dolfini, V. Andrioletti, and R. Mantovani, “Overexpression and alternative splicing of NF-YA in breast cancer,” *Sci. Rep.*, vol. 9, no. 1, p. 12955, Sep. 2019, doi: 10.1038/s41598-019-49297-5.

[68] S. Belluti *et al.*, “Alternative splicing of NF-YA promotes prostate cancer aggressiveness and represents a new molecular marker for clinical stratification of patients,” *J. Exp. Clin. Cancer Res.*, vol. 40, no. 1, p. 362, Dec. 2021, doi: 10.1186/s13046-021-02166-4.

[69] G. Ragazzini, A. Mescola, L. Corsi, and A. Alessandrini, “Fabrication of a low-cost on-stage cell incubator with full automation,” *J. Biol. Educ.*, vol. 53, no. 2, pp. 165–173, Mar. 2019, doi: 10.1080/00219266.2018.1451772.

[70] S. Schürmann *et al.*, “The IsoStretcher: An isotropic cell stretch device to study mechanical biosensor pathways in living cells,” *Biosens. Bioelectron.*, vol. 81, pp. 363–372, Jul. 2016, doi: 10.1016/j.bios.2016.03.015.

[71] R. N. Palchesko, L. Zhang, Y. Sun, and A. W. Feinberg, “Development of Polydimethylsiloxane Substrates with Tunable Elastic Modulus to Study Cell Mechanobiology in Muscle and Nerve,” *PLoS ONE*, vol. 7, no. 12, p. e51499, Dec. 2012, doi: 10.1371/journal.pone.0051499.

[72] M. Fincan, “Assessing Viscoelastic Properties of Polydimethylsiloxane (PDMS) Using Loading and Unloading of the Macroscopic Compression Test”.

[73] H. S. Cho, H. Moon, H. S. Lee, Y. T. Kim, and S. C. Jeoung, “Formulation Prediction for Young’s Modulus of Poly(dimethylsiloxane) by Spectroscopic Methods,” *Bull. Korean Chem. Soc.*, vol. 42, no. 9, pp. 1225–1231, Sep. 2021, doi: 10.1002/bkcs.12352.

[74] X. Li, K. Chan, and R. Ramer, “Fabrication of Through via Holes in Ultra-Thin Fused Silica Wafers for Microwave and Millimeter-Wave Applications,” *Micromachines*, vol. 9, no. 3, p. 138, Mar. 2018, doi: 10.3390/mi9030138.

[75] T. Mao *et al.*, “Critical Frequency and Critical Stretching Rate for Reorientation of Cells on a Cyclically Stretched Polymer in a Microfluidic Chip,” *ACS Appl. Mater. Interfaces*, vol. 13, no. 12, pp. 13934–13948, Mar. 2021, doi: 10.1021/acsami.0c21186.

[76] V. Basile *et al.*, “NF-YA splice variants have different roles on muscle differentiation,” *Biochim. Biophys. Acta BBA - Gene Regul. Mech.*, vol. 1859, no. 4, pp. 627–638, Apr. 2016, doi: 10.1016/j.bbagrm.2016.02.011.

[77] D. Ershov *et al.*, “TrackMate 7: integrating state-of-the-art segmentation algorithms into tracking pipelines,” *Nat. Methods*, vol. 19, no. 7, pp. 829–832, Jul. 2022, doi: 10.1038/s41592-022-01507-1.

[78] Y. Hu, M. L. Becker, and R. K. Willits, “Quantification of cell migration: metrics selection to model application,” *Front. Cell Dev. Biol.*, vol. 11, p. 1155882, May 2023, doi: 10.3389/fcell.2023.1155882.

[79] I. D. Luzhansky *et al.*, “Anomalously diffusing and persistently migrating cells in 2D and 3D culture environments,” *APL Bioeng.*, vol. 2, no. 2, p. 026112, Jun. 2018, doi: 10.1063/1.5019196.

[80] H. G. Othmer, S. R. Dunbar, and W. Alt, “Models of dispersal in biological systems,” *J. Math. Biol.*, vol. 26, no. 3, pp. 263–298, Jun. 1988, doi: 10.1007/BF00277392.

[81] J. B. Kelley and B. M. Paschal, “Fluorescence-based quantification of nucleocytoplasmic transport,” *Methods*, vol. 157, pp. 106–114, Mar. 2019, doi: 10.1016/j.ymeth.2018.11.002.

[82] E. Kim *et al.*, “YAP mechanotransduction under cyclic mechanical stretch loading for mesenchymal stem cell osteogenesis is regulated by ROCK,” *Front. Bioeng. Biotechnol.*, vol. 11, p. 1306002, Jan. 2024, doi: 10.3389/fbioe.2023.1306002.

[83] K. Imanaka-Yoshida and H. Aoki, “Tenascin-C and mechanotransduction in the development and diseases of cardiovascular system,” *Front. Physiol.*, vol. 5, Jul. 2014, doi: 10.3389/fphys.2014.00283.

[84] E. W. Howard *et al.*, “MMP-2 expression by fibroblasts is suppressed by the myofibroblast phenotype,” *Exp. Cell Res.*, vol. 318, no. 13, pp. 1542–1553, Aug. 2012, doi: 10.1016/j.yexcr.2012.03.007.

[85] Y. Zhang *et al.*, “Two-Pore-Domain Potassium Channel TREK–1 Mediates Pulmonary Fibrosis through Macrophage M2 Polarization and by Direct Promotion of Fibroblast Differentiation,” *Biomedicines*, vol. 11, no. 5, p. 1279, Apr. 2023, doi: 10.3390/biomedicines11051279.

[86] D. M. Abraham *et al.*, “The two-pore domain potassium channel TREK-1 mediates cardiac fibrosis and diastolic dysfunction,” *J. Clin. Invest.*, vol. 128, no. 11, pp. 4843–4855, Oct. 2018, doi: 10.1172/JCI95945.

[87] R. K. Adapala, V. Katari, L. R. Teegala, S. Thodeti, S. Paruchuri, and C. K. Thodeti, “TRPV4 Mechanotransduction in Fibrosis,” *Cells*, vol. 10, no. 11, p. 3053, Nov. 2021, doi: 10.3390/cells10113053.

[88] Y. Chen, A. M. Pasapera, A. P. Koretsky, and C. M. Waterman, “Orientation-specific responses to sustained uniaxial stretching in focal adhesion growth and turnover,” *Proc. Natl. Acad. Sci.*, vol. 110, no. 26, Jun. 2013, doi: 10.1073/pnas.1221637110.

[89] S. Das, A. Ippolito, P. McGarry, and V. S. Deshpande, “Cell reorientation on a cyclically strained substrate,” *PNAS Nexus*, vol. 1, no. 5, p. pgac199, Nov. 2022, doi: 10.1093/pnasnexus/pgac199.

[90] S. Mondésert-Deveraux, D. Aubry, and R. Allena, “In silico approach to quantify nucleus self-deformation on micropillared substrates,” *Biomech. Model. Mechanobiol.*, vol. 18, no. 5, pp. 1281–1295, Oct. 2019, doi: 10.1007/s10237-019-01144-2.

[91] X. Liu, R. Liu, Y. Gu, and J. Ding, “Nonmonotonic Self-Deformation of Cell Nuclei on Topological Surfaces with Micropillar Array,” *ACS Appl. Mater. Interfaces*, vol. 9, no. 22, pp. 18521–18530, Jun. 2017, doi: 10.1021/acsami.7b04027.

[92] A. Foss *et al.*, “Patient-derived glioblastoma cells (GBM) exhibit distinct biomechanical profiles associated with altered activity in the cytoskeleton regulatory pathway,” Jul. 17, 2020. doi: 10.1101/2020.07.16.207233.

[93] P. Dixit, I. Djafer-Cherif, S. Shah, A. Traulsen, and B. Waclaw, “A quantitative characterization of the heterogeneous response of glioblastoma U-87 MG cell line to temozolomide,” Jun. 02, 2024. doi: 10.1101/2024.05.28.596108.

[94] Z. Yang *et al.*, “The destruction of cytoplasmic skeleton leads to the change of nuclear structure and the looseness of lamin A submicroscopic network,” *Heliyon*, vol. 10, no. 18, p. e36583, Sep. 2024, doi: 10.1016/j.heliyon.2024.e36583.

[95] S. Mishra and D. L. Levy, “Nuclear F-actin and Lamin A antagonistically modulate nuclear shape,” *J. Cell Sci.*, vol. 135, no. 13, p. jcs259692, Jul. 2022, doi: 10.1242/jcs.259692.

[96] A. J. Lomakin *et al.*, “The nucleus acts as a ruler tailoring cell responses to spatial constraints,” *Science*, vol. 370, no. 6514, p. eaba2894, Oct. 2020, doi: 10.1126/science.aba2894.

[97] J. C. Martens and M. Radmacher, “Softening of the actin cytoskeleton by inhibition of myosin II,” *Pflüg. Arch. - Eur. J. Physiol.*, vol. 456, no. 1, pp. 95–100, Apr. 2008, doi: 10.1007/s00424-007-0419-8.

Appendix

In this Thesis ImageJ was largely used to perform image analysis and sometimes, given the file hierarchy of the computer of the optical microscope and the large number of acquired images (TIFF files), it became clear that we needed to automatize on some level image management. To do so, I developed small ImageJ macros intended to organize the input/output of already existing ImageJ plugins, in order to ease file management and reduce time-consuming manual operations. Following the open access philosophy of the ImageJ community, in this Appendix a small collection of these macros is included.

Suggestion: to avoid any troubleshoot and bug, directories and filenames should not contain spacings (prefer underscores instead), and filenames should be numbered with padding (e.g. image_0001.tif).

A.1 Alignment of two-channel stacks

The original *Template Matching* plugin for ImageJ, developed by Qingzong Tseng (https://sites.google.com/site/qingzongtseng/template-matching-ij-plugin) was included into a macro in order to perform alignment for two-channel stacks (e.g. time-lapse imaging of a cell sample with phase contrast and a fluorescent marker).

The idea behind the macro is that the Results printed at the end of the alignment process performed on the optical channel are stored and used to translate, slice by slice, the fluorescence stack. Finally, the two stacks are merged into a composite. Below, a simple workflow sums up the macro steps.

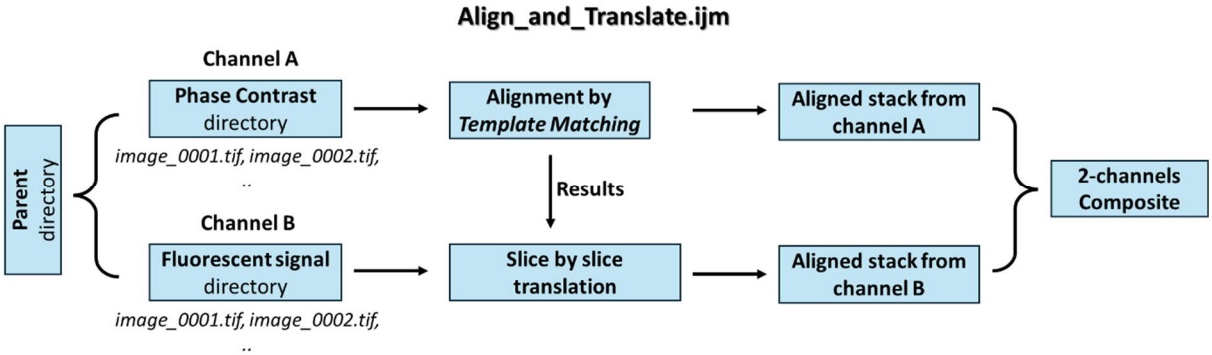

The following code performs alignment on a phase contrast stack and translation on the fluorescent stack of the DAPI signal (but channels can be changed directly in the code).

Align_and_Translate.ijm

```
//Beatrice Bighi 01/04/2022

/*This macro aligns a first set images from a channel (channel A) with the "Template Matching"
plugin by Qingzong Tseng [https://sites.google.com/site/qingzongtseng/template-matching-ij-
plugin] and performs the same alignment on a second set of images coming from a second channel
(channel B).

Please note that this macro requires the images to be named with a padded numbered (e.g.
image_0001.tif).
Also, please make sure that file paths do not contain any spaces.
It is possible to change the name of the folders from "channel A" and "channel B" used by the
macro by changing directly the code at lines 20, 21 and 24.;

The macro was originally thought for 2-channels stacks (Gray + Blue channel), for different
combinations of channels edit the code at lines 185 and 198 following the given legend:
c1 Red, c2 Green, c3 Blue, c4 Gray.*/

//Step 0: Defining folders containing the two sets of images
run("Clear Results");
print("\\Clear");

directory     = getDirectory("Please select the experiment directory.");
File.setDefaultDir(directory);

/*The script automatically recognizes as channel A the folder "ContrastoFase"
and as channel B the folder "Fluorescenza", to changes this, edit the following lines.*/

channel_A    = directory + "ContrastoFase/";
channel_B     = directory + "Fluorescenza/";

//A new folder containing the translated images from channel B is created (you could choose to
name yours "ChannelB_translated" for instance).
name_for_new_folder = "FluorescenzaTraslata";
File.makeDirectory(directory + name_for_new_folder+"/");
channel_B_trans    = directory + name_for_new_folder+"/";

name_for_stack_A = "Stack_A";

//Scanning elements in folder for Channel B.
channel_B_List     = getFileList(channel_B);

//Array to make choices.
items = newArray(2);
items[0] = "Yes";
items[1] = "No";

//*************************************************************************************************
*************************************************************************************************
//Step 1: Aligning the first stack (images from channel A)
print("Opening the first stack of images, from channel A. Please wait..");
run("Image Sequence...", "dir=["+ channel_A +"] sort");

run("8-bit");
run("Enhance Contrast...", "saturated=0.35 normalize process_all");
rename("Channel A");

n_slices = nSlices();
//print("The number of slices is:" + n_slices);

waitForUser("Align the stack\n1) Select a rectangle\n2) Plugin -- Template Matching -- Align
slices in stack.\n3) After the alignment has finished, press Ok to continue.");
    Dialog.create("Which is the slice number you used for aligning?");
    Dialog.addNumber("Which is the slice number you used for aligning?", 1);
    Dialog.show();
    ref_slice = Dialog.getNumber();
    //print("Reference slide:"+ref_slice)

waitForUser("Check the outcome of the alignment using the slider bar.\nThen press OK.");
```

```
    Dialog.create("Is the alignment good?");
    Dialog.addChoice("Is the alignment good?", items);
    Dialog.show();
    choice_1 = Dialog.getChoice();

if (choice_1 == "Yes"){
    print("Please wait, saving..");
    selectWindow("Channel A");
    saveAs("Tiff", directory + name_for_stack_A+"_align.tif");
    saveAs("Results", directory + "Coord_alignment.txt");
    print("The stack from channel A was aligned and correctly saved.");

    //Export of the translations applied to each slice in a temporary txt file
    Table.open(directory + "Coord_alignment.txt")
    x = newArray(n_slices);
    y = newArray(n_slices);
    slice = newArray(n_slices);

    //Reading the exported data
    for (i=0; i<n_slices; i++){

        if (i<n_slices-1) {
            x[i] = Table.get("dX", i);
            y[i] = Table.get("dY", i);
            slice[i] = Table.get("Slice", i);
            }

        //Adding to the translation file the null-translation applied to the reference slice
        if (i == n_slices-1) {
            x[i] = 0;
            y[i] = 0;
            slice[i] = ref_slice;
            }
        }

    //Choose what interval of images from the channel B you want to translate (default setting
include the whole stack)
    slice_init = 1;
    slice_fin = n_slices;

    Dialog.create("Choose initial/last slice from channel B");
    Dialog.addMessage("Now, we are going to translate images from channel B.\n");
    Dialog.addMessage("This feature can be helpful in case you want to translate just a specific
interval of images from channel B.\nDefault values include the whole stack.");

    Dialog.addNumber("Initial slice", slice_init);
    Dialog.addNumber("Last slice", n_slices);
    Dialog.show();
    slice_init = Dialog.getNumber();
    slice_fin = Dialog.getNumber();


    //print("Vector x contains the X coordinates"); Array.print(x);
    //print("Vector y contains the Y coordinates"); Array.print(y);
    //print("Vector index contains the indexes of the processed slices"); Array.print(slice);
    //Array.show("Slice/x/y", slice, x, y);

    print("Sorting..");

    Array.sort(slice,x,y);
    //print("Sorted vectors are:");
    //print("Slice:"); Array.print(slice);
    //print("x:");Array.print(x);
    //print("y:");Array.print(y);

    //Array.show("Slice/x/y sorted", slice, x, y);

    close("*");

    print("The stack from channel A is done.");
    close("*");
```

```
}else{
    waitForUser("Macro aborted. Please re-launch the macro.");
    close("*");
    exit
    }

//*************************************************************************************************
*************************************************************************************************
//Step 2: Translating images from Channel B accordingly to the translation applied for the images
of Channel A.
print("Translating the images from the channel B. Please wait..");

for (i=slice_init-1; i<slice_fin; i++){
    //Translating the reference slice
    if(i == ref_slice-1){
        print("Translating reference slice "+(i+1)+" of "+slice_fin-slice_init);
        open(channel_B + channel_B_List[i]);
        run("8-bit");
        //run("Enhance Contrast...", "saturated=0.35 normalize");
        run("Subtract Background...", "rolling=50 sliding");
        save(channel_B_trans + getTitle() + ".tif");
        close();


        //Translating the rest of the slices
        }else{
        print("Translating slice "+(i+1)+" of "+slice_fin-slice_init);
        open(channel_B + channel_B_List[i]);
        run("8-bit");
        //run("Enhance Contrast...", "saturated=0.35 normalize");
        run("Subtract Background...", "rolling=50 sliding");
        run("Translate...", "x="+ x[i] +" y="+ y[i] +" interpolation=None");
        save(channel_B_trans + getTitle() + ".tif");
        close();
        }
}

print("Images from Channel B successfully translated accordingly.");

//*************************************************************************************************
*************************************************************************************************
//Step 3: Merging & Post-processing
print("Opening stacks from channel A and B. Please wait..");

//Opening the aligned Stack from Channel A
open(directory + name_for_stack_A+"_align.tif");
run("8-bit");
run("Duplicate...", "title="+name_for_stack_A+"_align-1 ignore duplicate range="+slice_init+"-
"+slice_fin+"");
selectWindow(name_for_stack_A+"_align.tif");
close();

//Opening the aligned Stack from Channel B_translated
run("Image Sequence...", "select=["+ channel_B_trans+"] dir=["+ channel_B_trans+"] sort");
run("8-bit");

//Merging the two stacks
print("Merging the two stacks..");
run("Merge Channels...", "c3=["+name_for_new_folder+"] c4=["+name_for_stack_A+"_align-1]
create");
//c1 Red, c2 Green, c3 Blue, c4 Gray

//Checkpoint to post-process the composite before saving
setTool("rectangle");
//Cropping out black areas
waitForUser("Now you can post-process the stacks.\nPlease, crop out any black area from the
stack.\nPress OK when you are done.");

//Splitting channels to enhance the Channel 2 signal. Merging channels together again.
selectWindow("Composite");
```

```
run("Split Channels");
selectImage("C1-Composite");
run("Enhance Contrast...", "saturated=0.35 normalize process_all");
run("Merge Channels...", "c3=C1-Composite c4=C2-Composite create");

//Saving in TIFF
waitForUser("Ready to save? If additional post-processing is needed, press OK when you are
done.");
print("Saving the composite as a TIFF file. Please wait..");
saveAs("Tiff", directory + "Composite.tif");

//Deleting temporary files
File.delete(directory+"Stack_A_align.tif");
File.delete(channel_B_trans);

print("Done!");
beep();
```

A.2 Grid Stitching of images from multiple directories

This macro eases the grid stitching of images coming from different directories, applying the *Grid/Collection stitching* plugin (https://imagej.net/plugins/grid-collection-stitching) developed by Preibisch et al. [1]. Since time-lapse images of adjacent spots were saved in different directories, we needed a quick way to apply the Grid Stitching plugin without manually moving files around. The macro only deals with rectangular and square grids and exploits the "Snake by rows/Right & Down" mode.

Below is a simple scheme of the macro workflow for a 2x2 square tile.

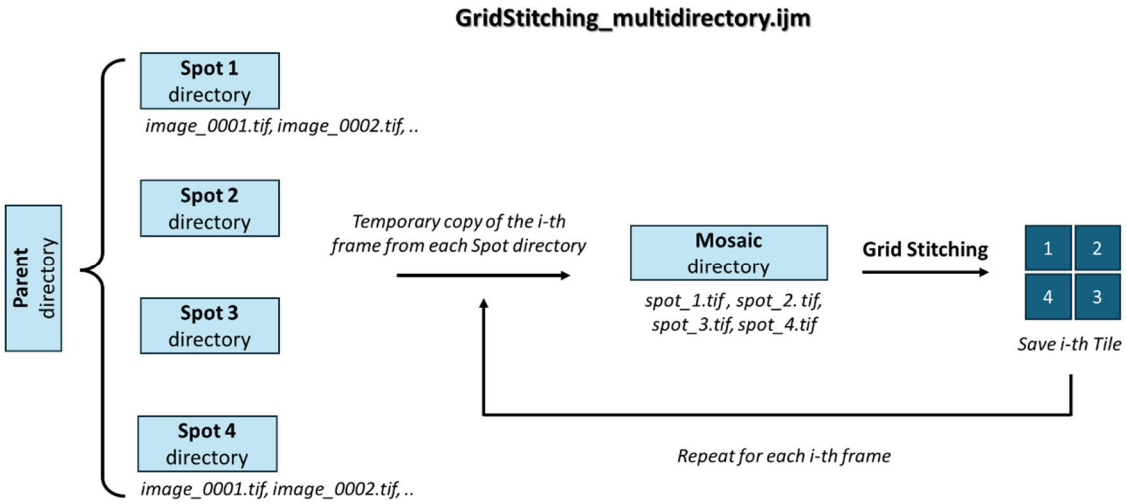

[1] S. Preibisch, S. Saalfeld, e P. Tomancak, «Globally optimal stitching of tiled 3D microscopic image acquisitions», *Bioinformatics*, vol. 25, fasc. 11, pp. 1463–1465, giu. 2009, doi: 10.1093/bioinformatics/btp184.

Grid_Stitching_multidirectory.ijm

```
//Beatrice Bighi last modified 27/03/2023
print("\\Clear");

/*This macro performs custom Grid Stitching (see https://imagej.net/plugins/grid-collection-
stitching) to obtain rectangular mosaics from images collected during time-lapse imaging, from
adjacent spots. Usually, images collected for each spot are stored in separate folders: this
macro collects the different tiles corresponding to a certain time point from each folder and
performs the Grid Stitching routine. The user is required to provide the shape of the final
mosaic (n_x * n_y) and the expected overlap between tiles.*/

main_directory = getDirectory("Experiment folder containing the different tiles subfolders");
File.setDefaultDir(main_directory);
number_x = 4;
number_y = 1;
overlap = 20;
number = 1;

input_path_ = newArray();
item = newArray(2);
    item[1] = "Yes";
    item[0] = "No";

//Ask the user the parameters to build the final mosaic
    Dialog.create("Parameters");
    Dialog.addMessage("Please specify the following final mosaic parameters");
    Dialog.addNumber("Nr. of tiles along x axis:", number_x);
    Dialog.addNumber("Nr. of tiles along y axis:", number_y);
    Dialog.addNumber("Expected tile overlap:", overlap);
    Dialog.show();

    number_x = Dialog.getNumber();
    number_y = Dialog.getNumber();
    overlap = Dialog.getNumber();

    number = number_x * number_y;
    print("The final mosaic shape is:" +number_x+" x "+number_y+" with expected overlap
"+overlap);


//Asking the user to specify which folders are going to be considered as sources
    for (k=0; k<number; k++){
        input_path_[k] = getDirectory("Please, define the folder containing spot nr. "+
(k+1)+"\nPlease note that the default settings expect tiles to be in 'snake by rows' in clockwise
order");
    }

    print("The following folders are considered as spots to recover the tiles from.");
    Array.print(input_path_);

//Creating a folder to save outputs
    File.makeDirectory(main_directory + "mosaic");
    output_path = main_directory + "mosaic";
    print("Mosaics will be saved in: " + output_path);

//Grid Stitching
fileList = getFileList(input_path_[0]);

/*The following for cycle locates the tiles to be merged together, copies them in the current
working directory, performs the Grid Stitching routine,
 * saves the mosaic and deletes files that are not useful anymore.*/

for (i=0; i<fileList.length; i++) {
    for (k=0; k<number; k++){
        open(input_path_[k] + fileList[i]);
        run("8-bit");
        run("Enhance Contrast...", "saturated=0.35 normalize");
        saveAs("Tiff", output_path + "\\spot_" + (k+1) + ".tif");
        close();
```

```
        }

    run("Grid/Collection stitching", "type=[Grid: snake by rows] order=[Right & Down]
grid_size_x="+number_x+" grid_size_y="+number_y+" tile_overlap="+overlap+" first_file_index_i=1
directory="+output_path+" file_names=spot_{i}.tif output_textfile_name=TileConfiguration.txt
fusion_method=[Linear Blending] regression_threshold=0.30 max/avg_displacement_threshold=2.50
absolute_displacement_threshold=3.50 compute_overlap computation_parameters=[Save memory (but be
slower)]");

    //Mosaics are saved with 4-digits numeration
    prefix = "";

    if ((i+1)<10){
        prefix = prefix + "000";
    }
    if ((10<=(i+1)) & ((i+1)<100)){
        prefix = prefix + "00";
    }

    if ((100<=(i+1)) & ((i+1)<1000)){
        prefix = prefix + "0";
    }

    //Saving the current mosaic
    saveAs("Tiff", output_path + "\\mosaic_" + prefix + (i+1) + ".tif");
    close();

    //Deleting files that are no longer useful
    for (k=0; k<number; k++){
        File.delete(output_path + "\\spot_" + (k+1) + ".tif");
        }
    File.delete(output_path + "\\TileConfiguration.registered.txt");
    File.delete(output_path + "\\TileConfiguration.txt");
    }

print("Stitching completed!");
beep();
```

A.3 Stacking images with different dimensions

After the Grid Stitching process, in order to manage the obtained tiles, it is necessary to uniform their dimension since each one of them has slightly different width and height. To do so, tiles are opened as single images and then concatenated into an AVI file which then can be aligned with the original Template Matching plugin.

Stack_tiles.ijm

```
//Beatrice Bighi last modified 18/04/2024

print("\\Clear");

/*This macro creates an AVI stack from the mosaics of different dimensions previously obtained
with the Grid Stitching macro.*/
input_path = getDirectory("Select the folder containing the mosaics to be stacked.");
File.setDefaultDir(input_path);

//Delete useless files that would compromise the macro
File.delete(input_path + "TileConfiguration.registered.txt");
File.delete(input_path + "TileConfiguration.txt");

fileList = getFileList(input_path);

//Setting the number of mosaics to be considered in one stack, since it is not advisable to
consider all of them in just one shot.
n_slices_per_stack = fileList.length;

Dialog.create("How many mosaics");
Dialog.addNumber("How many images would you like to unite in one -intermediate- stack?",
n_slices_per_stack);
Dialog.addMessage("Suggestion: consider 70-80 images maximum; if they are really big 50-60 is
preferable.");
Dialog.show()
n_slices_per_stack = Dialog.getNumber();

//Splitting the workload
images_laststack = fileList.length%n_slices_per_stack;

if (images_laststack == 0) {
    n_stack = floor(fileList.length/n_slices_per_stack);
    }
if (images_laststack != 0) {
    n_stack = floor(fileList.length/n_slices_per_stack) + 1;
    }

print("Dividing the " + fileList.length + " images in " + n_stack + " stacks.");
if (images_laststack != 0) {
    print("The last stack will contain " + images_laststack + " images.");
    }

//Case 1: the number of images to be stacked is a multiple of the splitting value chosen by the
user
if (images_laststack == 0) {
    //Open and stack the images
    for (i=0; i<n_stack; i++) {
        print("Opening the images to create stack nr. " +(i+1));
        for(element=n_slices_per_stack*i; element<n_slices_per_stack*(i+1); element++){
            open(input_path + fileList[element]);
            setOption("ScaleConversions", true);
            run("8-bit");
```

```
            }

            print("Please wait, creating stack nr. " +(i+1));
            run("Images to Stack", "method=[Copy (center)]
name=Stack_"+(n_slices_per_stack*i+1)+"_"+n_slices_per_stack*(i+1)+" title=[] use");

            //Save as AVI
            run("AVI... ", "compression=JPEG frame=10
save="+input_path+"Stack_"+(n_slices_per_stack*i+1)+"_"+n_slices_per_stack*(i+1)+".avi");
            saveAs("AVI",
input_path+"Stack_"+(n_slices_per_stack*i+1)+"_"+n_slices_per_stack*(i+1)+".avi");
            close("*");
            print("Stack nr. " +(i+1)+ " was correctly saved.");
        }
    }

/*Case 2: the number of images to be stacked is not a multiple of the splitting value chosen by
the user. Some extra images will remain, they are going to be dealt with separately*/
if (images_laststack!=0) {
    //Open and stack the images
    for (i=0; i<(n_stack-1); i++) {

    print("Opening images to create stack nr. " +(i+1));

    for(element=n_slices_per_stack*i; element<n_slices_per_stack*(i+1); element++){
        open(input_path + fileList[element]);
        setOption("ScaleConversions", true);
        run("8-bit");
        }

        print("Please wait, creating stack nr. " +(i+1));

        run("Images to Stack", "method=[Copy (center)]
name=Stack_"+(n_slices_per_stack*i+1)+"_"+n_slices_per_stack*(i+1)+" title=[] use");
        run("AVI... ", "compression=JPEG frame=10
save="+input_path+"Stack_"+(n_slices_per_stack*i+1)+"_"+n_slices_per_stack*(i+1)+".avi");

        //Save as AVI
        saveAs("AVI",
input_path+"Stack_"+(n_slices_per_stack*i+1)+"_"+n_slices_per_stack*(i+1)+".avi");
        close("*");

        print("Stack nr. " +(i+1)+ " was correctly saved.");
    }

    //Creating the last stack, with the remaining images
    print("Creating the last stack, please wait..");

    for (element=n_slices_per_stack*i; element<fileList.length; element++){
        //Opening the remaining images
        open(input_path + fileList[element]);
        setOption("ScaleConversions", true);
        run("8-bit");
        }

    run("Images to Stack", "method=[Copy (center)]
name=Stack_"+(n_slices_per_stack*i+1)+"_"+fileList.length+" title=[] use");
    run("AVI... ", "compression=JPEG frame=10
save="+input_path+"Stack_"+(n_slices_per_stack*i+1)+"_"+fileList.length+".avi");
    saveAs("AVI", input_path+"Stack_"+(n_slices_per_stack*i+1)+"_"+fileList.length+".avi");
    close("*");

    print("Stack nr. " +(i+1)+ "was correctly saved.");
}

/*The intermediate stacks are now going to be opened and concatenated in a final Stack */
//1 stack only exists
if ((images_laststack == 0) & (n_stack == 1)){
    beep();
    print("Only one AVI stack was in the folder");
```

```
    //Deleting files not useful anymore
    fileList = getFileList(input_path);
    for (i = 0; i < fileList.length; i++) {
        if (endsWith(fileList[i], ".avi") == false){
            File.delete(input_path + fileList[i]);
        }
    }

    print("Done!");
    exit()
    }

//1+ stacks exist
print("Opening all the stacks to be concatenated, please wait..");
for (i=0; i<n_stack-1; i++){
    run("AVI...",
"avi="+input_path+"Stack_"+(n_slices_per_stack*i+1)+"_"+n_slices_per_stack*(i+1)+".avi use
convert");
    }
run("AVI...", "avi="+input_path+"Stack_"+(n_slices_per_stack*i+1)+"_"+fileList.length+".avi use
convert");

//Concatenate
conc_stack = "";
for (i=0; i<n_stack-1; i++){
    conc_stack +=
"image"+(i+1)+"=Stack_"+(i*n_slices_per_stack+1)+"_"+(n_slices_per_stack*(i+1))+".avi ";
    }

conc_stack += "image"+(i+1)+"=Stack_"+(i*n_slices_per_stack+1)+"_"+(fileList.length)+".avi";
print("Concatenating stacks, please wait..");
run("Concatenate...", "all_open title=Stack_all");
run("AVI... ", "compression=JPEG frame=10 save="+input_path+"Stack_all.avi");
saveAs("AVI", input_path+"Stack_all.avi");

print("Final stack was correctly saved.");

//Deleting files no longer useful
fileList = getFileList(input_path);

for (i = 0; i < fileList.length; i++) {
    if (fileList[i]!="Stack_all.avi"){
        File.delete(input_path + fileList[i]);
    }
}

beep();
print("Done!");
```

A.4 Grid Stitching of images from multiple directories with two channels

This macro reprises the same working principle of the Grid Stitching alternative presented in **Section A.2** and the "Channel A and B" setup used in **Section A.1** to realize, alongside mosaics for the optical channel, a parallel mosaic for the fluorescent signal. The *Stack_tiles.ijm* and *Align_and_Translate.ijm* scripts can be used then to create two time-lapse stacks – one per channel – and then perform the two-channel alignment.

Grid_Stitching_multidirectory_fluo.ijm

```
//Beatrice Bighi last modified 27/03/2023
print("\\Clear");

/*This macro performs custom Grid Stitching (see https://imagej.net/plugins/grid-collection-
stitching) to obtain rectangular mosaics from images collected during time-lapse imaging, from
adjacent spots. Usually, images collected for each spot are stored in separate folders: this
macro collects the different tiles corresponding to a certain time point from each folder and
performs the Grid Stitching routine. The user is required to provide the shape of the final
mosaic (n_x * n_y) and the expected overlap between tiles.*/

main_directory = getDirectory("Experiment folder containing the different tiles subfolders");
File.setDefaultDir(main_directory);
number_x = 4;
number_y = 1;
overlap = 20;
number = 1;

input_= newArray();
input_path_ = newArray();
input_path_fluo_ = newArray();
item = newArray(2);
    item[1] = "Yes";
    item[0] = "No";

//Ask the user the parameters to build the final mosaic
    Dialog.create("Parameters");
    Dialog.addMessage("Please specify the following final mosaic parameters");
    Dialog.addNumber("Nr. of tiles along x axis:", number_x);
    Dialog.addNumber("Nr. of tiles along y axis:", number_y);
    Dialog.addNumber("Expected tile overlap:", overlap);
    Dialog.show();

    Dialog.show();
    number_x = Dialog.getNumber();
    number_y = Dialog.getNumber();
    overlap = Dialog.getNumber();

    number = number_x * number_y;
    print("The final mosaic shape is:" +number_x+" x "+number_y+" with expected overlap
"+overlap);

//Asking the user to specify which folders are going to be considered as sources
/*The script automatically recognizes as channel A the folder "ContrastoFase"
and as channel B the folder "Fluorescenza", to changes this, edit the following lines.*/

    for (k=0; k<number; k++){
        input_[k]= getDirectory("Please, define the folder containing spot nr. "+ (k+1)+"\nPlease
note that the default settings expect tiles to be in 'Snake by Rows' in clockwise order");
        input_path_[k] = input_[k] + "ContrastoFase/";
        input_path_fluo_[k] = input_[k] + "Fluorescenza/";
    }
```

```
//Creating a folder to save outputs
    File.makeDirectory(main_directory + "mosaic");
    output_path = main_directory + "mosaic";
    File.makeDirectory(main_directory + "mosaic_fluo");
    output_path_fluo = main_directory + "mosaic_fluo";

//Grid Stitching
fileList = getFileList(input_path_[0]);
fileList_fluo = getFileList(input_path_fluo_[0]);
//print("fileList: "+fileList);
//print("fileList_fluo:"+fileList_fluo);

for (i=0; i<fileList.length; i++) {
    for (k=0; k<number; k++){
        open(input_path_[k] + fileList[i]);
        //run("8-bit");
        run("Enhance Contrast...", "saturated=0.35 normalize");
        saveAs("Tiff", output_path + "\\spot_" + (k+1) + ".tif");
        close();

        open(input_path_fluo_[k] + fileList_fluo[i]);
        //run("8-bit");
        //run("Enhance Contrast...", "saturated=0.35 normalize");
        run("Subtract Background...", "rolling=50 sliding");
        saveAs("Tiff", output_path_fluo + "\\spot_" + (k+1) + ".tif");
        close();
        }

    run("Grid/Collection stitching", "type=[Grid: snake by rows] order=[Right & Down]
grid_size_x="+number_x+" grid_size_y="+number_y+" tile_overlap="+overlap+" first_file_index_i=1
directory="+output_path+" file_names=spot_{i}.tif output_textfile_name=TileConfiguration.txt
fusion_method=[Linear Blending] regression_threshold=0.30 max/avg_displacement_threshold=2.50
absolute_displacement_threshold=3.50 compute_overlap computation_parameters=[Save memory (but be
slower)] image_output=[Fuse and display]");

    //Mosaics are saved with 4-digits numeration
    prefix = "";

    if ((i+1)<10){
        prefix = prefix + "000";
    }
    if ((10<=(i+1)) & ((i+1)<100)){
        prefix = prefix + "00";
    }

    if ((100<=(i+1)) & ((i+1)<1000)){
        prefix = prefix + "0";
    }

    saveAs("Tiff", output_path + "\\Tile_" + prefix + (i+1) + ".tif");
    close();

    File.delete(output_path + "\\TileConfiguration.txt");

    //Saving Results file
    File.copy(output_path + "\\TileConfiguration.registered.txt", output_path_fluo +
"\\TileConfiguration.registered.txt");

    //Re-constructing the fluorescent mosaic from the Results obtained by the Stitching of the
previous channel
    run("Grid/Collection stitching", "type=[Positions from file] order=[Defined by
TileConfiguration] directory="+output_path_fluo+" layout_file=TileConfiguration.registered.txt
fusion_method=[Linear Blending] regression_threshold=0.30 max/avg_displacement_threshold=2.50
absolute_displacement_threshold=3.50 computation_parameters=[Save memory (but be slower)]
image_output=[Fuse and display]");
    saveAs("Tiff", output_path_fluo + "\\Tile_" + prefix + (i+1) + ".tif");
    close();

    //Deleting files that are no longer useful
    for (k=0;k<number;k++){
```

```
        File.delete(output_path + "\\spot_" + (k+1) + ".tif");
        File.delete(output_path_fluo + "\\spot_" + (k+1) + ".tif");
        }

    }

print("Stitching completed!");
beep();
```

Acknowledgments

I would like to express my gratitude to Prof. Andrea Alessandrini for his guidance and supervision throughout the years of my PhD fellowship. Thank you also to Prof. Michele Bianchi and Dr. Andrea Mescola for their valuable advice.

My thanks also go to the past and present members of the NanoBioLab, especially Gregorio and Alice, whose collaboration made working together a rewarding experience.